Spectroscopy in Fuels

Lead Guest Editor: Xing Fan
Guest Editors: Xun Hu, Yao-Jen Tu, and Binoy K. Saikia

Spectroscopy in Fuels

Spectroscopy in Fuels

Lead Guest Editor: Xing Fan
Guest Editors: Xun Hu, Yao-Jen Tu, and Binoy K. Saikia

Editorial Board

Contents

Editorial
Spectroscopy in Fuels

Xing Fan [ID],[1] Xun Hu,[2] Yao-Jen Tu,[3] and Binoy K. Saikia[4]

[1]*Key Laboratory of Coal Processing and Efficient Utilization, Ministry of Education, China University of Mining & Technology, Xuzhou, Jiangsu 221116, China*
[2]*School of Material Science and Engineering, University of Jinan, Jinan 250022, China*
[3]*Institute of Urban Study, Shanghai Normal University, Shanghai 200234, China*
[4]*Polymer Petroleum and Coal Chemistry Group, Materials Science and Technology Division, CSIR-North East Institute of Science & Technology, Jorhat 785006, India*

Correspondence should be addressed to Xing Fan; fanxing@cumt.edu.cn

The special issue aims to provide contributions from spectroscopic technologies relating to the characterization of composition of fuels, evaluation of contamination emission, and the monitoring of fuels during thermal, physical, chemical, and biochemical conversion processes.

The special issue presents seven papers relating to biomass, jet fuel, coal, and so on. We feel that the published articles represent a certain wide range of researches in the scope of special issue. A series of analytical techniques like X-ray diffraction, Fourier-transform infrared spectroscopy, and mass spectrometry were included in the researches. This special issue is dedicated to the readers in the research fields of analytical chemistry, biochemical engineering, chemical engineering, material engineering, and mineral engineering.

In Y. Huang et al.'s paper, the microstructure, mineral composition, and precipitation of heavy metal elements of coal gangue with different weathering degrees were analyzed by electron microscopy and X-ray diffraction. The precipitation mechanism for heavy metals was revealed.

Trace water in jet fuel was characterized by thermometric titration in J.-Q. Hu's paper. The optimal detection system is 2,2-dimethoxypropane as titrant, cyclohexane, and isopropanol as titration solvents and methanesulfonic acid as catalyst. Rapid and accurate determination of trace water in a jet fuel can be realized by thermometric titration.

X-ray diffraction and gas chromatography/mass spectrometry were applied in R. Wang's research to characterize the Fe_2S_3/activated carbon catalyst and catalytic hydroconversion products of a coal, respectively. The results suggested that the catalyst could effectively catalyze the cleavage of C-C-bridged bonds in the coal.

The hydrotreating process of vegetable oil involves the transformation of vegetable oil triglycerides into straight-chain alkanes. J. García-Dávila et al. used Fourier-transform infrared spectroscopy and mass spectrometry to analyze the products of hydrotreating reaction from *Jatropha curcas* seed oil triglycerides.

H. Yang et al. reported an easily controlled method, electronic controlling, for fabricating regular nanotextures on an electrodeposited Ni-Co alloy, which was achieved using atomic force microscope. The friction force decreased when using different nanotextures in an external electric field.

T. Yao et al. investigated the deterioration mechanism of diester aero lubricating oil at high temperatures. Structures of the deteriorated lubricating oils were analyzed by gas chromatograph/mass spectrometry. Deterioration of aero lubricating oil at high temperatures included thermal pyrolysis, oxidation, and polymerization, with the generation of a variety of products such as alcohols, aldehydes, acids, and esters, which caused the deterioration of physicochemical properties of the aero lubricating oil.

Structural characterization of lignin and its degradation products with spectroscopic methods was reviewed by Y. Lu et al. Various spectroscopic methods, such as ultraviolet spectroscopy, Fourier-transformed infrared spectroscopy, Raman spectroscopy, and nuclear magnetic resonance

(NMR) spectroscopy, for the characterization of structural and compositional features of lignin were summarized. Various NMR techniques, such as ^{1}H, ^{13}C, ^{19}F, and ^{31}P, as well as 2D NMR, were highlighted for the comprehensive investigation of lignin structure.

Xing Fan
Xun Hu
Yao-Jen Tu
Binoy K. Saikia

Research Article

Catalytic Activity of a Bifunctional Catalyst for Hydrotreatment of *Jatropha curcas* L. Seed Oil

J. García-Dávila [iD],[1,2] E. Ocaranza-Sanchez,[1] C. Sánchez,[3] and A. L. Martínez-Ayala [iD][4]

[1]*Instituto Politécnico Nacional, Centro de Investigación en Biotecnología Aplicada, 90700 Tepetitla de Lardizabal, Tlaxcala, Mexico*
[2]*Universidad Politécnica de Tlaxcala, Av. Universidad Politécnica No. 1, San Pedro Xalcaltzinco, 90180 Tepeyanco, Tlaxcala, Mexico*
[3]*Universidad Autónoma de Tlaxcala, Laboratorio de Biotecnología, Centro de Investigación en Ciencias Biológicas,*
 90120 Tlaxcala, Mexico
[4]*Instituto Politécnico Nacional, Centro de Desarrollo de Productos Bióticos, 62731 Yautepec Morelos, Mexico*

Correspondence should be addressed to J. García-Dávila; jorge.garcia@uptlax.edu.mx and A. L. Martínez-Ayala; alayala@ipn.mx

The hydrotreating process of vegetable oils (HPVO) involves the transformation of vegetable oil triglycerides into straight chain alkanes, which are carried out by deoxygenation reactions, generating multiple hydrocarbon compounds, cuts similar to heavy vacuum oil. The HPVO is applied to *Jatropha curcas* oil on USY zeolite supported with gamma alumina and platinum deposition on the catalytic as hydrogenation component. The acid of additional activity of the supports allows the development of catalytic routes that the intervention of catalytic centers of different nature reaches the desired product. The products of the hydrotreating reaction with *Jatropha curcas* seed oil triglycerides were identified by Fourier transform infrared spectroscopy and by mass spectroscopy to identify and analyze the generated intermediate and final hydrocarbon compounds.

1. Introduction

Currently, there is a decline in fossil fuel reserves by contrast, every year the increase in demand for liquid fuels, such as environmental pollution due to excessive use; it is necessary to obtain renewable liquid fuels from natural sources. Triglyceride-based vegetable oils are a potential raw material for the production of biofuels. *Jatropha curcas* seed oil is one of the most important alternative nonedible types of vegetable oils for biofuel production [1]. The fluid catalytic cracking (FCC) process uses fossil fuels to produce, that is, gasoline, diesel, and olefins, where large molecules are broken down with the help of a catalyst [2].

Catalyst is the key factor in promoting high activity and selectivity to product distribution. In fact, new research materials focus on improving catalytic activity and generate fewer by-products and contaminants [3]. The heterogeneous catalyst is the great economic impact as the USY zeolite which provides high activity and selectivity of the catalysts.

USY is a large pore crystalline material having a maximum aperture of 0.74 nm, a cell unit size of about 2.45 mm, a Si/Al ratio of 3 to 5, and having shape selectivity to have the sites more active in the microporous structure [4].

The zeolite USY is widely used as a catalyst support and plays an important role in the catalysts used in the hydrocracking process because they enhance catalytic activity, selectivity, or stability imparting shape selectivity [5]. However, the high acidity of the zeolite carrier increases undesirable cracking activity, which accelerates the rate of coke deposition. The incorporation of a metallic phase on the support materials with a high dispersion allows the development of catalytic routes in which the intervention of catalytic centers of different nature achieves the desired product [6] (multifunctional catalysts).

Conventional hydrotreating involves the removal of heteroatoms, such as sulfur and nitrogen. The hydrocracking process involves the saturation and breakage of C-C bonds to produce high-grade gasoline and diesel fuels [7]. A novel

alternative for the production of biofuels is catalytic hydrotreatment and hydrocracking of vegetable oils [8].

Hydrotreatment of vegetable oil and its mixtures with heavy vacuum gas oil has been explored to produce biofuels using conventional hydrotreating catalysts based on Ni-Mo/Al_2O_3 and Co-Mo/Al_2O_3 [9] under conventional conditions of nominal hydrodesulfurization operation [10]. A novel alternative to manufacture biofuels is catalytic hydrotreatment and hydrocracking of vegetable oils. Several hydrotreated vegetable oils include palm oil [11], *Jatropha curcas* L. [12], *Jatropha cinerea* oil [13], and soybean lecithin [14].

USY zeolite has been reported to use as a catalyst for cracking of waste cooking oils [15] and *Jatropha curcas* [16]. Favor you apply in very different pressure and temperature conditions. In this work, we use the γ-alumina which is the most commonly used as support on which the active component in this case is dispersed the zeolite USY which presents activity acid. In addition, in the form of dispersion are incorporated platinum particles that act as a function of hydrogenation in the catalyst for the hydrotreatment of *Jatropha curcas* seed oil [17].

2. Experimental

2.1. Jatropha curcas Seed Oil.
The *Jatropha curcas* L. seed species used in this study are native to the state of Puebla, Mexico. The seed oil was extracted by mechanical pressing using an ELVEC press. The vegetable oil was used without a pretreatment.

2.2. Preparation of Zeolite USY.
The support used was γ-alumina with a specific surface area of $270 \, m^2/g$ and a volume of $0.8 \, cm^3/g$. It was mixed with zeolite USY at 10 and 20 wt%. The samples were extruded and dried at 110°C overnight and calcined in air at 500°C for 4 h. This mixture was used as platinum metal support. The catalysts were prepared by impregnating the aqueous solution of chloroplatinic acid (H_2PtCl_6) as a precursor using the incipient impregnation wetness method. After impregnation, the sample was dried at 110°C overnight, followed by calcination at 500°C for 4 h in a muffle furnace. After activation, the catalyst was reduced for 4 h at 400 psia and 400°C under a hydrogen flow of $60 \, mL \, min^{-1}$.

The adsorption of water was used as a manual method for the determination of the specific surface [18]; it is a simple and economical approximation to obtain the value of $0.45 \, mL/g$ of catalyst (± 0.01). Both the pore volume and the pore size of the zeolite are smaller than the alumina sample. The presence of Pt partially reduces the sites, responsible for coking [19] for their masking with the metal particles Pt; hence, the activity of the catalyst persists over a long period.

2.3. Catalytic Activity.
The catalytic performance of the bifunctional catalyst was investigated by hydrotreating *Jatropha curcas* seed oil in a continuous flow tubular reactor of 9 mm internal diameter and 300 mm in length vertically within the tubular programmable temperature. Nitrogen gas was introduced into the system to fully purge air from the system while the reactor reached the desired temperature. The hydrotreating process was carried out under the following conditions: temperature 310, 360, and 390°C, total pressure 400 psi, hourly space velocity by weight (WHSV) $176.4–35.28 \, h^{-1}$ (0.5 and 0.1 g of the catalyst were charged), and hydrogen to feed oil molar ratio of 15.

2.4. Analysis of Hydrotreatment Samples.
The analysis of the products was performed using a Fourier transform infrared spectroscopy (FTIR). Using a Bruker Vertex-70 unit in an ATR (attenuated total reflectance) sampling mode, the system is equipped with an OPUS program for data acquisition and the region of measurement was the middle infrared ($4000–400 \, cm^{-1}$) with a resolution of $4 \, cm^{-1}$. Subsequently, the liquid products were analyzed using an Agilent 7890A GC/MSD gas chromatograph, with the G4513A auto sampler coupled to a 5975C VL MSD mass spectrometer with triple axis detector; a capillary HP-5MS ($30 \, m^* 320 \, \mu m^* 0.25 \, \mu m$) was used with the external standard technique for quantification. The GC/MSD parameters were oven program, 70°C for 5 min, 20°C/min at 200°C for 5 min, and then 10°C/min at 300°C for 5 min, with an injection volume of $2 \, \mu L$ and temperatures of 230°C and 150°C for MS source and quadruple, respectively, with the ChemStation program for data acquisition in mode scan.

A calibration curve was taking from the previous work of García-Dávila et al. [20] that represents the band intensity quantification at $1743 \, cm^{-1}$ and $1160 \, cm^{-1}$, indicating the abundance of fatty acids (Figures 1 and 2). Using *Jatropha curcas* seed oil spectrum as the maximum content of oxygenates compounds, and n-hexadecane as hydrocarbon molecule model as the minimum oxygenated compounds, this compound was taken an internal standard to represent the final hydrotreatment product. The reduction of the signal in the band intensity at $1743 \, cm^{-1}$ and $1160 \, cm^{-1}$ was quantified and correlated with the conversion [21].

3. Results

3.1. Spectrometry FTIR.
The hydrotreatment tests were performed by testing the Al_2O_3 support loaded with two percentages of 10 and 20% USY zeolite to observe the effect of the acid activity of the zeolite on the oil. Subsequent to the appropriate relationship, platinum (Pt) molecules are incorporated by the incipient wetness impregnation method to add the hydrogenating function; two different weight fractions as indicated in Table 1 were tested to quantify the specific metallic activity in the catalyst.

A comparison of hydrotreated samples was carried out by attenuated total reflectance spectroscopy (FTIR-ATR), where the amplitude of the oil peaks was compared with the amplitude of the peaks of the hydrotreated samples. It was taken as the baseline below the n-hexadecane spectrum (100% conversion) and *Jatropha curcas* oil as the upper base (0% conversion) to standardize the magnitudes of the FTIR peaks and quantitatively establish the conversion, a calibration curve by means of dilutions of the oil with hexadecane (Figures 1 and 2). From the correlation of the signal intensity of the spectra by the FTIR of the samples, the limit of the
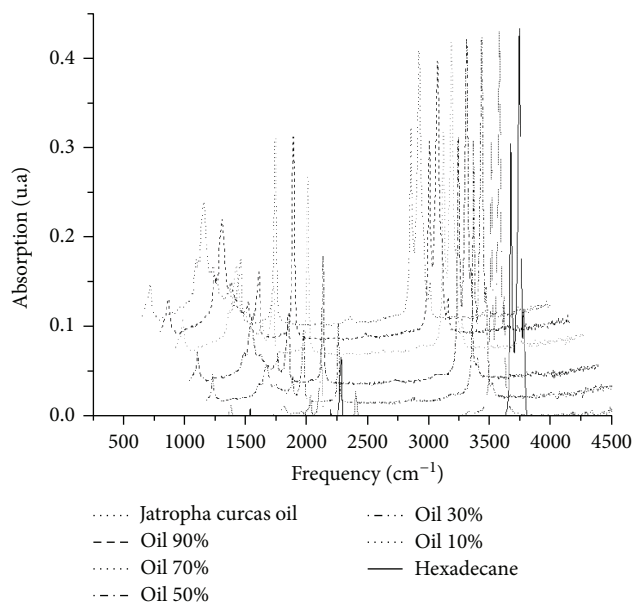
Figure 1: FTIR spectra of calibration curve of *Jatropha curcas* oil with hexadecane [12].

Figure 2: Calibration curve of *Jatropha curcas* seed oil dilutions with hexadecane at 1743 and 1160 cm^{-1} wavelength [12].

Table 1: Formulation of bifunctional catalyst for hydrotreatment of *Jatropha curcas* seed oil.

Quantity of USY zeolite on gamma alumina	Catalyst charging to the reactor (g)	Platinum (%)
0% USY/Al$_2$O$_3$	0.5	0.05
10% USY/Al$_2$O$_3$		0.01
20% USY/Al$_2$O$_3$	0.1	0.05
		0.01

There was a decrease in the characteristic peaks of the fatty acids in the hydrotreatment samples; this phenomenon was registered at temperatures of 310°C according to the increase of the operating temperature. To discriminate the thermal cracking effect on the hydrotreatment process, a test without catalyst was run, where the evidence shows that there is no significant difference between the FTIR spectra with respect to the crude oil which demonstrates that there is no thermal degradation of the triglyceride and the process only develops as a function of the bifunctional catalyst (Figure 3). These data are consistent with those reported by Idem et al. [22] for canola oil, wherein the thermal cracking is significant above 400°C and increases with operating temperature.

It is observed that at higher USY zeolite/alumina ratio, there is a higher acid activity like sulfur-type catalysts such as Co-Mo and Ni-Mo, with conversions above 60% at residence times, like those reported for other catalysts [23].

From the analysis by FTIR, a shift to low frequencies in the wave number is observed by the presence of characteristic peaks of carbonyl and carboxyl groups. These representing the formation of compounds with functional groups of ketones and aldehydes which are considered as the first intermediate products generated in the hydrotreatment process [24] after the disintegration of the triglyceride, this information will be corroborated by gas chromatography coupled to mass spectroscopy.

The absorption band shift was recorded with a wavelength of 1743 to 1710 cm^{-1} corresponding to group (C=O) characteristic of ketones and aliphatic aldehydes Figure 4 unlike the group (C=O) of the fatty acids that has a lower stability because of not containing the (OH) group. The signal from this group increases its absorbance by increasing the operating temperature of the hydrotreatment process, which indicates that more fatty acid reduction is present at higher operating temperatures [25].

With the formulation of the 20% USY/Al$_2$O$_3$ catalyst, platinum particles were incorporated by the incipient wetness impregnation method. To this end, a solution of chloroplatinic acid H$_2$PtCl$_6$ was prepared from the grams of platinum to be incorporated into the matrix of 0.01, 0.05, and 0.1 g, respectively, with a comparison being made between the catalytic activities for each formulation of the bifunctional catalyst.

The results show that the catalyst with the highest activity to hydrocarbon transformation is the formulation with 20% of zeolite USY/Al$_2$O$_3$ with a percentage of 0.01% Pt (Figure 5). Since at higher percentages, the metallic phase

superior of the respect and the inferior one determined the progress in the reduction of the band intensity of the fatty acids in a process of hydrotreatment of *Jatropha curcas* seed oil.
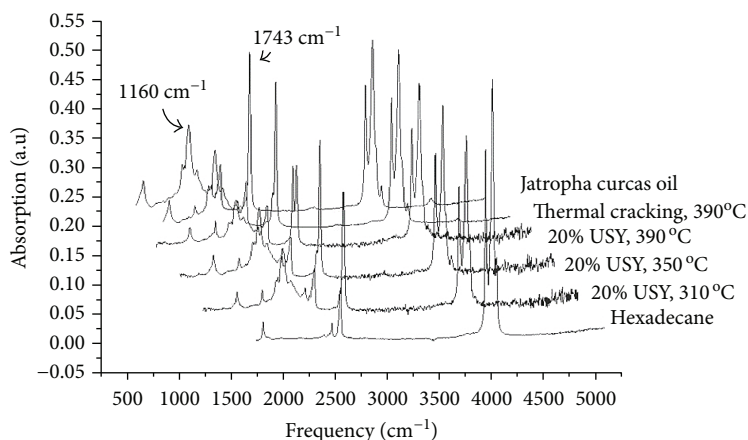
Figure 3: FTIR spectra of hydrotreated oil at different temperatures with WHSV of $3\,min^{-1}$ with 20% USY/Al_2O_3 without metallic active phase.
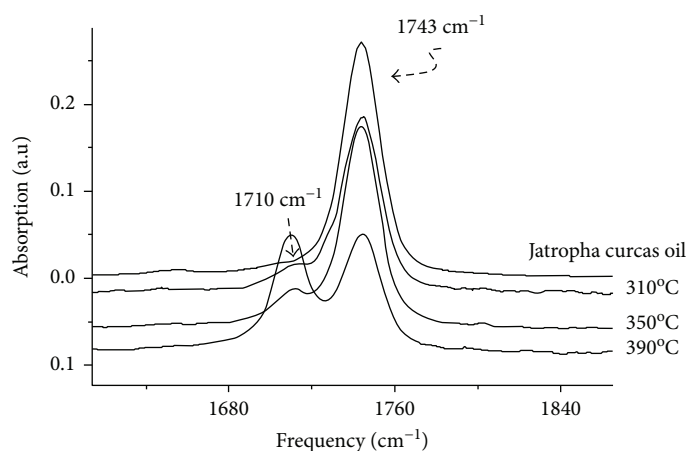
Figure 4: Displacement of absorption bands in hydrotreated samples with 20% USY catalyst with WHSV of $35.28\,h^{-1}$.
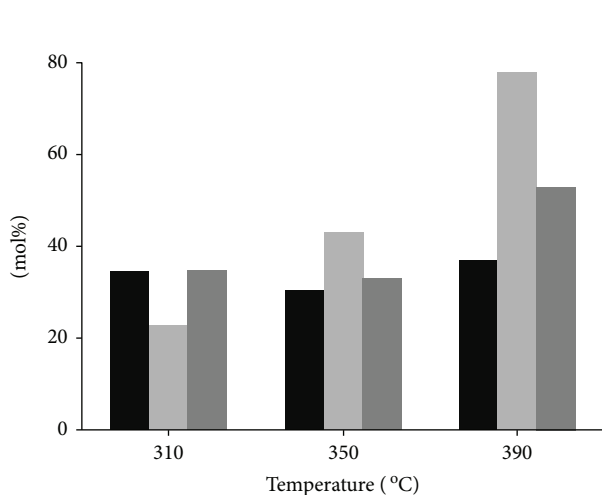
Figure 5: Comparative catalytic activity in samples hydrotreated by FTIR at different temperatures and WHSV with platinum-loaded 20% USY/Al_2O_3 catalyst. (black square) 0.01% Pt WHSV = $176.4\,h^{-1}$; (light gray square) 0.01% Pt WHSV = $35.28\,h^{-1}$; and (dark gray square) 0.05% Pt WHSV = $35.28\,h^{-1}$.
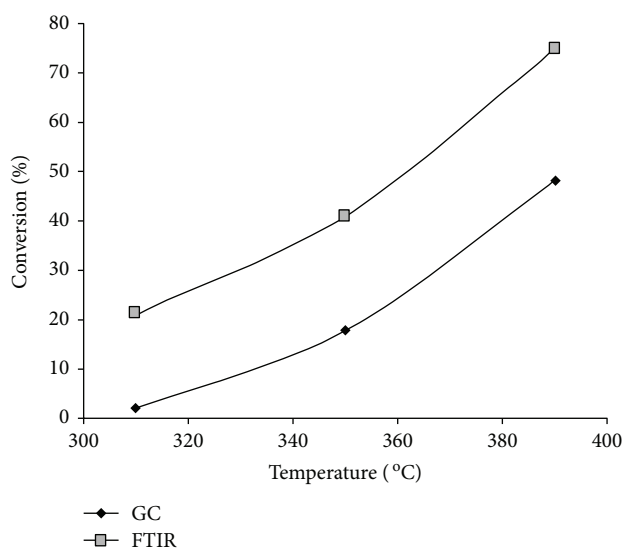
Figure 6: Comparative maximum conversion and hydrotreated samples by FTIR and CG/MSD at different temperatures with catalyst 0.01% Pt and 20% USY/Al_2O_3 at WHSV = $35.28\,h^{-1}$.
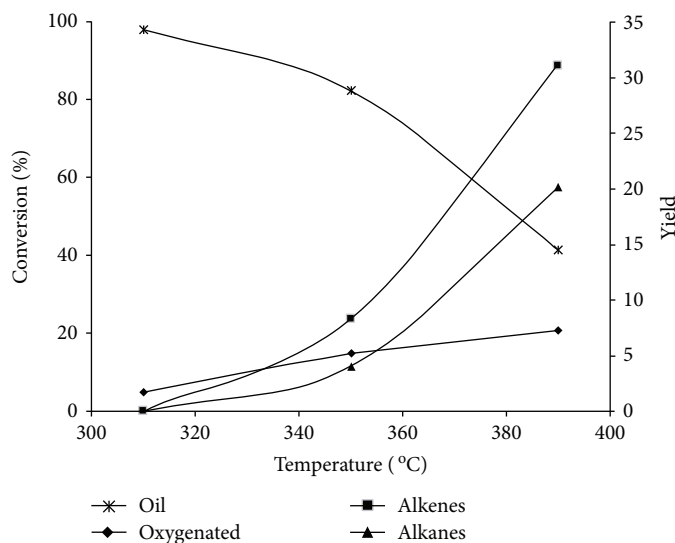
FIGURE 7: Catalytic activity for *Jatropha curcas* L. seed oil. Catalytic selectivity in functional groups for bifunctional catalyst 0.01% Pt and 20% USY/Al$_2$O$_3$ at WHSV = 35.28 h^{-1}.

does not allow the transition towards the acid phase, which results in a rapid saturation of the free fatty acids not allowing molecular cracking reactions [26]. The total triglyceride conversion is proportionality to temperature. At 310°C, conversion levels reach 20% with 0.01% Pt loaded; at 350°C, conversion levels increase until 40%; and finally at 390°C, conversion levels increase to 75% at WHSV 35.3 h^{-1}.

3.2. CG/MSD. A comparative study of the degree of reaction progression by FTIR and CG/MSD was carried out, where it was observed (Figure 6) that there is a higher degree of advancement by FTIR compared to CG/MSD for the same samples; with increasing temperature at 390°C, there is a significant difference between the yields for the same catalyst formulation.

Despite this, both analytical techniques coincide in the formulation of the catalyst with 20% of zeolite USY/Al$_2$O$_3$ with a percentage of 0.01% Pt as the formulation of greater activity in the hydrotreatment process. The discrepancies in absorbance values obtained by FTIR are overestimated by the presence of compounds with similar C = O binding. This is attributed to the formation of light fatty acids of lower molecular weight compared to the initials present in the triglyceride. It is known that in the process, hydrotreating occurs first before hydrocracking [27]. Whereby at a temperature of 310°C, there is more hydrogenation/dehydrogenating activity than acidic activity [28].

By FTIR analysis, the light fatty acids considered them as reactive for keeping the C=O bond current, while for CG/MSD, they were considered as reaction intermediates since they are not part of the initial triglyceride. This difference is observable for each operating temperature performed in this work, where there is the presence of other functional groups that makes the reaction follow-up similar by both techniques.

The formation of partially deoxygenated groups increases as temperature and WHSV increase; these compounds are considered as primary intermediates of reaction of the free fatty acids to olefins and as by-products of reaction to the alkanes and aromatics as a result of processes of cyclization and hydrogenation of the olefins [29]. The hydrocarbon cuts formed have a high selectivity towards the formation of chains of the order of diesel and in less amount hydrocarbon formation of the order of jet fuel and gasolines in a proportion of 6 : 1 and 21 : 1, respectively, Figures 6, 7, and 8.

It is clearly observed that at a temperature of 390°C, there is a higher formation of hydrocarbons of the order of diesel with a yield of more than 35%, while for jet fuel and gasolines are maintained at yields of less than 10%; this emphasizes that the catalyst is selective to cuts of diesel. Similar results have been reported by Zheng et al. [16] and Li et al. [15] who reported similar conversions of 68.6% and 58.7% of liquid products, respectively, at higher WHSV and temperature values compared with those used in this research.

4. Conclusions

The bifunctional catalyst synthesized showed high activity in the hydrotreatment of *Jatropha curcas* seed oil with a selectivity towards linear hydrocarbon chains; the activity increases as a function of temperature and space velocity but with a decrease in the selectivity towards hydrocarbon chains of the order of the diesel.

The selectivity towards the formation of saturated fatty acids was increased with platinum loading percentages of 0.01 wt% on the surface of the catalyst responsible for the hydrogenating activity, resulting in a decrease in acid activity. The formulation of the catalyst that showed the highest activity in high molecular weight hydrocarbon cuts is (0.01%) Pt and (20%) USY/Al$_2$O$_3$ for both process monitoring techniques.

USY zeolite is very active and selective as hydrotreated catalyst, even at moderate conditions, and that can be
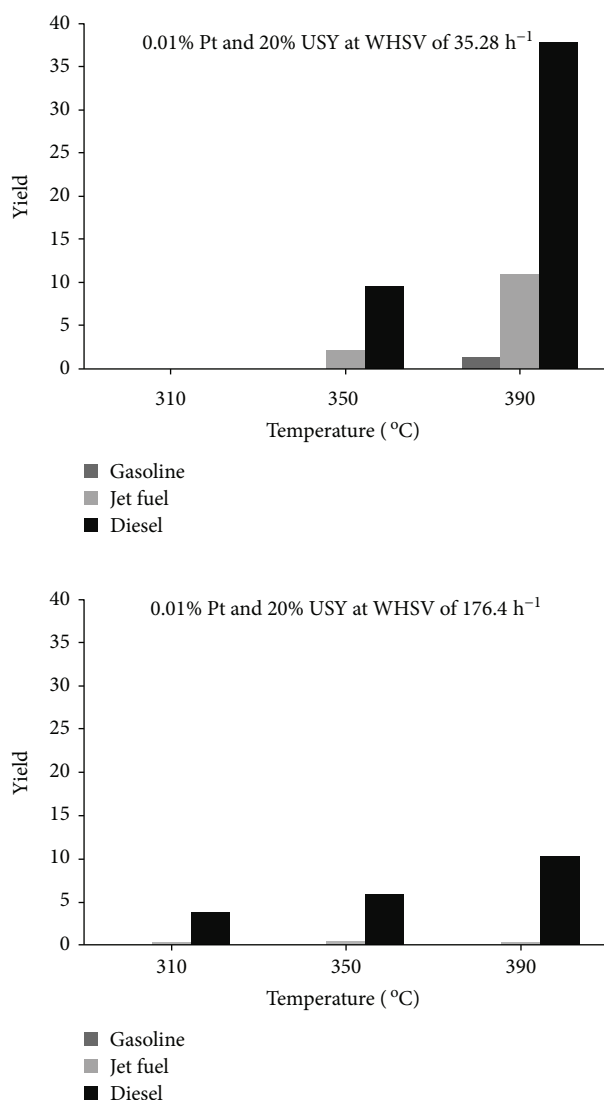
FIGURE 8: Yield in hydrocarbon cuts as a function of temperature and WHSV with bifunctional catalyst 0.01% Pt and 20% USY/Al$_2$O$_3$.

attributed to its acidity function, which is strong enough to accelerate this reaction. Pt incorporation in the zeolite is greatly effective for enhancing the transformation of *Jatropha curcas* seed oil and for improving the selectivity to the linear hydrocarbons reaction.

Conflicts of Interest

The authors declare no conflicts of interest.

Acknowledgments

References

[1] K. Becker and H. P. S. Makkar, "*Jatropha curcas:* a potential source for tomorrow's oil and biodiesel," *Lipid Technology*, vol. 20, no. 5, pp. 104–107, 2008.

[2] J. Hancsók, S. Magyar, and D. Kalló, "Selective hydrodesulphurization of full range FCC gasoline on PtPd/USY-zeolite," *Petroleum & Coal*, vol. 46, no. 2, pp. 1–12, 2004.

[3] A. Galadima, J. A. Anderson, and R. P. K. Wells, "Solid acid catalysts in heterogeneous n-alkanes hydroisomerisation for increasing octane number of gasoline," *Science World Journal*, vol. 4, no. 3, 2010.

[4] M. Chareonpanich, Z.-G. Zhang, and A. Tomita, "Hydrocracking of aromatic hydrocarbons over USY-zeolite," *Energy & Fuels*, vol. 10, no. 4, pp. 927–931, 1996.

[5] Y. Y. A. Pertuz, L. A. Oviedo, U. U. Navarro, M. A. Centeno, and J. A. Odriozola, "Modificaciones de las propiedades texturales y estructurales de una zeolita USY y de sus mezclas con caolín clay y clorhidrol como consecuencia del tratamiento hidrotérmico," *Revista Colombiana de Química*, vol. 35, no. 1, 2006.

[6] A. M. Alsobaai, R. Zakaria, and B. H. Hameed, "Hydrocracking of gas oil over Ni-W, Ni-Mo, Co-W and Co-Mo catalysts supported on USY zeolite," *Arab Research Institute in Sciences & Engineering*, vol. 3, no. 3, pp. 91–98, 2007.

[7] A. M. Alsobaai, R. Zakaria, and B. H. Hameed, "Characterization and hydrocracking of gas oil on sulfided NiW/MCM-48 catalysts," *Chemical Engineering Journal*, vol. 132, no. 1-3, pp. 173–181, 2007.

[8] T. Morgan, D. Grubb, E. Santillan-Jimenez, and M. Crocker, "Conversion of triglycerides to hydrocarbons over supported metal catalysts," *Topics in Catalysis*, vol. 53, no. 11-12, pp. 820–829, 2010.

[9] Y. Liu, R. Sotelo-Boyás, K. Murata, T. Minowa, and K. Sakanishi, "Hydrotreatment of vegetable oils to produce bio-hydrogenated diesel and liquefied petroleum gas fuel over catalysts containing sulfided Ni–Mo and solid acids," *Energy & Fuels*, vol. 25, no. 10, pp. 4675–4685, 2011.

[10] S. Bezergianni and A. Kalogianni, "Hydrocracking of used cooking oil for biofuels production," *Bioresource Technology*, vol. 100, no. 17, pp. 3927–3932, 2009.

[11] N. Taufiqurrahmi, A. R. Mohamed, and S. Bhatia, "Deactivation and coke combustion studies of nanocrystalline zeolite beta in catalytic cracking of used palm oil," *Chemical Engineering Journal*, vol. 163, no. 3, pp. 413–421, 2010.

[12] J. García-Dávila, E. Ocaranza-Sánchez, M. Rojas-López, J. A. Muñoz-Arroyo, J. Ramírez, and A. L. Martínez-Ayala, "*Jatropha curcas* L. oil hydroconversion over hydrodesulfurization catalysts for biofuel production," *Fuel*, vol. 135, pp. 380–386, 2014.

[13] A. L. F. Santos, D. U. Martins, O. K. Iha, R. A. M. Ribeiro, R. L. Quirino, and P. A. Z. Suarez, "Agro-industrial residues as low-price feedstock for diesel-like fuel production by thermal cracking," *Bioresource Technology*, vol. 101, no. 15, pp. 6157–6162, 2010.

[14] M. Díaz de León-Cabrera and M. A. Sánchez-Castillo, "Basis for triglycerides and phospholipids conversion into fuels using mesoporous catalysts," *Revista Mexicana de Ingeniería Química*, vol. 15, no. 1, pp. 111–128, 2016.

[15] L. Li, Z. Ding, K. Li et al., "Liquid hydrocarbon fuels from catalytic cracking of waste cooking oils using ultrastable zeolite

USY as catalyst," *Journal of Analytical and Applied Pyrolysis*, vol. 117, pp. 268–272, 2016.

[16] Q. Zheng, L. Huo, H. Li et al., "Exploring structural features of USY zeolite in the catalytic cracking of *Jatropha curcas* L. seed oil towards higher gasoline/diesel yield and lower CO_2 emission," *Fuel*, vol. 202, pp. 563–571, 2017.

[17] K. Murata, Y. Liu, M. Inaba, and I. Takahara, "Production of synthetic diesel by hydrotreatment of jatropha oils using Pt-Re/H-ZSM-5 catalyst," *Energy & Fuels*, vol. 24, no. 4, pp. 2404–2409, 2010.

[18] B. Lombardi, M. A. Dapino, P. R. Montardit, and R. M. Torres Sánchez, "Aproximación al valor de superficie específica por un método manual y simple," *Jornadas SAM-CONAMET-AAS*, vol. 1, pp. 251–256, 2011.

[19] D. Bazin, D. Guillaume, C. Pichón, D. Uzio, and S. Lopez, "Structure and size of bimetallic palladium-platinum clusters in an hydrotreatment," *Oil & Gas Science and Technology*, vol. 60, no. 5, pp. 801–813, 2005.

[20] J. García-Dávila, E. Ocaranza-Sánchez, C. Sánchez, E. Ortega-Sánchez, S. Tlecuitl-Beristaín, and A. L. Martínez-Ayala, "FTIR analysis of hydrotreated *Jatropha curcas* L. seed oil over Ni-Mo catalyst for biofuel production," *Revista Mexicana de Ingeniería Química*, vol. 16, no. 2, pp. 337–345, 2017.

[21] J. K. Satyarthi and D. Srinivas, "Fourier transform infrared spectroscopic method for monitoring hydroprocessing of vegetable oils to produce hydrocarbon-based biofuel," *Energy & Fuels*, vol. 25, no. 7, pp. 3318–3322, 2011.

[22] R. O. Idem, S. P. R. Katikaneni, and N. N. Bakhshi, "Catalytic conversion of canola oil to fuels and chemicals: roles of catalyst acidity, basicity and shape selectivity on product distribution," *Fuel Processing Technology*, vol. 51, no. 1-2, pp. 101–125, 1997.

[23] M. Chiappero, P. T. M. Do, S. Crossley, L. L. Lobban, and D. E. Resasco, "Direct conversion of triglycerides to olefins and paraffins over noble metal supported catalysts," *Fuel*, vol. 90, no. 3, pp. 1155–1165, 2011.

[24] D. Kubicka, P. Símácék, and N. Zilkova, "Transformation of vegetable oils into hydrocarbons over mesoporous-alumina-supported CoMo catalysts," *Topics in Catalysis*, vol. 52, no. 1-2, pp. 161–168, 2009.

[25] G. W. Huber, P. O'Connor, and A. Corma, "Processing biomass in conventional oil refineries: production of high quality diesel by hydrotreating vegetable oils in heavy vacuum oil mixtures," *Applied Catalysis A: General*, vol. 329, pp. 120–129, 2007.

[26] S. A. El-Khatib, M. G. Abd El-Wahed, L. K. Mohamed, and S. A. El-Saadany, "Hydroconversion of n-octane over platinum containing H-ZSM-5 zeolite and alumina catalysts," *Journal of Applied Sciences Research*, vol. 5, no. 9, pp. 1163–1172, 2009.

[27] S. Bezergianni, A. Kalogianni, and I. A. Vasalos, "Hydrocracking of vacuum gas oil-vegetable oil mixtures for biofuels production," *Bioresource Technology*, vol. 100, no. 12, pp. 3036–3042, 2009.

[28] J. Hancsók, S. Magyar, K. Juhász, and D. Kalló, "HDS, HDN and HDO of FCC gasoline spiked with benzothiophene over PtPd/H-USY," *Topics in Catalysis*, vol. 45, no. 1–4, pp. 207–212, 2007.

[29] E. Vonghia, D. G. B. Boocock, S. K. Konar, and A. Leung, "Pathways for the deoxygenation of triglycerides to aliphatic hydrocarbons over activated alumina," *Energy & Fuels*, vol. 9, no. 6, pp. 1090–1096, 1995.

Research Article

Effect of Pretreatment with Sulfuric Acid on Catalytic Hydrocracking of Fe/AC Catalysts

Ruiyu Wang,[1] Fei Wang,[2] and Ling Liu[1]

[1]*Key Laboratory of Coal-Based CO_2 Capture and Geological Storage of Jiangsu Province, China University of Mining & Technology, Xuzhou, Jiangsu 221008, China*
[2]*School of Chemical Engineering and Technology, China University of Mining & Technology, Xuzhou, Jiangsu 221116, China*

Correspondence should be addressed to Ruiyu Wang; wangruiyu@cumt.edu.cn

Activated carbon (AC) was modified by H_2SO_4 and used as a support for catalyst. The Fe_2S_3/AC-T catalyst was prepared by deposition-precipitation method and used to catalyze hydrocracking of coal-related model compound, di(1-naphthyl)methane (DNM). The properties of catalyst were studied by N_2 adsorption-desorption, X-ray diffraction, and scanning electron microscopy. The result showed that ferric sulfate and acidic centers had synergetic effect on hydrocracking of DNM when using Fe_2S_3/AC-T as catalyst, the optimal loading of Fe is 9 wt.%. Hydroconversion of the extraction residue from Guizhou bituminous coal was also studied using Fe_2S_3/AC-T as the catalyst. The reaction was conducted in cyclohexane under 0.8 Mpa of initial hydrogen pressure at $310°C$. The reaction mixture was extracted with petroleum ether and analyzed by GC/MS. Amounts of organic compounds which fall into the categories of homologues of benzene and naphthalene were detected. It suggested that the catalyst could effectively catalyze the cleavage of C-C-bridged bonds.

1. Introduction

As an important chemical process, direct coal liquefaction (DCL) could be a feasible option to directly convert coals into liquid fuels or chemicals [1, 2]. Nowadays, rapid decrease of petroleum stresses the importance of coals for covering the shortage of organic chemical feedstock [3, 4]. Compared to the existing DCL performed at high temperatures, low-temperature DCL should be more promising in consideration of the fact that the formation of gaseous products and coke can be considerably reduced at low temperatures [5–7].

Catalyst is one of key issues in DCL process. Considerable efforts [8–15] have been contributed to the catalytic performances of metal-based (Fe and Ni) catalysts for DCL or to the reactions of coal-related model compounds. It is generally accepted that catalysts can significantly promote coal pyrolysis by reducing the pyrolysis activation energy and the formation of active hydrogen atoms (AHAs) by facilitating H_2 dissociation [16, 17]. The cleavage of C-C bridged bonds in coals, which is very important for DCL, begins with the secondary distribution of AHAs in the whole reaction system [9, 15, 17]. Iron sulfides are commonly used catalyst for DCL because of their easy availability. By literatures [18, 19], FeS_2 thermolysis to $Fe_{1-x}S$ and FeS_2 regenerated from the reaction of $Fe_{1-x}S$ with H_2S facilitates the continuous formation of AHAs. In another word, the cycle of FeS_2 decomposition and regeneration contributes to its catalysis in the reactions of DCL.

Although the iron-based catalysts are successfully used in industrial processes of DCL, their efficiency is still quite low. Solid acids are commonly catalyst for cracking reactions, and the corresponding acidic sites are active for the cleavage of C-C-bridged bonds [12–14, 20, 21]. If combined with acidic centers, the Fe-based catalyst could exhibit an improved catalytic performance in DCL process. Therefore, we prepared an iron sulfide-supported catalyst, the activated carbon (AC) which was modified by H_2SO_4 was used as support, and the catalysts were used to catalyze hydrocracking of a coal-related model compound (DNM) and hydroconversion of the extraction residue of a bituminous coal.

2. Experiments

2.1. Preparation of Catalyst. Guizhou bituminous coal (GBC) was collected from Guizhou province, China. It was pulverized to pass a 200-mesh sieve followed by desiccation in a vacuum oven at 80°C before use. All of chemical reagents used in the experiments are commercially obtained.

3 g activated carbon (AC) was placed in a beaker, and 10 mL H_2SO_4 (2 mol/L) was added. The mixture was disposed by ultrasound by placing the beaker into an ultrasonic oscillator for 3 min and then kept overnight. The obtained mixture was dried under drier at 80°C for 6 h. The product obtained was denoted as AC-T (T means treated carrier), and the corresponding amount of acid was 2.0 mmol/g, which was measured via neutral drip reaction with NaOH solution.

A certain amount of $Fe_2(SO_4)_3$ (0.34 g, 0.59 g, 0.86 g, 1.16 g, and 1.48 g) and the corresponding amount of $Na_2S \cdot 9H_2O$ (0.612 g, 1.602 g, 1.55 g, 2.09 g, and 2.66 g) were dissolved in 50 mL deionized water, respectively. Under stirring, both the Na_2S and $Fe_2(SO_4)_3$ aqueous solution were continuously dropped to 10 mL deionized water at the same rate. When the reactions were completed, the 3 g AC-T support was added. The mixture was kept stirring for 10 min followed by filtration, and the filter cake was dried at 100°C for 2 h. The product obtained was calcined at 300°C and held at the temperature for 2 h under a protection of N_2 flow. The obtained catalyst was denoted as $Fe_2S_3/$ AC-T(x), where x represents the weight percentage of Fe in catalyst.

For unmodified AC as support, the catalyst prepared at the same conditions was denoted as Fe_2S_3/AC.

2.2. Characterization of Catalyst. N_2 adsorption-desorption isotherms were measured with a Bayer BELSORP-max instrument. Specific surface area (SSA), total pore volume (TPV), and average pore diameter (APD) of the samples were calculated from the isotherms via t-plot, BJH, and HK methods, respectively. Morphology of the samples and the corresponding elemental distribution on the surface were characterized using a FEI Quanta 250 scanning electron microscope (SEM) coupled with an energy-dispersive spectrometer (EDS). The X-ray diffraction pattern was recorded on a Burker D8 ADVANCE diffractometer with a scanning rate of 4°/min at 2θ of 10 to 80°, using a Cu ka radiation ($\lambda = 0.154$ nm) at 40 kV and 40 mA.

2.3. Di(1-naphthyl)methane Hydrocracking. Di(1-naphthyl)-methane (DNM, 1 mmol), catalyst (0.4 g), and cyclohexane (30 mL) were put into a 60 mL stainless, magnetically stirred autoclave. After replacing the air with hydrogen for 3 times, the autoclave was pressurized to 0.8 MPa and heated to an indicated temperature in 15 min. Under stirring at a rate of 200 r/m, the reaction was conducted for 1 h. Then the autoclave was cooled to room temperature in an ice-water bath. The gaseous reaction mixture was taken out from the autoclave and quantified using a gas chromatography (9790, Zhejiang Fuli, China).

2.4. GBC Residue Hydroconversion. 2 g GBC and 50 mL acetone were put into a 100 mL stainless, magnetically stirred
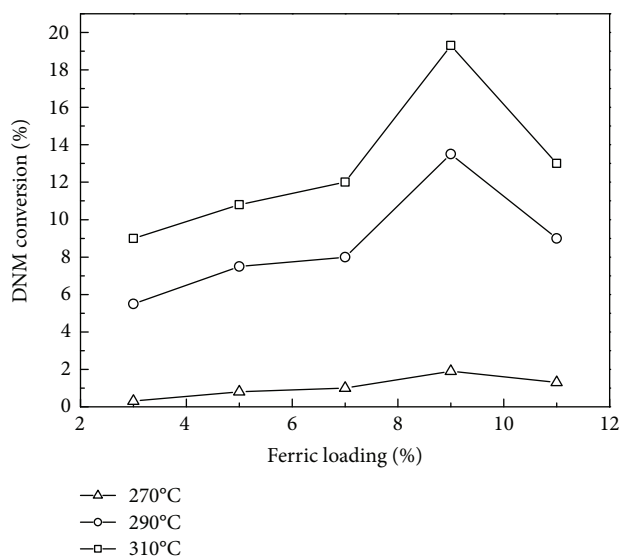
Figure 1: Effect of Fe loading on DNM conversion rate.

autoclave. After replacing air for 3 times, the autoclave was pressurized to 5 MPa with nitrogen and heated to 310°C within 15 min. The autoclave was cooled to room temperature in an ice-water bath after being kept at 310°C for 1 h. The reaction mixture was taken out and filtered through a 0.8 μm membrane filter, and the residue from GBC (RGBC) was dried in vacuum at 80°C for 6 h.

The RGBC (1 g), Fe_2S_3/AC-T catalyst (0.5 g), and cyclohexane (50 mL) were put into a 100 mL stainless, magnetically stirred autoclave. After replacing air for 3 times, the autoclave was pressurized to 0.8 MPa with hydrogen, heated to 310°C within 15 min, and kept at the temperature for 1 h. Then the autoclave was immediately cooled to room temperature in an ice-water bath. The reaction mixture was taken out from the autoclave using petrol ether as the rinse solvent and filtered through a 0.8 μm membrane filter. The filtrate was concentrated by evaporating the solvents using a rotary evaporator and then analyzed with a Hewlett–Packard 6890/5973 GC/MS.

3. Results and Discussion

Figure 1 shows the dependence of DNM conversion on the Fe loading of Fe_2S_3/AC-T. At 270°C, the conversion rate of DNM over Fe_2S_3/AC-T with various Fe loading was below 1%. When the reaction temperature increased to 290 or 310°C, with the increases of Fe loading (3% to 9%), the DNM conversion rate increased and reached a maximum of 13.5% at 290°C and 19.3% at 310°C. With further increase of Fe loading, the DNM conversion rate decreased to 9% at 290°C and 13% at 310°C. The results indicated that 9% of Fe loading is appropriate for the catalyst and excessive ferric sulfide may result in a decrease of specific surface area, which in turn reduce the catalytic efficiency. The hydrocracking of DNM is an endothermic reaction, and higher temperature is favorable for the reaction. It can be seen in Figure 1 that a high DNM conversion was got under a mild condition (reaction temperature of 310°C).
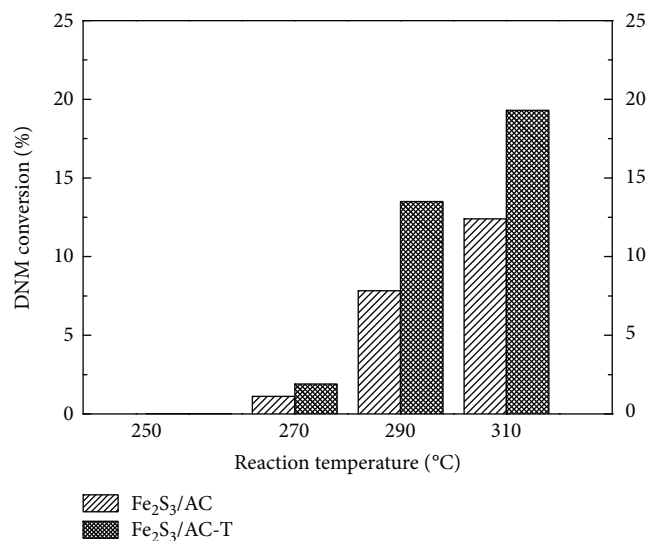
FIGURE 2: DNM conversion rates with two kinds of catalysts at different temperatures.
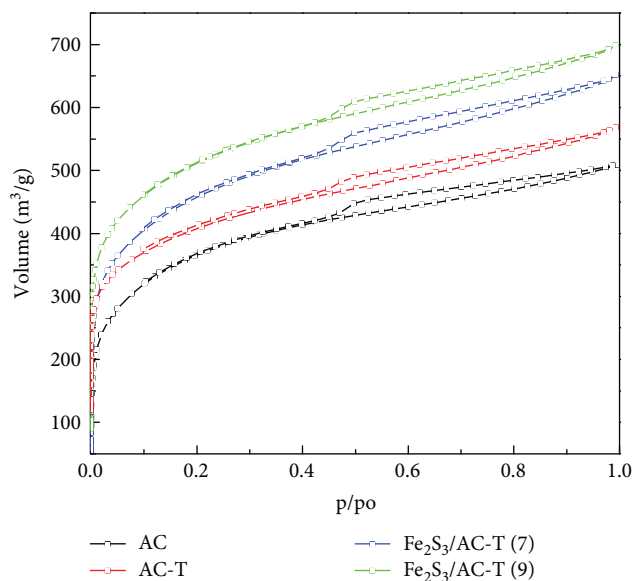
FIGURE 3: N$_2$ adsorption-desorption isotherms of supports and catalysts.

FIGURE 4: Micropore-size distribution (a) and mesopore-size distribution (b) of carriers and catalysts.

The catalytic activities of the catalysts Fe$_2$S$_3$/AC (9) and Fe$_2$S$_3$/AC-T (9) were compared in Figure 2, which summarizes the DNM conversions under different reaction temperatures. At 250°C, the DNM conversion was close to zero. As the reaction temperature rised to 270°C, the DNM conversion over Fe$_2$S$_3$/AC (9) and Fe$_2$S$_3$/AC-T (9) were 1.12% and 1.9%, respectively. With further increase of reaction temperature to 290°C, the DNM conversion increased greatly, 7.85% over Fe$_2$S$_3$/AC (9) and 13.5% over Fe$_2$S$_3$/AC-T (9), respectively. At 310°C, the DNM conversion reached 12.4% and 19.3% over Fe$_2$S$_3$/AC (9) and Fe$_2$S$_3$/AC-T (9), respectively.

It is believed that the H$_2$S species, generated by ferric sulfate and hydrogen gas under enhanced temperature and pressure, further react with the C-C-bridged bonds of DNM to form naphthalene and methyl naphthalene. In our study, the support AC-T was obtained by impregnating the AC to sulfuric acid solution, and the catalyst Fe$_2$S$_3$/AC-T was coated with a layer of acid sites. The acid sites are helpful to the cleavage of C-C-bridged bonds. The catalyst Fe$_2$S$_3$/AC-T was more active than the Fe$_2$S$_3$/AC, which could be ascribed to the synergy effects of ferric sulfate and acid sites in the catalyst.

N$_2$ adsorption-desorption isotherms of supports and catalysts are shown in Figure 3. Those of AC, AC-T, Fe$_2$S$_3$/

TABLE 1: The surface properties of AC support and the catalysts.

Samples	SSA (m^2/g)	TPV (cm^3/g)	V mic (cm^3/g)	D_{BJH} (nm)	D_{HK} (nm)
AC	1485.7	0.8625	0.7259	2.3221	0.5875
AC-T	1017	0.691	0.5264	2.7178	0.51
Fe$_2$S$_3$/AC-T (7)	1465.7	0.9389	0.7538	2.5623	0.5375
Fe$_2$S$_3$/AC-T (9)	1508.1	0.9581	0.7654	2.5412	0.6125
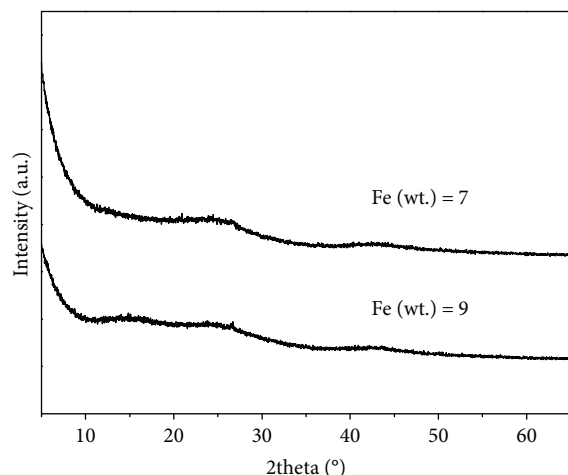
FIGURE 5: XRD patterns of the catalysts.

AC-T (7) and Fe$_2$S$_3$/AC-T (9) exhibited a mixture of type and type isotherms, with a wider knee exhibited at relative pressure (p/p0) < 0.1. This indicated wider micropores. An obvious capillary condensation step (hysteresis loop) at p/p0 > 0.4 indicated that a considerable amount of mesoporous was also present. Mesopore- and micropore-size distributions are shown in Figures 4(a) and 4(b), respectively, and the specific surface area, total pore volume, and pore diameter of the support AC and the catalyst Fe$_2$S$_3$/AC-T are listed in Table 1. It can be seen that AC has a high specific surface area and a high percentage of micropores and the pore-size distribution was predominantly 0.5–0.8 nm. After treated by sulfuric acid, the specific surface area and total volume of AC-T decreased about 30% and 18%, respectively. The micropore size becomes nonuniform and has a wide range of distribution. Compare to the support AC-T, the Fe$_2$S$_3$/AC-T catalysts have a significantly higher specific surface area and total pore volume. It may be ascribed to the loose structure of ferric sulfate on the support. A certain amount of micropores was also formed during impregnation. The values of specific surface area and total pore volume reach the maximum at the Fe loading of 9 wt.%. Combined with the catalytic performance exhibited in Figures 1 and 2, the optimal loading of Fe is 9 wt.%.

The XRD patterns of the catalyst Fe$_2$S$_3$/AC-T with different ferric sulfate loading are shown in Figure 5. The broad diffraction peak showed between $2\theta = 20\sim30°$ is ascribed to the support AC. It is obvious that the catalyst only exhibited the diffraction peak of support AC. The absence of diffraction peaks of ferric substance can be ascribed to its well dispersion on the AC surface.
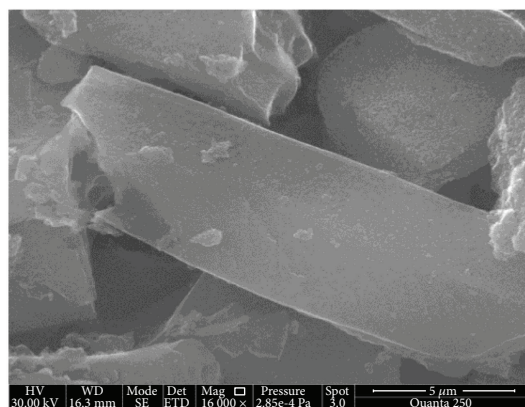
(a)
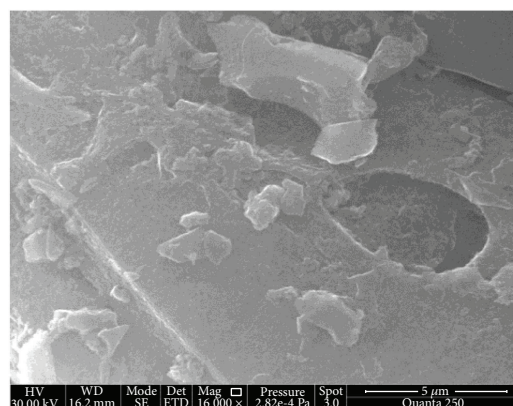
(b)

FIGURE 6: SEM images of AC (a) and Fe$_2$S$_3$/AC-T (b).

As Figure 6 displays, the surface of AC support is smooth, and the surface of catalyst Fe$_2$S$_3$/AC-T (9) is rough. There are irregular bulks adhered to the AC surface. Combined with the XRD results, the bulks of ferric sulfate are well dispersed on the AC surface.

Total ion chromatogram of the filtrate of reaction mixture from catalytic hydroconversion of RGBC is shown in Figure 7. 18 compounds were identified and listed in Table 2. Five arenes and 13 alkanes were identified. It indicated that the Fe$_2$S$_3$/AC-T significantly catalyzed the hydroconversion of RGBC and forms GC/MS-detectable species.

4. Conclusions

Ascribed to the synergy effects of ferric sulfate and acid sites, the Fe$_2$S$_3$/AC-T exhibited a benign catalytic performance for DNM hydrocracking.
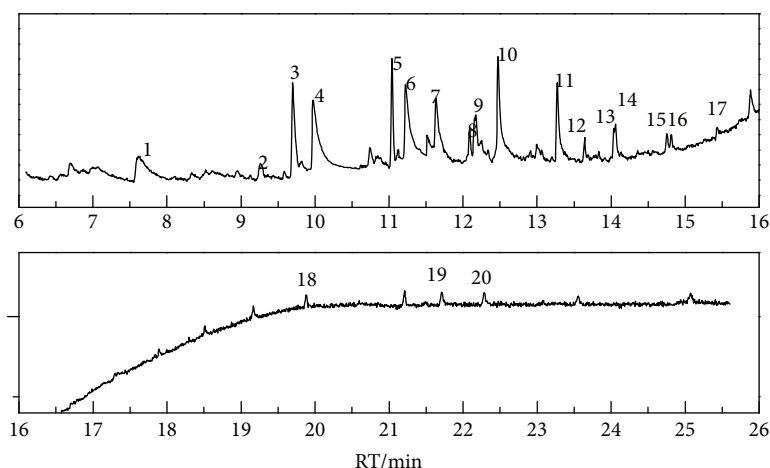
FIGURE 7: Total ion chromatogram of the filtrate of reaction mixture.

TABLE 2: The compounds detected in the reaction mixture.

Peaks	RT (min)	Compounds
Arenes		
1	7.63	1,2,3-Trimethyl-benzene
2	9.27	1,2,3,4-Tetramethyl-benzene
3	9.7	1,2,3,4-Tetrahydro-naphthalene
4	9.98	Naphthalene
6	11.23	2-Methyl-naphthalene
Alkane		
5	11.04	Bicyclohexyl
7	11.64	Tetradecane
8	12.09	1-Cyclohexylmethyl-4-methyl-cyclohexane
9, 16	12.16	2,6,10-Trimethyl-dodecane
10	12.48	Tridecane
11	13.27	Hexadecane
12	13.64	5-Ethyl-decane5
13, 19	14.03	Octadecane
14	14.06	2,6,10-Trimethyl-pentadecane
15, 18	14.75	Eicosane
17	15.44	Pentadecane
20	22.68	Nonadecane

The Fe_2S_3/AC-T significantly catalyzed the hydroconversion of RGBC and forms GC/MS-detectable species. Five arenes and 13 alkanes were identified in the filtrate of reaction mixture.

Conflicts of Interest

The authors declare that they have no conflicts of interest.

Acknowledgments

References

[1] H. H. Schobert and C. Song, "Chemicals and materials from coal in the 21st century," *Fuel*, vol. 81, no. 1, pp. 15–32, 2002.

[2] H. F. Shui, Z. P. Cai, and C. B. Xu, "Recent advances in direct coal liquefaction," *Energies*, vol. 3, no. 2, pp. 155–170, 2010.

[3] H. R. Zhou, S. Y. Yang, H. H. Xiao, Q. H. Yang, and L. Gao, "Modeling and techno-economic analysis of shale-to-liquid and coal to liquid fuels processes," *Energy*, vol. 109, pp. 201–210, 2016.

[4] Z. Y. Luo and M. Agraniotis, "Coal-to-liquids and polygeneration using low rank coals," in *Low Rank Coals for power generation, Fuel and Chemical Production*, pp. 241–268, Woodhead Publishing, Duxford, UK, 2017.

[5] K. Miura, "Mild conversion of coal for producing valuable chemicals," *Fuel Processing Technology*, vol. 62, no. 2-3, pp. 119–135, 2000.

[6] Z. P. Lei, S. F. Zhang, W. Lian, H. F. Shui, and S. B. Ren, "Study on mild hydrogenation of Xianfeng lignite in ionic liquid," *Journal of Fuel Chemistry and Technology*, vol. 41, no. 8, pp. 922–927, 2013.

[7] J. C. Yan, Z. Q. Bai, P. Hao, J. Bai, and W. Li, "Comparative study of low temperature pyrolysis and solvent treatment on upgrading and hydro-liquefaction of brown coal," *Fuel*, vol. 199, no. 1, pp. 598–605, 2017.

[8] X. Y. Wei, E. Ogata, and E. Niki, "Catalyses of Fe and FeS$_2$ on the reaction of di(1-naphthyl)methane," *Chemistry Letters*, vol. 20, no. 12, pp. 2199–2202, 1991.

[9] K. Hirano, M. Kouzu, T. Okada, M. Kobayashi, N. Ikenaga, and T. Suzuki, "Catalytic activity of iron compounds for coal liquefaction," *Fuel*, vol. 78, no. 15, pp. 1867–1873, 1999.

[10] T. Kaneko, K. Tazawa, N. Okuyama, M. Tamura, and K. Shimasaki, "Effect of highly dispersed ion catalyst on direct liquefaction of coal," *Fuel*, vol. 79, no. 3-4, pp. 263–271, 2000.

[11] Z. H. Ni, Z. M. Zong, L. F. Zhang et al., "Reactivities of di(1-naphthyl)methane toward hydrocracking over Ni-S," *Energy & Fuels*, vol. 16, pp. 1154–1159, 2002.

[12] Z. C. Wang, H. F. Shui, D. X. Zhang, and J. S. Gao, "A comparison of FeS, FeS + S and solid superacid catalytic properties for coal hydro-liquefaction," *Fuel*, vol. 86, no. 5-6, pp. 835–842, 2007.

[13] Z. C. Wang, H. F. Shui, X. P. Gu, and J. S. Gao, "Study on the direct liquefaction reactivity of Shenhua coal catalyzes by SO_4^{2-}/ZrO_2 solid acid," *Journal of Fuel Chemistry and Technology*, vol. 38, no. 3, pp. 257–263, 2010.

[14] S. G. Kang, Z. M. Zong, H. F. Shui, Z. C. Wang, and X. Y. Wei, "Comparison of catalytic hydroliquefaction of Xiaolongtan lignite over FeS, FeS+S and SO_4^{2-}/ZrO_2," *Energy*, vol. 36, no. 1, pp. 41–45, 2011.

[15] X. Fan, G. F. Liu, Z. M. Zong et al., "Mechanism for catalytic hydrodenitrogenation of isoquinoline," *Fuel Processing Technology*, vol. 106, pp. 661–665, 2013.

[16] C. Y. Wang, J. Mu, and C. L. Wu, "Research and development of direct coal liquefaction catalyst," *Coal Science and Technology*, vol. 4, pp. 24-25, 1998.

[17] X. Li, S. Hu, L. Jin, and H. Hu, "Role of iron-based catalyst and hydrogen transfer in direct coal liquefaction," *Energy & Fuels*, vol. 22, no. 2, pp. 1126–1129, 2008.

[18] S. H. Weng, Y. Q. Wu, J. S. Gao, C. G. Zhao, and Z. Wu, "Mossbauer spectroscopic study of iron catalyst in coal hydroliquefaction—II. On the transformation and the action mechanism of iron sulphide in hydrogenation," *Journal of Fuel Chemistry and Technology*, vol. 18, pp. 97–102, 1990.

[19] L. J. Wang, Z. D. Cui, and S. K. Lui, "The application of Mossbauer spectroscopy to the study of coal catalytic liquefaction I. The transformation of iron catalysts during liquefaction," *Journal of Fuel Chemistry and Technology*, vol. 18, pp. 268–272, 1990.

[20] X. M. Yue, X. Y. Wei, B. Sun, Y. H. Wang, Z. M. Zong, and Z. W. Liu, "Solid superacid-catalyzed hydroconversion of an extraction residue from Lingwu bituminous coal," *International Journal of Mining Science and Technology*, vol. 22, no. 2, pp. 251–254, 2012.

[21] X. M. Yue, X. Y. Wei, B. Sun et al., "A new solid acid for specifically cleaving the C_{ar}-C_{alk} bond in di(1-naphthyl)-methane," *Applied Catalysis A: General*, vol. 425-426, pp. 79–84, 2012.

Review Article

Structural Characterization of Lignin and Its Degradation Products with Spectroscopic Methods

Yao Lu,[1,2,3] Yong-Chao Lu,[4] Hong-Qin Hu,[3] Feng-Jin Xie,[3] Xian-Yong Wei,[1,3] and Xing Fan[1,3]

[1]Key Laboratory of Coal Processing and Efficient Utilization, Ministry of Education, China University of Mining & Technology, Xuzhou 221116, China
[2]Advanced Analysis & Computation Center, China University of Mining & Technology, Xuzhou 221116, China
[3]School of Chemical Engineering and Technology, China University of Mining & Technology, Xuzhou 221116, China
[4]School of Basic Education Sciences, Xuzhou Medical University, Xuzhou 221004, China

Correspondence should be addressed to Xing Fan; fanxing@cumt.edu.cn

Lignin is highly branched phenolic polymer and accounts 15–30% by weight of lignocellulosic biomass (LCBM). The acceptable molecular structure of lignin is composed with three main constituents linked by different linkages. However, the structure of lignin varies significantly according to the type of LCBM, and the composition of lignin strongly depends on the degradation process. Thus, the elucidation of structural features of lignin is important for the utilization of lignin in high efficient ways. Up to date, degradation of lignin with destructive methods is the main path for the analysis of molecular structure of lignin. Spectroscopic techniques can provide qualitative and quantitative information on functional groups and linkages of constituents in lignin as well as the degradation products. In this review, recent progresses on lignin degradation were presented and compared. Various spectroscopic methods, such as ultraviolet spectroscopy, Fourier-transformed infrared spectroscopy, Raman spectroscopy, and nuclear magnetic resonance (NMR) spectroscopy, for the characterization of structural and compositional features of lignin were summarized. Various NMR techniques, such as ^{1}H, ^{13}C, ^{19}F, and ^{31}P, as well as 2D NMR, were highlighted for the comprehensive investigation of lignin structure. Quantitative ^{13}C NMR and various 2D NMR techniques provide both qualitative and quantitative results on the detailed lignin structure and composition produced from various processes which proved to be ideal methods in practice.

1. Introduction

The main components of lignocellulosic biomass (LCBM) are cellulose, hemicellulose, and lignin. Cellulose is a polymer of glucose, accounting for 30–50 wt% of dry LCBM; hemicellulose is a mixture of heteropolymers containing various polysaccharides, such as xylan, glucuronoxylan, and glucomannan, accounting for 20–35 wt%; the mainly remaining portion with 15–30 wt% is lignin, which is a multisubstituted phenolic polymer. Lignin is the most abundant aromatic biopolymer accounting for up to 30% of the organic carbon on Earth and thus can be treated as a potential renewable feedstock for energy supplement and aromatic chemicals production [1, 2]. The annual production of lignin is more than 70 million tons [3]. The most abundant industrial

lignins are produced from kraft and sulfite pulping processes in the pulp and paper industries, so-called black liquor. However, only less than 2% of the lignin produced from pulping industries was value-addedly utilized, while the rest was abandoned or burned as a low-value fuel for energy supplement [4], leading to serious waste of precious aromatic resource and environmental pollution.

Lignin is an amorphous, irregular three-dimensional, and highly branched phenolic polymer. The functions of lignin in the plant cell wall are to cover structural support, transport water and nutrients, and issue protection to prevent chemical or biological attacks, and so forth. Though the chemical structure is extremely complex, it is generally accepted that lignin is formed via irregular biosynthesis process constructed from three basic phenylpropanoid monomers,

R = H or −OCH$_3$
L = lignin
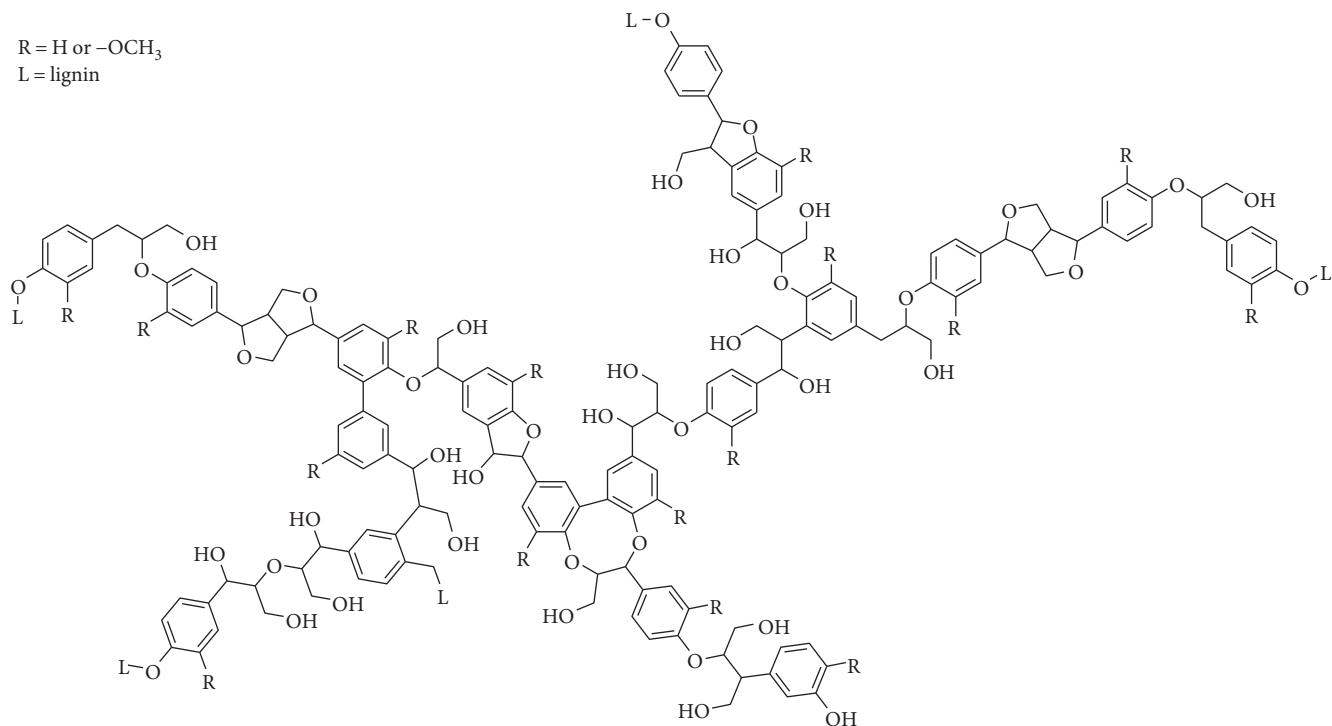
Figure 1

p-hydroxyphenyl (H), guaiacyl (G), and syringyl (S) units, derived from p-coumaryl, coniferyl, and sinapyl alcoholic precursors, respectively. Figure 1 shows a typical structural model of lignin. Gymnosperms contain almost entirely G unit in lignins; dicotyledonous angiosperms contain G and S units in lignins; and all the G, S, and H units can be found in monocotyledonous lignins [5]. Other units with relatively fewer contents were also identified in the lignin of LCBM, such as ferulates and coumarates [6]. Biosynthesis of lignin is a process that monomers undergo radical coupling reactions to form racemic, cross-linked, and phenolic polymer, by which lignin content and composition may vary significantly in different LCBMs [7]. Furthermore, the structure of lignin even varies among different tissues and ages of the same individual of LCBM [8].

Typical lignin contents are 24–33% in softwoods, 19–28% in hardwoods, and 15–25% in grasses, respectively. Functional groups in lignin include methoxyl, carbonyl, carboxyl, and hydroxyl linking to aromatic or aliphatic moieties, with various amounts and proportions, leading to different compositions and structures of lignin [9]. Various linkages (see Figure 2) either in C-C or C-O type with different abundances formed in the coupling reactions involved in biosynthesis of lignin, including aryglycerol-β-ether dimer (β-O-4, 45–50%), biphenyl/dibenzodioxocin (5–5′, 18–25%), pino/resinol (β-5, 9–12%), diphenylethane (β-1, 7–10%), aryglycerol-α-ether dimer (α-O-4, 6–8%), phenylcoumaran (β-β′, 0–3%), siaryl ether (4-O-5, 4–8%), and spirodienon.

It is difficult to draw accurate structural diagram for entire lignin by using up-to-date techniques in situ. Although relative new methods for imaging and analyzing chemical structure of lignin, such as confocal Raman scattering microscopy [10] and time-of-flight secondary ion mass spectrometry [11, 12], can provide chemical and spectral imaging of lignin for the distribution of componental units with high resolution and sensitive, these techniques are only available in several biological labs and have not been employed widely by chemical scientific groups. Up to now, the comprehensive elucidation of structural and compositional features of lignin relies on the processes for the degradation and isolation of lignin from LCBM and methods applied in the characterization of the corresponding products [2, 13]. However, in the degradation process, the original structural and compositional features of lignin may be sometimes ambiguous or even missed. Different degradation processes produce different types of lignins with various structures and compositions; furthermore, a specific analytical technique gives partial and/ or limited information and is not able to provide a general picture for the entire lignin. The industrial applications of lignin are limited critically due to its complex nature and undefined chemical structure. For example, commercially purchased kraft lignins from softwoods may have different compositions as well as their structures [14]. Furthermore, the lignin-carbohydrate complex (LCC) increases the difficulty of structural analysis and isolation of lignin from LCBM [15]. The value-added utilization of lignin and its degradation products are one of the ultimate goals especially for biorefineries; therefore, the comprehensive understanding of the structure of lignin is crucial necessary, since it can provide theoretical direction on constructing and optimizing degradation processes, generating of valuable aromatic chemicals
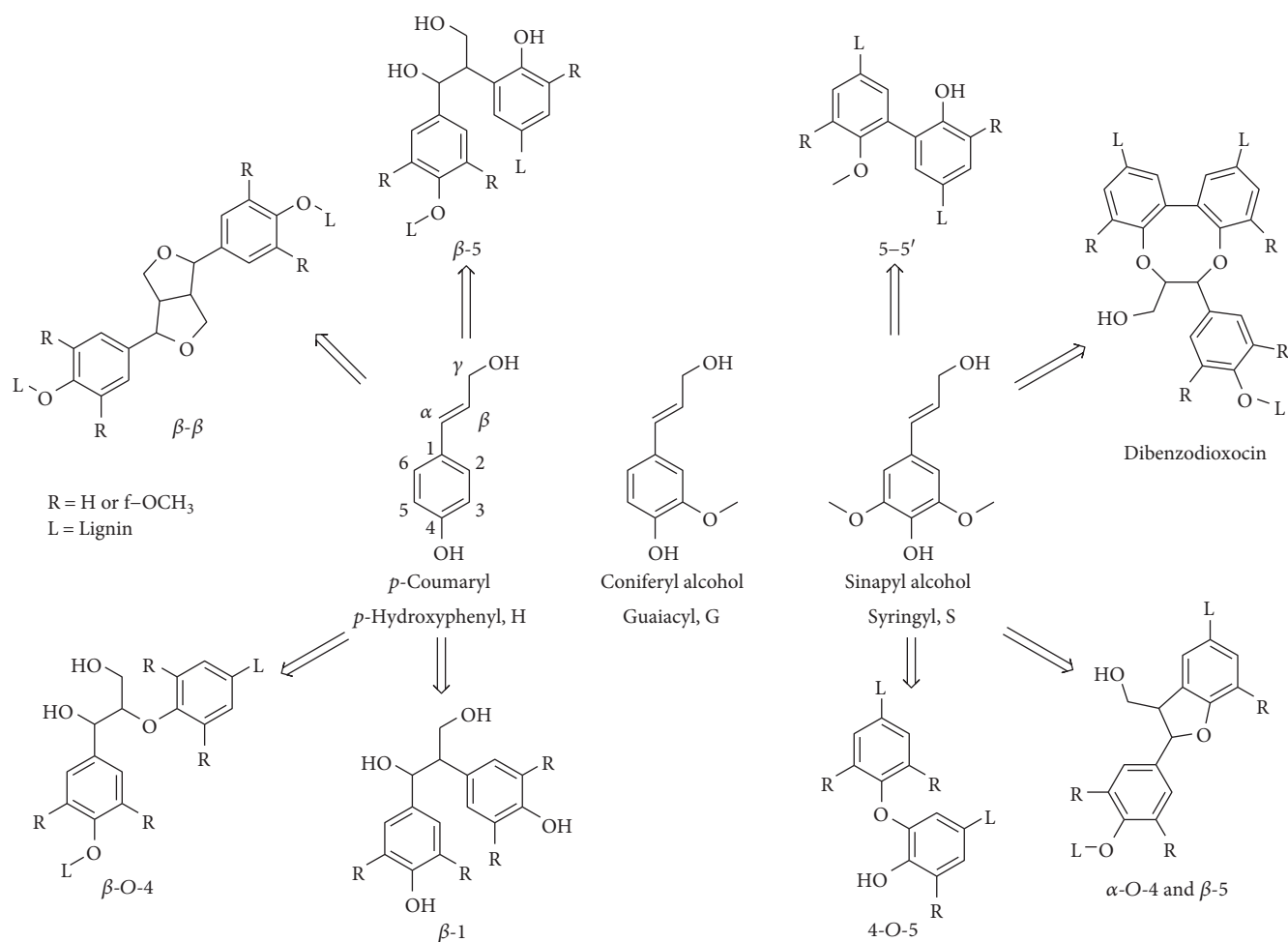
FIGURE 2

to act as low-molecular-mass feedstocks [16], estimating the economic viability, and so forth.

Traditionally, there are two ways to isolate lignin from other components in LCBM, so-called degradation processes: one is to extract cellulose and hemicellulose leaving most of the lignin as solid residue, and the other one is to extract lignin by using fractionation methods leaving the other components. For the former process, dilute sulfuric acid and hot water are often used to break down cellulose and hemicellulose releasing sugars and facilitating the further enzymatic hydrolysis, while leaving lignin as the main content in solid residue. For the later process, hydroxide solution, either with sodium, potassium or calcium, is used to remove lignin from LCBM samples. The degradation processes are designed to cleave the bonds between lignin and carbohydrates, leading to more or less extensive changes compared to native lignin structure. Consequently, the chemical compositional features of the resulting technical lignins, such as the relative abundance of S/G/H units, the status of side chains, and the contents of functional groups, are highly dependent on the methods and conditions used in degradation processes [17]. The most common linkages in lignin, namely, β-O-4 linkages, are relatively weak linkages

and are the key target of most degradation pretreatments. Other linkages, such as β-5, β-1, β-β', 5–5′, and 4-O-5, are more complicated and difficult to be degraded. Toward the structural investigation, various lignins are produced via different degradation processes, such as milled wood lignin (MWL), acidic lignin, sulfite lignin, soda lignin, kraft lignin, organosolv lignin, cellulolytic enzyme lignin (CEL), enzymatic mild acidolysis lignin (EMAL), and lignin from thioacidolysis process [2]. In the recent years, extraction and depolymerization with ionic liquids (ILs) for the isolation or degradation of lignins were considered to be promising processes [18, 19].

For the structural and compositional elucidation of complex samples, various instrumental methods were used. For example, the chromatographic techniques coupled to mass spectrometers and high-resolution mass spectrometric techniques were used extensively in the analysis of the bio-oil, biomass, and lignin samples [20–24]. These methods concentrate on the detection of individual species basing on the chromatographic separation and high molecular resolution. However, on the other hand, spectroscopic methods, such as ultraviolet spectroscopy (UV), Fourier-transformed infrared spectroscopy (FTIR), and nuclear magnetic resonance

(NMR), concern about the analysis of the whole structure and direct detection of moieties in samples over degradation techniques [25, 26]. Detailed spectrometric information related to structural features, including functional groups, bond types, and chemical state of atoms, can be obtained. Furthermore, both of the qualitative and quantitative analyses can be carried out simultaneously.

In this review, we focused on the recent development and interesting findings on the structural investigation of lignin with spectroscopic methods over various degradation processes. Structural and compositional characters of lignin samples produced from different degradation processes were presented and compared, and developments of spectroscopic methodologies on the qualitative and quantitative elucidation of lignin structure were also summarized. The degradation processes and instrumental methods involved in the detailed and comprehensive understanding of the lignin structure were prospected.

2. Degradation Processes of Lignin

Various physical/chemical methods were carried out for the degradation and isolation of lignin. Optimization or modification of these methods was conducted on various LCBMs due to the difference in the structure of lignin. In order to facilitate further structural and/or compositional analyses or to produce high purity lignin, modified or multistep processes were usually carried out.

2.1. Milled Wood Lignin. MWL is produced via the extraction of milled sample particles from LCBM with a neutral organic solvent (e.g., 1,4-dioxane) under mild conditions to remove other components. In the extraction process, only minor changes may occur with respect to the milled sample; hence, the obtained lignin has similar property with the milled sample. Nevertheless, MWL is not considered to be a representative of the original lignin in the LCBM due to its relative low yield (based on Klason lignin).

2.2. Cellulolytic Enzyme Lignin. In order to improve the yield, CEL was developed from the extraction of enzymatically hydrolyzed MWL residue. Typically, the residual carbohydrate contents in CEL account 10–15 wt% of initial MWL sample. The structure of CEL is similar to MWL, and it is more representative of total lignin in LCBM than in MWL. CEL has commonly been used for the structural analysis of lignin in the cell wall of plants. In a recent study, cellulolytic enzyme hydrolysis was carried out prior to water/dioxane extraction of MWL to remove carbohydrates. The lignin was obtained with high yield and purity [27]. Enzymatic lignin degradation has several advantages such as mild conditions and potentially fewer inhibitors for microbes. However, the degradation of lignin in LCBM still gave a very low yield of fragmented and soluble lignin, which may due to the limitations on efficient electron transfer [28] in the process.

2.3. Sulfite, Soda, and Kraft Lignins. Sulfite, soda, and kraft lignins are by far the main technical lignins produced via industrial processes. Among them, sulfite and kraft methods are sulfur-involving processes, accounting more than 90% of the chemical pulp production worldwide [29], and soda method is sulfur-free process. In the sulfite process, water-soluble lignosulfonates are formed. Further purification is needed to remove unexpected carbohydrate impurities. This process produces the largest amount of technical lignin. However, the obtained lignin contains considerable amount of sulfur. In the soda process, lignin is dissolved in hydroxide solution and following steps including precipitation, maturation, and filtration. In the kraft process, LCBM particles are emerged in an aqueous solution containing NaOH and Na$_2$S. Lignins are depolymerized as water-/alkali-soluble fragments with approximately 70–75% of the hydroxyl groups become sulfonated. Industrially, kraft lignin, produced chemically from the lignin degradation in aqueous alkali, is the major constituent of black liquor (90–95%). Neither kraft lignin nor sulfite lignin is suitable for investigating the original native structures of lignins, because significant structural changes occur especially the cleavage of α-O-4 and β-O-4 linkages under the conditions of these processes. Additionally, undesirable impurities such as sulfurous compounds or carbohydrates are present in derived lignin for these fractionation processes. Currently, almost all the produced technical lignins are only high yield industrial by-products and recovered as low-value fuel. This dilemma may rely on the progress in structural characterization of lignins from various LCBMs and the further upgrading of the technical lignins targeting value-added chemical production.

2.4. Organosolv Lignin. In the organosolv process, high purity lignin and cellulose are produced at the same time with various solvents; however, no technical lignins are commercially available from this process up to now. Organosolv process typically results in more than 50% lignin removal from LCBM through cleavage of lignin-carbohydrate bonds and β-O-4 linkages. The separation of organosolv lignin can be achieved either by removing of the solvent or by precipitation with water followed by distillation. Most organosolv lignin is easily soluble in basic solutions and polar solvents, that is, ethanol or ethanol/water mixture, but will be insoluble in acidic aqueous solutions. Organosolv lignin is sulfur-free, high purity, and rich in functionality including phenolics, exhibits a narrow polydispersity, and has limited carbohydrate contamination.

The extraction conditions affect the structure of organosolv lignin, that is, severity factor (H-factor). The molecular weight of the ethanol organosolv lignin decreased within a 36–56% range with respect to the MWL with the increase of the severity. Moreover, an obvious decrease in the content of aliphatic hydroxyl groups and an increase of syringyl phenolic units and condensed phenolic structures with the increase in severity of the organosolv treatment were also observed [30]. An integrated process of hot water extraction followed by high-boiling-solvent cooking with 1,4-butanediol can fractionate bagasse vigorously into cellulose, hemicelluloses, and lignin. The organosolv lignin formed exhibited a chemical structure similar to EMAL with more newly formed phenolic OH groups [31].

2.5. Acidic Lignin. Traditionally, in the acidolysis process, lignin is extracted from LCBM sample with 1,4-dioxane containing hydrochloric acid under room temperature. The obtained lignin with high purity is considered to be a representative of the original lignin. However, a limitation of this process is that the same conditions used to hydrolyze polysaccharides also degrade the liberated monosaccharides, leading to overestimate monosaccharide degradation and introducing bias between polysaccharides of different liability. Modifications were introduced to reduce these errors [32]. A modified acidolysis process was carried out by Gong et al. [33]. The acetic acid lignin from bamboo shoot shell had a higher yield of lignin (74 wt%) and lower content of associated carbohydrates (2.96 wt%) than MWL (5.16 wt%). Additionally, acetic acid lignin possessed a molecular weight 2789 Da and a narrow polydispersity index (i.e., $M_w/M_n = 1.54$). Higher phenolic hydroxyl group content and S/G ratio were also obtained in this lignin compared to MWL [33]. Enzymatic mild acidolysis lignin (EMAL) is obtained from acidolysis of CEL with dilute acid, such as hydrochloric acid. The remaining carbohydrates linking to lignin can be removed further in the acidolysis producing lignin with higher purity [34].

2.6. Thioacidic Lignin. Modified acidolysis processes were carried out to produce lignin with high yield and purity. Thioacidolysis process, in which ethanethiol is used instead of water, produced more lignin and less complex monomer mixtures. In this process, thioethylated H, G, and S monomers by the cleavage of β-O-4 ether linkages are produced. Traditional thioacidolysis methods require several steps before down streaming analysis or further treatments. Hence, higher-throughput quantitative method is needed for screening various types of LCBMs [35].

2.7. Ionic Liquid Degradation Lignin. IL provides an alternative path for lignin removal to classic organosolv pretreatment for enhancing subsequent enzymatic hydrolysis and isolation. Some ILs, such as 1-ethyl-3-methylimidazolium acetate, can extract lignin from poplar and birch with most structural features retained [36]. Some acidic ILs, such as 1-*H*-3-methylimidazolium chloride, will hydrolyze ether linkages [37] and further degrade lignin. The following are some recent progresses concentrated on the lignin degradation and isolation by ILs.

The ILs containing 1-butyl-3-methylimidazolium (bmim), 1-ethyl-3-methylimidazolium (emim), and 1-allyl-3-methylimidazolium (amim) cations either with acetate or chloride as the anions are commonly used in the lignin dissolution [38]. ILs have the capability to disrupt various linkages between the components in the LCBM by the formation of several types of interactions such as hydrogen bond, dipole-dipole, and van der Waals interactions [39]. Pyridinium formate (PyFor) showed a high capacity for the dissolution of kraft lignin (70 *w/w*%) at a relatively lower temperature (75°C) [40].

Cholinium ILs are novel bio-ILs used in the lignin valorization, in which different chemical reactions take place during the lignin dissolution from imidazolium ILs [41]. In the dissolution of kraft lignin in cholinium ILs, significant changes in the structure and thermal properties of kraft lignin occurred via depolymerization, dehydration, and demethoxylation followed by recondensation. Thermal properties of kraft lignin were altered, that is, increased the maximal decomposition temperature (T_m) and glass transition temperature (T_g); and the molecular weights were reduced after regeneration from cholinium ILs [41].

Other ILs, such as 1-ethyl-3-methylimidazolium xylenesulfonate [emim][ABS] and 1-butyl-3-methylimidazolium methylsulfate [bmim][MeSO$_4$], could promote depolymerization of organosolv lignin and Klason lignin under the oxidative conditions using a Cu/EDTA complex in the presence of a monomeric phenol (4-tert-butyl-2,6-dimethylphenol) [42].

An acidic IL, called 1-(4-sulfobutyl)-3-methyl imidazolium hydrosulfate ([C$_4$H$_8$SO$_3$Hmim]HSO$_4$), was proven to be an efficient catalyst for direct liquefaction of bagasse lignin, where more than 65% degree of liquefaction and 13.5% yield of phenolic monomer without any char formation [43].

A switchable ionic liquid (SIL), synthesized from 1,8-diazabicyclo[5.4.0]undec-7-ene (DBU), monoethanol amine (MEA), and CO$_2$, named CO$_2$-switched [DBU][MEASIL], was demonstrated to have high ability to extract the interlinked polysaccharide impurities from the sodium lignosulfonate while the linkages and aromatic subunits remain unaffected during the dissolution-recovery cycle. This SIL can be used as an affordable solvent medium to obtain carbohydrate-free lignin from an impure lignin source [44].

Future developments on the IL degradation of lignin will focus on selective lignin extraction/degradation and functionalization as well as minimization of process costs for recovery and recycling of ILs.

2.8. Multistep Processes. Multistep processes were used to enhance the removal of lignin. A two-step process was carried out in which anhydrous ammonia pretreatment was followed by mild NaOH extraction on corn stover to solubilize and fractionate lignin [45]. Lignin removal of more than 65% with over 84% carbohydrate retention was achieved. Furthermore, a significant reduction in the weight-average molecular weight (M_w) of extracted lignin was also achieved. Synergistic effects were found in the combination of pretreatments to enhance the isolation or conversion of lignins [28, 46]. In the sequential fractionation of *Tamarix spp.*, MWL, organosolv lignin, and alkaline lignin were conducted with dioxane, alkaline organosolv, and alkaline solutions, respectively. The results indicated that the alkaline organosolv extraction released a higher yield of lignin (17.7%) than dioxane and alkaline solution extractions. Small amounts of carbohydrates (0.79%) were detected in the organosolv lignin fraction, suggesting a significant cleavage of α-ether bonds between lignin and carbohydrates in the alkaline organosolv fractionation process [47].

2.9. Comparison of the Processes. Alkaline lignins were found to have higher carbohydrate content (up to 30 wt%) with higher molecular weights around 3000 Da; on the other hand, organosolv lignins had considerable high purity (better than

93 wt%) with molecular weights in the range of 600–1600 Da [48]. The structure and composition of alkali lignin, CEL, and MWL from valonea of *Quercus variabilis* Blume were compared by Yang et al. [49]. The isolation processes of alkali lignin and CEL caused some damages to the structure of lignin. The β-O-4 linkages were largely cleaved during the CEL process since the relative content of β-O-4 linkages in CEL was much lower than those in alkali lignin and MWL. High S/G ratio for alkali lignin was observed, indicating that the S-units were easily released under the alkali conditions.

Yang et al. [50] compared four lignins produced from valonea of *Quercus variabilis*, namely, ethanol lignin, alkali lignin, MWL, and enzyme hydrolysis lignin (EHL). The results showed that the four lignins contained GSH-type with little differences. The MWL contained the least functional groups with the poorest thermostability and the highest antioxidant activity. The EHL had the highest molecular weight (i.e., $M_w = 1429$ g/mol; $M_n = 746.18$ g/mol). In a comparison of pretreatments on hardwood (red oak), softwood (loblolly pine), and herbaceous biomass (corn stover) for lignin valorization through pyrolysis, organosolv lignins contained fewer volatiles in comparison to the corresponding MWLs for all the tested samples [51]. Red oak lignin was affected mostly by the organosolv process, since the greatest decrease in volatile content and increase in carbon content were observed. Corn stover lignin had the highest potential for volatilization because it retained highly branched polymer structure enriched in tricin, ferulate, and coumarate groups.

Clearly, different degradation processes or pretreatments have significant influence on the compositional and structural features of lignin. The selectivity and efficiency of these processes are the main consideration. To elucidate the original structure of lignin, relatively undestroyed and effective degradation methods are feasible, such as IL extraction and organosolv process. To produce value-added chemical from lignin, more aggressive methods aiming at the cleavage of the weak linkages in lignin (i.e., β-O-4 linkages) and the interunits between lignin and polysaccharides can be used in the degradation process. Of course, biological conversion with suitable selectivity might be another orientation for degradation of lignin [52].

3. Spectroscopic Methods

Structural investigation of lignin with spectroscopic techniques has been considered to be promising high-throughput and routine methods, which can provide detailed qualitative and quantitative information on structural features including functional groups, types of chemical bonds, and states of atoms.

3.1. UV Spectroscopy. The content of acid-soluble lignin, the purity, and the components of isolated lignin, can be determined by using UV spectroscopy [53]. National Renewable Energy Laboratory (NREL) proposed an accurate method for the determination of lignin, by which the absorbance of lignin was recorded at the recommended wavelength [54]. According to the intrinsic structure of lignin, several absorption maxima attributed to different functional groups were

TABLE 1: UV spectroscopic absorptions of typical structures in lignin [25, 30, 50, 53–56].

Absorption maxima/nm	Electronic transition style	Chromophores and structures
200	π-π^*	Conjugated bonds/aromatic ring
240	n-π^*	Free -OH
282	π-π^*	Conjugated bonds/aromatic ring
320	π-π^*	Aromatic ring conjugated bond with C = C
320	n-π^*	C = O groups conjugated to aromatic ring
325	n-π^*	Etherified ferulic acid
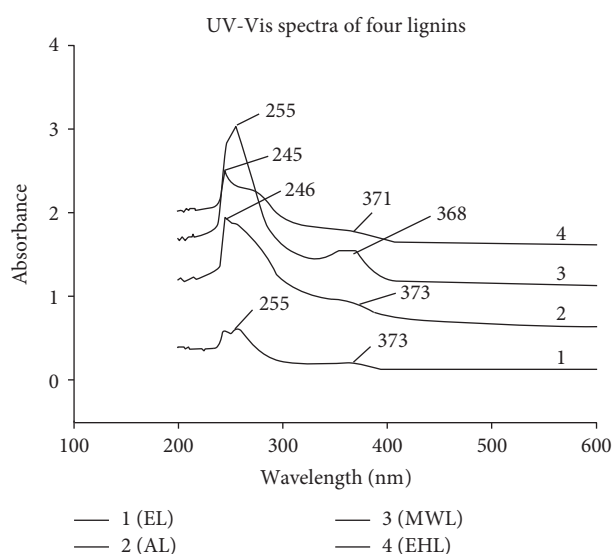
FIGURE 3

observed, as shown in Table 1 [25, 30, 50, 53–56]. The determination of phenolic hydroxyl groups can be achieved basing on the difference in absorption at 292 and 370 nm between phenolic units in neutral and alkaline solutions [30, 50, 55, 56]. Attributed to the symmetrical syringyl unit, the maximum absorbance of lignins produced from different processes exhibited a blue shift. Furthermore, an additional absorbance at approximately 370 nm due to the presence of conjugated phenolic hydroxyl groups was also observed [50] (see Figure 3).

Basing on the Lambert-Beer's Law, UV spectroscopy can be used for the semiquantitative determination of the purity of lignin and its degradation products by using extinction coefficient (EC) [57, 58]. Because of the cross-linking structures of lignin with carbohydrates, cellulose, and hemicelluloses, the isolation of pure lignin is extremely difficult. The low value of EC represents the high nonlignin substance content in the isolated lignin.

3.2. FTIR Spectroscopy. FTIR spectroscopy is the most widely used technique in the functional group determination basing

EMAL

AL

CL

Transmittance

4000   3500   3000   2500   2000   1500   1000   500

Wavenumbers/cm^{-1}
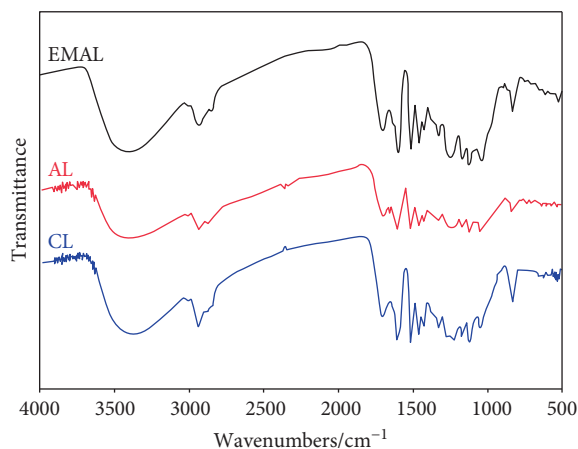
FIGURE 4

on the substances with chromophores. It can be treated as a nondestructive, noninvasive, highly sensitive, and rapid technique. Typical functional groups contained in lignin, such as hydroxyl, carbonyl, methoxyl, carboxyl, and aromatic and aliphatic C-H, can be assigned well in the FTIR spectrum. Figure 4 shows FTIR spectra for detection of different lignins, namely, EMAL, autocooking lignin (AL), and citric acid-catalyzed cooking lignin (CL) [31]. For the assignments of signals in FTIR spectra, Table 2 lists the typical wavelength assigned for possible functional groups and structures in lignin [25, 29, 38].

Attenuated total reflectance- (ATR-) FTIR could be used for the evaluation of kraft lignin in acylation with different acyl chlorides [59] and lignin structural changes during the cooking process with solid alkali and active oxygen [60]. FTIR spectroscopy could also characterize changes in the chemical structure of wood polymers in relation to the tree growth location and conditions [61]. Untreated solid samples (Norway spruce, *P. abies L. Karst.*) from three provenances in Europe were selected. Principal component analysis (PCA) and cluster analysis (CA) were used for evaluation of spectral data obtained by FTIR spectroscopy. The results showed that the samples belonging to the same wood species differ due to the origin. FTIR analysis was able to correctly discriminate samples originating from three different provenances in Europe.

It is known that functional properties of oxyethylated lignins (OELs) and the resulting substances are strongly affected by the degree of oxyethylation (DOE) of phenolic hydroxyl groups (OH$_{phen}$). Passauer et al. [62] found the strong linear correlations between OH$_{phen}$ contents of lignin/OEL and FTIR vibrations attributed to phenolic and aliphatic acetoxy groups. With appropriate calibration, FTIR spectroscopy combined with sample preacetylation is considered to be a promising tool for rapid and accurate determination of the DOE of OELs with qualitative and quantitative results.

3.3. Raman Spectroscopy. Raman spectroscopy, as the sister spectroscopic technique of FTIR, can provide complementary information on the structural features even for the

samples containing water. Furthermore, more absorption bands were detected with Raman spectroscopy than FTIR [63]. Generally, the assignments of the absorption bands in Raman spectra are similar with FTIR spectra.

Raman spectroscopy is suitable for the investigation of the chemical structure of lignin, because it can provide in situ determination on the cell wall of plants even with no sample preparation. However, when analyzing a lignin sample in solutions with various solvents, one should consider the environmental effects of the solvents [64]. Confocal Raman microscopy was used to investigate the structural changes of lignocellulosic cell walls during the dilute acid pretreatments. According to the intensity of the Raman images, the ratio of lignin/cellulose [I(1600 cm^{-1})/I(900 cm^{-1})] was low for oxalic acid-pretreated biomass compared to sulfuric acid-pretreated biomass [65].

3.4. NMR Spectroscopy. NMR spectroscopy provides more precise and comprehensive information on qualitative and quantitative assays for the frequencies of linkages and the composition of H/G/S units in the lignin analysis. The first discovery of dibenzodioxocine and spirodienone structures in lignin was carried out by Ralph et al. [66] and Zhang et al. [67], respectively. [1]H, ^{13}C, ^{19}F, and ^{31}P as well as various 2D NMR spectroscopic techniques can be used in the structural and compositional analyses of lignin. Among them, ^{1}H and ^{13}C NMR tend to be the regular tools for the analysis of lignin; and solid-state ^{13}C NMR and 2D heteronuclear single-quantum coherence (HSQC) NMR can provide accurate quantitative results on the functional groups and side chain moieties.

Compared with the spectroscopic methods mentioned above, NMR spectroscopic methods possess much higher resolution and enable a larger amount of information to be obtained. One-dimensional (1D) NMR methods, including ^{1}H, ^{13}C, ^{19}F, and ^{31}P NMR, and two-dimensional (2D) NMR methods, such as 2D HSQC NMR, were applied for the analysis of lignin samples with both solid and liquid states. The distribution of functional groups and amount of linkages and H/G/S units as well as other components in lignin can be qualitatively and quantitatively determined. The chemical shifts of functional groups in the spectra have been established.

^{1}H NMR is the method routinely used in the structural investigation of lignin, because of the simple preparation of samples and fast scanning speed. Almost all the compositional investigations of lignins use ^{1}H NMR for the detection of the chemical environment of proton. In the spectra, the signal observed around 7.5 ppm can be assigned to aromatic protons of H units and the other two chemical shifts around 7.0 ppm and 6.5 ppm are attributed to aromatic protons in G and S units, respectively [68, 69]. The chemical shifts in the range of 6.3–4.0 ppm are assigned to aliphatic protons in the linkages of β-O-4, β-β, and β-5. The signals in the range of 4.0–3.5 ppm are attributed to protons in methoxyl groups. The chemical shifts around 3.10 ppm may be attributed to the protons in anhydroxylose units [31, 70]. Typical peeks are assigned to functional groups in lignin, as shown in Table 3 [25, 31].

TABLE 2: Assignments of signals in FTIR spectrum to functional groups in lignin [25, 29, 38].

Wavenumbers/cm^{-1}	Assignments	Functional groups and structures in lignin
3400–3600	ν (O-H)	Free -OH
3100–3400	ν (O-H)	Associated -OH
2820–2960	ν (C-H)	-CH$_2$, -CH$_3$
2920	ν (C-H)	Carboxylic -OH
2650–2890	ν (C-H)	Methyl group in methoxyl
1771	ν (C = O)	Aromatic
1700–1750	ν (C = O)	Unconjugated ketones, carbonyls, and ester groups
1722	ν (C = O)	Aliphatic
1650–1680	ν (C = O)	Conjugated p-substituent carbonyl and carboxyl
1500–1600, 1420–1430	ν (aromatic skeletal)	Benzene ring
1450–1470, 1360–1370	ν (C-H)	-CH$_2$, -CH$_3$
1325–1330, 1230–1235	ν (C-O)	Syringyl ring
1270–1275	ν (C-O)	Guaiacyl ring
1215	ν (C-O)	Ether
1140–1145	ν (C-H)	Guaiacyl
1130	ν (C-H)	Syringyl
1085–1090	ν (C-O)	Secondary alcohol and aliphatic ether
1025–1035	ν (C-O, C-H)	Aromatic ring and primary alcohol
750–860	ν (C-H)	Aromatic ring

TABLE 3: Assignments of signals in ^{1}H NMR spectrum to typical functional groups in lignin (in CD$_3$Cl) [25, 31].

Chemical shift/ppm	Assignments
9.7–9.9	Cinamaldehydes and benzaldehydes
6.7–7.1	Aromatic-H in guaiacyl
6.2–6.7	Aromatic-H in syringyl
5.8–6.2	Benzylic OH in β-O-4 and β-1
4.9–5.1	Carbohydrates
3.3-4.0	Methoxyl
3.0–3.1	H$_\beta$ in β-1
2.2–2.4	Phenolic OH
1.6–2.2	Aliphatic OH

^{13}C NMR can be carried out to overcome the overlapping resonances of some structures in ^{1}H NMR spectra, providing qualitative and quantitative results with nondestructive detection of solid or solution samples. Although with a higher resolution, it is recommended that relative pure lignin sample is necessary in the ^{13}C NMR analysis, since the unexpected overlapping of spectra was due to the complexity of sample. Typical ^{13}C NMR spectra are shown in Figure 5 [31], and the assignments of signals are presented in Table 4 [31, 38, 49, 71]. By using the data from quantitative ^{13}C NMR, basic parameters which summarizes the main structural characteristics of lignins can be obtained, such as content of β-O-4 structures, degree of condensation, and unit ratio of S/G/H. Radar plots include these parameters and allow a direct classification of different lignins by comparison of the key descriptors [71]. Solid-state ^{13}C NMR analysis is a nondestructive method and not limited by sample insolubility. The cross-polarization/magic angle spinning (CP/MAS) method extensively used NMR technique for elucidating the structure of lignin. The detections take a very short time with high resolution; however, the quantitative analysis of CP/MAS is not sufficient enough [72]. Solid-state ^{13}C NMR is considered to be an advanced method for structural investigation of LCBM at atomic level; however, by using this technique, the structure remains largely unexplored due to the complexity of lignin and the severe spectral crowding of the responding signals [73]. A sensitive hyperpolarization solid-state NMR technique by combining high-field dynamic nuclear polarization (DNP) and MAS was used to improve the resolution of the determination [74]. Furthermore, this technique can provide 2D homonuclear ^{13}C-^{13}C correlation solid-state NMR spectra at natural isotopic abundance, yielding, and an atomic level structural investigation [75, 76]. Most of current lignin content analytical techniques require solo or sequential degradation or dissociation steps, which are time-consuming. By using the solid-state ^{13}C CP/MAS NMR technique with an internal standard (sodium-3-trimethylsilylpropionate, TMSP), a simple yet reliable method was established to analyze content of lignin in various LCBMs without destroying their native structures [77].

Constant et al. [78] carried out the quantification and classification of carbonyls in industrial humins and lignins by ^{19}F NMR. The carbonyl groups were transformed to corresponding hydrazone with 4-(trifluoromethyl)phenylhydrazine before quantification by ^{19}F NMR. By using model compound library, the carbonyl functional groups in Indulin Kraft and Alcell lignins were quantified and classified for the first time.
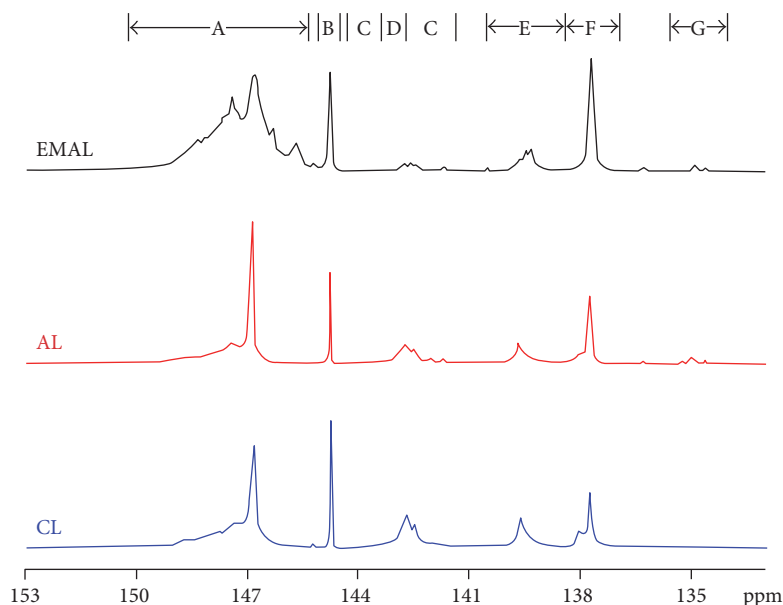
FIGURE 5

TABLE 4: Assignments of signals in ^{13}C NMR spectrum to functional groups in lignin [31, 38, 49, 71].

Chemical shift/ppm	Assignments
167–178	Unconjugated -COOH
162–168	Conjugated -COOH
140–155	C_3, C_4 aromatic ether or hydroxyl
127–140	C_1, aromatic C-C
123–127	C_5, aromatic C-C
117–123	C_6, aromatic C-H
114–117	C_5, aromatic C-H
106–114	C_2, aromatic C-H
78–90	Aliphatic C_β-O
67–78	Aliphatic C_α-O
54–57.5	Methoxyl

^{31}P NMR has also been widely used to quantitatively determine the amount of aliphatic and phenolic hydroxyl groups as well as carboxyl groups in lignin after phosphitylation with 2-chloro-4,4,5,5-tetramethyl-1,3,2-dioxaphospholane (TMDP) [29, 79, 80]. The high phenolic OH content reflecting the presence of condensed aromatic units, such as 5–5 units, was found by ^{31}P NMR in a biolignin produced by acetic acid/formic acid/water hydrolysis from wheat straw [81]. The ^{31}P NMR analysis of the insoluble fraction of kraft lignin provided an accurate and quantitative way to illustrate the effects of the laccase-HBT (1-hydroxybenzotriazole) system on lignin chemical bond cleavage [82]. Typical ^{31}P NMR spectra and signal assignments are shown in Figure 6 and Table 5, respectively [29, 82].

Solid-/solution-state ^{13}C NMR spectroscopes are powerful in lignin structural elucidation either in their solid or solution state. However, solid-state ^{13}C NMR spectroscopy is only suitable for the analysis of lignin samples that have restricted solubility and can observe some structural features of lignin due to its low resolution; and lignin is subjected to acetylation by anhydride/pyridine solution before the solution-state ^{13}C NMR spectrum collection [83] since dissolving lignin is difficult.

Various 2D NMR methods were carried out to overcome the overlapping of resonances in 1D NMR with higher resolution and providing more reliability to the assignments of the signals, especially in the determination of lignin [44, 84–93]. 2D NMR methods, such as heteronuclear multiple-quantum coherence (HMQC) spectroscopy, heteronuclear correlation (HETCOR) spectroscopy, homonuclear Hartmann-Hahn (HOHAHA) spectroscopy, total correlation spectroscopy (TOCSY), rotating frame Overhauser experiment spectroscopy (ROESY), heteronuclear single-quantum coherence (HSQC) spectroscopy, and heteronuclear multiple bond coherence (HMBC) spectroscopy, have been employed in lignin structure characterization [44, 84–86]. Among these, 2D HSQC NMR is the most extensively used due to its versatility in illustrating structural features and structural transformations of isolated lignin fractions. Figure 7 presents a typical investigation of lignin with accurate assignments of different structures [71]. 2D HSQC NMR is able to clearly characterize the structures of lignin and polysaccharides in cell walls and the linkages among the lignin without isolating each component [87]. Structural changes of lignin and the other components in LCBM in chemical reaction can be easily monitored by this method. The relationship between the degree of acetylation and the introduction positions of acetyl groups during the acetylation of ground pulp was investigated with 2D HSQC NMR [88]. Acetylation was found to occur firstly on the primary hydroxyl groups of polysaccharides and lignin, followed by the secondary hydroxyl groups of polysaccharides, and finally the hydroxyl groups at the α-position in lignin [88].
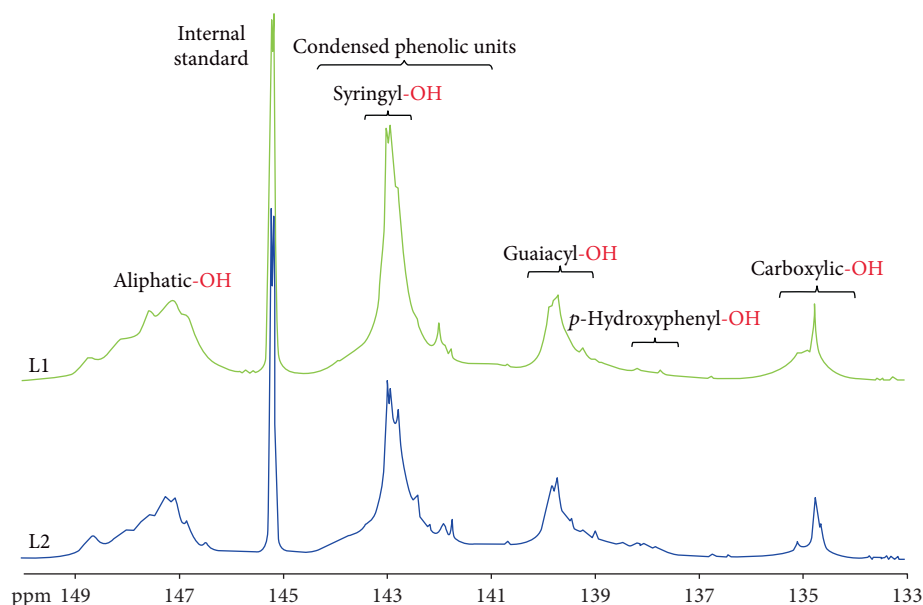
FIGURE 6

TABLE 5: Assignments of signals in ^{31}P NMR spectrum to hydroxyl groups in lignin [29, 82].

Chemical shift/ppm	Structural assignments
145.5–150.0	Aliphatic -OH
136.5–144.7	Phenols
140.0–144.5	C_5 substituted
143.5	β-5
142.7	Syringyl
142.3	4-O-5
141.2	5–5
139.0–140.0	Guaiacyl
138.2–139.0	Catechol
137.3–138.2	p-Hydroxyphenyl
133.6–136.6	Carboxylic acid -OH

Thioacidolysis was usually used as pretreatment before 2D HSQC NMR analysis in the characterization of the structures of the lignin monomers and oligomers [89]. Changes in the interunit linkage types during solvolysis were investigated. Lignin oligomers ranging from monomers to tetramers were released through considerable cleavage of the β-O-4 linkages [89]. In a study of various lignins derived from brewer's spent grain, 2D HSQC NMR revealed the substructures including β-O-4$'$ alkyl-aryl ethers (77–79%), β-5$'$ phenylcoumarans (11–13%), β-β' resinols (5-6%), and 5–5$'$ dibenzodioxocins (3–5%); while 2D HMBC NMR and derivatization followed by reductive cleavage analyses showed that p-coumarates were acylating at the γ-position of lignin side chains and were mostly occurred in condensed structures [90]. By using high-resolution 2D HSQC NMR, the chemical structures both on low and high molecular weight fractions of bio-oil derived from kraft lignin were determined. In the

degradation of kraft lignin to bio-oil, cleavages of both aliphatic carbon-oxygen (C-O) and to some extent carbon-carbon (C-C) bonds as well as repolymerization were observed simultaneously [91].

The combination of quantitative ^{13}C NMR and 2D HSQC NMR has been proven to be a powerful way in structural elucidation of complex samples since it takes advantage of the spectral dispersion afforded by the 2D spectrum to serve as an internal standard to measure the integral values obtained from the quantitative ^{13}C spectrum [92]. This method can overcome the severe overlap of signals and reduce errors in signal quantification due to differential line widths, quantitative abundance of S/G/H units, hydroxycin-namates, and tricin units, as well as various types of side chain substructures by selecting the proper internal standard reference signals [93]. Other combinations of NMR techniques were also reported; for instance, the existence of low energy dipole-dipole interactions and the absence of covalent bond between lignin and chitosan could be revealed clearly by solid-state ^{1}H-^{13}C CP/MAS NMR [94].

4. Conclusions

The comprehensive understanding of the lignin structure relies greatly on the developments of analytical strategies used, which is extremely important for the value-added utilization of biomass. Although significant progresses have been made in the degradation and isolation of the lignin from other components in LCBM, only a fraction of lignin can be identified and analyzed. Structure and composition of lignins from different LCBMs vary significantly according to both issue and age. Furthermore, the analytical results are strongly dependent on the degradation processes and instrumental equipment used.

For the structural investigation of lignin, undestroyed, selective, and efficient isolation methods should be built to
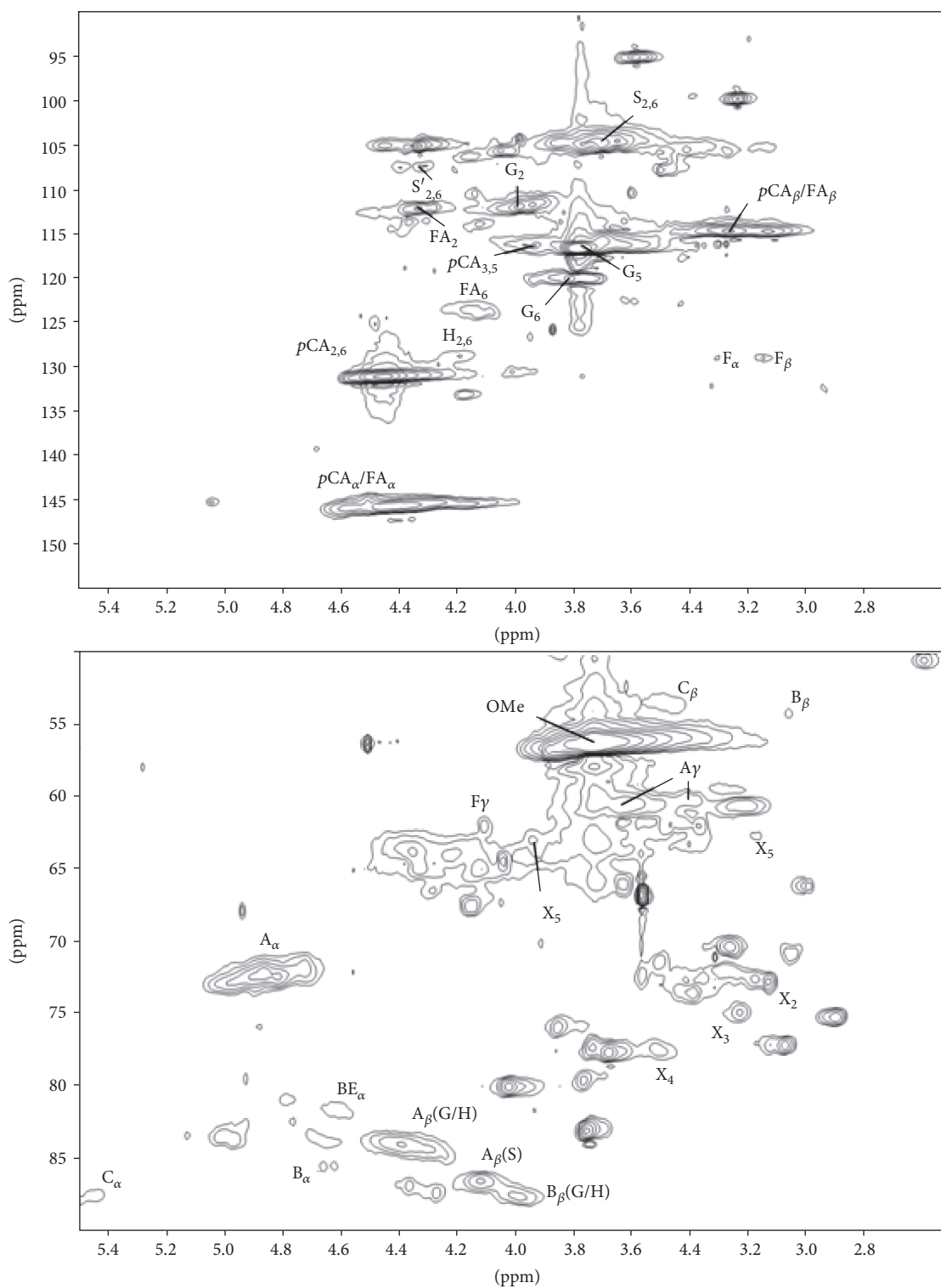
FIGURE 7

preserve the initial structure of lignin and obtain as much sample to be analyzed. Among the wet-chemistry techniques used, IL extraction and organosolv process are the promising methods. They are treated as environmentally friendly methods since relatively mild conditions used and the reagents can be recycled. Biological degradation might be another possible pathway for the oriented isolation of lignin since the outstanding selectivity and rate of conversion.

Various spectroscopic methods are routinely used for the investigation of lignin structures. These methods can provide both qualitative and quantitative information on functional groups and linkages in lignin as well as degradation products

of lignin. Among these spectroscopic techniques, UV spectroscopy is less likely to be used since it can provide relatively less information on the structural features of lignin. Generally, FTIR spectroscopy is much more frequently used than Raman spectroscopy. FTIR, ^{1}H NMR, and ^{13}C NMR are commonly used in most of the investigations for the characterization of structure of lignins. Recently, ^{31}P NMR is more adopted in this area. Significant progresses for structural elucidation of lignin rely on the application of quantitative ^{13}C NMR and various 2D NMRs. They are robust techniques by providing detailed qualitative and quantitative results with high resolution and precision and can be treated as ideal methods. Rapid, accurate, and nondestructive spectroscopic techniques can be combined to overcome their individual intrinsic limitations for better elucidation of lignin structure. The data collected from these methods contributes to the understanding of LCBM structure and facilitates the design of effective processes to obtain lignin-based value-added chemicals.

Conflicts of Interest

The authors declare that there is no conflict of interest regarding the publication of this paper.

Acknowledgments

References

[1] J. S. Luterbacher, D. M. Alonso, and J. A. Dumesic, "Targeted chemical upgrading of lignocellulosic biomass to platform molecules," *Green Chemistry*, vol. 16, pp. 4816–4838, 2014.

[2] B. M. Upton and A. M. Kasko, "Strategies for the conversion of lignin to high-value polymeric materials: review and perspective," *Chemical Reviews*, vol. 116, no. 4, pp. 2275–2306, 2016.

[3] K. M. N. Satheesh, A. K. Mohanty, L. Erickson, and M. Misra, "Lignin and its applications with polymers," *Journal of Biobased Materials and Bioenergy*, vol. 3, pp. 1–24, 2009.

[4] D. Stewart, "Lignin as a base material for materials applications: chemistry, applications and economics," *Industrial Crops and Products*, vol. 27, no. 2, pp. 202–207, 2008.

[5] C. R. Poovaiah, M. Nageswara-Rao, J. R. Soneji, H. L. Baxter, and C. N. Stewart Jr, "Altered lignin biosynthesis using biotechnology to improve lignocellulosic biofuel feedstocks," *Plant Biotechnology Journal*, vol. 12, pp. 1163–1173, 2014.

[6] H. B. C. Molinari, T. K. Pellny, J. Freeman, P. R. Shewry, and R. A. C. Mitchell, "Grass cell wall feruloylation: distribution of bound ferulate and candidate gene expression in *Brachypodium distachyon*," *Frontiers in Plant Science*, vol. 4, p. 50, 2013.

[7] J. Shigeto, Y. Ueda, S. Sasaki, K. Fujita, and Y. Tsutsumi, "Enzymatic activities for lignin monomer intermediates highlight the biosynthetic pathway of syringyl monomers in *Robinia pseudoacacia*," *Journal of Plant Research*, vol. 130, no. 1, pp. 203–210, 2017.

[8] A. L. Healey, J. S. Lupoi, D. J. Lee et al., "Effect of aging on lignin content, composition and enzymatic saccharification in *Corymbia* hybrids and parental taxa between years 9 and 12," *Biomass and Bioenergy*, vol. 93, pp. 50–59, 2016.

[9] D. Kai, M. J. Tan, P. L. Chee, Y. K. Chua, Y. L. Yap, and X. J. Loh, "Towards lignin-based functional materials in a sustainable world," *Green Chemistry*, vol. 18, no. 5, pp. 1175–1200, 2016.

[10] Y. Zeng, M. E. Himmel, and S. Y. Ding, "Coherent Raman microscopy analysis of plant cell walls," *Methods in Molecular Biology*, vol. 908, pp. 49–60, 2012.

[11] C. Zhou, Q. Li, V. L. Chiang, L. A. Lucia, and D. P. Griffis, "Chemical and spatial differentiation of syringyl and guaiacyl lignins in poplar wood via time-of-flight secondary ion mass apectrometry," *Analytical Chemistry*, vol. 83, no. 18, pp. 7020–7026, 2011.

[12] S. Jung, M. Foston, U. C. Kalluri, G. A. Tuskan, and A. J. Ragauskas, "3D chemical image using TOF-SIMS revealing the biopolymer component spatial and lateral distributions in biomass," *Angewandte Chemie International Edition*, vol. 51, no. 48, pp. 12005–12008, 2012.

[13] A. J. Ragauskas, G. T. Beckham, M. J. Biddy et al., "Lignin valorization: improving lignin processing in the biorefinery," *Science*, vol. 344, no. 6185, article 1246843, 2014.

[14] A. P. Dodd, J. F. Kadla, and S. K. Straus, "Characterization of fractions obtained from two industrial softwood kraft lignins," *ACS Sustainable Chemistry & Engineering*, vol. 3, no. 1, pp. 103–110, 2015.

[15] N. Giummarella, L. M. Zhang, G. Henriksson, and M. Lawoko, "Structural features of mildly fractionated lignin carbohydrate complexes (LCC) from spruce," *RSC Advances*, vol. 6, no. 48, pp. 42120–42131, 2016.

[16] H. L. Wang, H. X. Ben, H. Ruan et al., "Effects of lignin structure on hydrodeoxygenation reactivity of pine wood lignin to valuable chemicals," *ACS Sustainable Chemistry & Engineering*, vol. 5, no. 2, pp. 1824–1830, 2017.

[17] A. Berlin and M. Balakshin, "Industrial lignins: analysis, properties, and applications," in *Bioenergy Research: Advances and Applications*, V. K. Gupta, M. G. T. P. Kubicek and J. S. Xu, Eds., pp. 315–336, Elsevier, Amsterdam, 2014.

[18] R. Prado, A. Brandt, X. Erdocia, J. Hallet, T. Welton, and J. Labidi, "Lignin oxidation and depolymerisation in ionic liquids," *Green Chemistry*, vol. 18, no. 3, pp. 834–841, 2016.

[19] J. Shi, S. Pattathil, R. Parthasarathi et al., "Impact of engineered lignin composition on biomass recalcitrance and ionic liquid pretreatment efficiency," *Green Chemistry*, vol. 18, no. 18, pp. 4884–4895, 2016.

[20] Y. Lu, X. Y. Wei, J. P. Cao et al., "Characterization of a bio-oil from pyrolysis of rice husk by detailed compositional analysis and structural investigation of lignin," *Bioresource Technology*, vol. 116, pp. 114–119, 2012.

[21] S. Z. Wang, X. Fan, A. L. Zheng et al., "Evaluation of the oxidation of rice husks with sodium hypochlorite using gas chromatography-mass spectrometry and direct analysis in real time-mass spectrometry," *Analytical Letters*, vol. 47, no. 1, pp. 77–90, 2014.

[22] X. Fan, J. L. Zhu, A. L. Zheng et al., "Rapid characterization of heteroatomic molecules in a bio-oil from pyrolysis of rice husk using atmospheric solid analysis probe mass spectrometry," *Journal of Analytical and Applied Pyrolysis*, vol. 115, pp. 16–23, 2015.

[23] V. V. Lobodin, L. Nyadong, B. M. Ruddy et al., "Fourier transform ion cyclotron resonance mass spectrometry for analysis of complex organic mixtures," *International Journal of Mass Spectrometry*, vol. 378, pp. 186–192, 2015.

[24] C. F. Wang, X. Fan, F. Zhang et al., "Characterization of humic acids extracted from a lignite and interpretation for the mass spectra," *RSC Advances*, vol. 7, no. 33, pp. 20677–20684, 2017.

[25] T. T. You and F. Xu, "Applications of molecular spectroscopic methods to the elucidation of lignin structure," *Applications of Molecular Spectroscopy to Current Research in the Chemical and Biological Sciences*, vol. 2016, pp. 235–260.

[26] E. A. Capanema, M. Y. Balakshin, and J. F. Kadla, "A comprehensive approach for quantitative lignin characterization by NMR spectroscopy," *Journal of Agricultural and Food Chemistry*, vol. 52, no. 7, pp. 1850–1860, 2004.

[27] B. Jiang, T. Y. Cao, F. Gu, W. J. Wu, and Y. C. Jin, "Comparison of the structural characteristics of cellulolytic enzyme lignin preparations isolated from wheat straw stem and leaf," *ACS Sustainable Chemistry & Engineering*, vol. 5, no. 1, pp. 342–349, 2017.

[28] C. Zhao, S. Xie, Y. Pu et al., "Synergistic enzymatic and microbial conversion of lignin for lipid," *Green Chemistry*, vol. 18, no. 5, pp. 1306–1312, 2016.

[29] B. Ahvazi, É. Cloutier, O. Wojciechowicz, and T. D. Ngo, "Lignin profiling: a guide for selecting appropriate lignins as precursors in biomaterials development," *ACS Sustainable Chemistry & Engineering*, vol. 4, no. 10, pp. 5090–5105, 2016.

[30] M. Yáñez-S, B. Matsuhiro, C. Nuñez et al., "Physicochemical characterization of ethanol organosolv lignin (EOL) from *Eucalyptus globulus*: effect of extraction conditions on the molecular structure," *Polymer Degradation and Stability*, vol. 110, pp. 184–194, 2014.

[31] Q. Wang, S. S. Liu, G. L. Yang, and J. C. Chen, "Characterization of high-boiling-solvent lignin from hot-water extracted bagasse," *Energy & Fuels*, vol. 28, no. 5, pp. 3167–3171, 2014.

[32] M. B. Whitfield, M. S. Chinn, and M. W. Veal, "Improvement of acid hydrolysis procedures for the composition analysis of herbaceous biomass," *Energy & Fuels*, vol. 30, no. 10, pp. 8260–8269, 2016.

[33] W. H. Gong, Z. Y. Xiang, F. Y. Ye, and G. H. Zhao, "Composition and structure of an antioxidant acetic acid lignin isolated from shoot shell of bamboo (*Dendrocalamus latiforus*)," *Industrial Crops and Products*, vol. 91, pp. 340–349, 2016.

[34] W. Zhang, N. Sathitsuksanoh, B. A. Simmons, C. E. Frazier, J. R. Barone, and S. Renneckar, "Revealing the thermal sensitivity of lignin during glycerol thermal processing through structural analysis," *RSC Advances*, vol. 6, no. 36, pp. 30234–30246, 2016.

[35] A. E. Harman-Ware, C. Foster, R. M. Happs et al., "A Thioacidolysis method tailored for higher-throughput quantitative analysis of lignin monomers," *Journal of Biotechnology*, vol. 11, no. 10, pp. 1268–1273, 2016.

[36] J. L. Wen, S. L. Sun, B. L. Xue, and R. C. Sun, "Quantitative structures and thermal properties of birch lignins after ionic liquid pretreatment," *Journal of Agricultural and Food Chemistry*, vol. 61, no. 3, pp. 635–645, 2013.

[37] B. J. Cox and J. G. Ekerdt, "Pretreatment of yellow pine in an acidic ionic liquid: extraction of hemicelluloses and lignin to facilitate enzymatic digestion," *Bioresource Technology*, vol. 134, pp. 59–65, 2013.

[38] A. Casas, M. Oliet, M. V. Alonso, and F. Rodrígues, "Dissolution of *Pinus radiata* and *Eucalyptus globulus* woods in ionic liquids under microwave radiation: lignin regeneration and characterization," *Separation and Purification Technology*, vol. 97, pp. 115–122, 2012.

[39] S. S. Mohtar, T. N. Z. Tengku Malim Busu, A. M. Md Noor, N. Shaari, and H. Mat, "An ionic liquid treatment and fractionation of cellulose, hemicelluloses and lignin from oil palm empty fruit bunch," *Carbohydrate Polymers*, vol. 166, pp. 291–299, 2017.

[40] T. Rashid, C. F. Kait, I. Regupathi, and T. Murugesan, "Dissolution of kraft lignin using protic ionic liquids and characterization," *Industrial Crops and Products*, vol. 84, pp. 284–293, 2016.

[41] Y. X. An, N. Li, H. Wu, W. Y. Lou, and M. H. Zong, "Changes in the structure and the thermal properties of kraft lignin during its dissolution in cholinium ionic liquids," *ACS Sustainable Chemistry & Engineering*, vol. 3, no. 11, pp. 2951–2958, 2015.

[42] S. Nanayakkara, A. F. Patti, and K. Saito, "Lignin depolymerization with phenol via redistribution mechanism in ionic liquids," *ACS Sustainable Chemistry & Engineering*, vol. 2, no. 9, pp. 2159–2164, 2014.

[43] J. X. Long, W. Y. Lou, L. F. Wang, B. L. Yin, and X. H. Li, "[$C_4H_8SO_3Hmim$]HSO_4 as an efficient catalyst for direct liquefaction of bagasse lignin: decomposition properties of the inner structural units," *Chemical Engineering Science*, vol. 122, pp. 24–33, 2015.

[44] S. G. Khokarale, T. Le-That, and J. P. Mikkola, "Carbohydrate free lignin: a dissolution-recovery cycle of sodium lignosulfonate in a switchable ionic liquid system," *ACS Sustainable Chemistry & Engineering*, vol. 4, no. 12, pp. 7032–7040, 2016.

[45] A. Mittal, R. Katahira, B. S. Donohoe et al., "Ammonia pretreatment of corn stover enables facile lignin extraction," *ACS Sustainable Chemistry & Engineering*, vol. 5, no. 3, pp. 2544–2561, 2017.

[46] T. Q. Yuan, T. T. You, W. Wang, F. Xu, and R. C. Sun, "Synergistic benefits of ionic liquid and alkaline pretreatments of poplar wood. Part 2: characterization of lignin and hemicelluloses," *Bioresource Technology*, vol. 136, pp. 345–350, 2013.

[47] Y. C. Sun, M. Wang, and R. C. Sun, "Toward an understanding of inhomogeneities in structure of lignin in green solvents biorefinery. Part 1: fractionation and characterization of cignin," *ACS Sustainable Chemistry & Engineering*, vol. 3, no. 10, pp. 2443–2451, 2015.

[48] C. Nitsos, R. Stoklosa, A. Karnaouri et al., "Isolation and characterization of organosolv and alkaline lignins from hardwood and softwood biomass," *ACS Sustainable Chemistry & Engineering*, vol. 4, no. 10, pp. 5181–5193, 2016.

[49] L. N. Yang, D. M. Wang, D. Zhou, Y. W. Zhang, and T. T. Yang, "Isolation and further structural characterization of lignins from the valonea of *Quercus variabilis*," *International Journal of Biological Macromolecules*, vol. 97, pp. 164–172, 2017.

[50] L. N. Yang, D. M. Wang, D. Zhou, and Y. Zhang, "Effect of different isolation methods on structure and properties of lignin from valonea of *Quercus variabilis*," *International Journal of Biological Macromolecules*, vol. 85, pp. 417–424, 2016.

[51] S. Zhou, Y. Xue, A. Sharma, and X. L. Bai, "Lignin valorization through thermochemical conversion: comparison of hardwood, softwood and herbaceous lignin," *ACS*

Sustainable Chemistry & Engineering, vol. 4, no. 12, pp. 6608–6617, 2016.

[52] G. T. Beckham, C. W. Johnson, E. M. Karp, D. Salvachúa, and D. R. Vardon, "Opportunities and challenges in biological lignin valorization," *Current Opinion in Biotechnology*, vol. 42, pp. 40–53, 2016.

[53] F. Xu, R. C. Sun, M. Z. Zhai, J. X. Sun, J. X. Jiang, and G. J. Zhao, "Comparative study of three lignin fractions isolated from mild ball-milled *Tamarix austromogoliac* and *Caragana sepium*," *Journal of Applied Polymer Science*, vol. 8, no. 2, pp. 1158–1168, 2008.

[54] A. Sluiter, B. Hames, R. Ruiz et al., *Determination of Structural Carbohydrates and Lignin in Biomass*, National Renewable Energy Laboratory (NREL) Laboratory Analytical Procedures (LAP) for Standard Biomass Analysis, National Renewable Energy Laboratory, Golden, USA, 2007, NREL/TP-510-42618.

[55] F. Q. Xiong, Y. M. Han, S. Q. Wang et al., "Preparation and formation mechanism of renewable lignin hollow nanospheres with a single hole by self-assembly," *ACS Sustainable Chemistry & Engineering*, vol. 5, no. 3, pp. 2273–2281, 2017.

[56] B. Hansen, P. Kusch, M. Schulze, and B. Kamm, "Qualitative and quantitative analysis of lignin producedfrom beech wood by different conditions of the organosolv process," *Journal of Polymers and the Environment*, vol. 24, no. 2, pp. 85–97, 2016.

[57] S. O. Prozil, D. V. Evtuguin, A. M. S. Silva, and L. P. C. Lopes, "Structural characterization of lignin from grape stalks (*Vitis vinifera* L.)," *Journal of Agricultural and Food Chemistry*, vol. 62, no. 24, pp. 5420–5428, 2014.

[58] M. Azadfar, H. M. GaoA, M. V. Bule, and S. L. Chen, "Structural characterization of lignin: a potential source ofantioxidants *guaiacol* and *4-vinylguaiacol*," *International Journal of Biological Macromolecules*, vol. 75, pp. 58–66, 2015.

[59] K. A. Y. Koivu, H. Sadeghifar, P. A. Nousiainen, D. S. Argyropoulos, and J. Sipilä, "Effect of fatty acid esterification on the thermal properties of softwood kraft lignin," *ACS Sustainable Chemistry & Engineering*, vol. 4, no. 10, pp. 5238–5247, 2016.

[60] Q. L. Yang, J. B. Shi, and L. Lin, "Characterization of structural changes of lignin in the process of cooking of bagasse with solid alkali and active oxygen as a pretreatment for lignin conversion," *Energy & Fuels*, vol. 26, pp. 6999–7004, 2012.

[61] I. Santoni, E. Callone, A. Sandak, J. Sandak, and S. Dirè, "Solid state NMR and IR characterization of wood polymer structure in relation to tree provenance," *Carbohydrate Polymers*, vol. 117, pp. 710–721, 2015.

[62] L. Passauer, K. Salzwedel, M. Struch, N. Herold, and J. Appelt, "Quantitative analysis of the etherification degree of phenolic hydroxyl groups in oxyethylated lignins: correlation of selective aminolysis with FTIR spectroscopy," *ACS Sustainable Chemistry & Engineering*, vol. 4, no. 12, pp. 6629–6637, 2016.

[63] U. P. Agarwal, R. S. Reiner, A. K. Pandey, S. A. Ralph, K. C. Hirth, and R. H. Atalla, Eds., "Raman spectra of lignin model compounds," in *59th Appita Annual Conference and Exhibition: Incorporating the 13th ISWFPC (International Symposium on Wood, Fiber and Pulping Chemistry), Auckland, New Zealand, 16–19 May 2005: Proceedings*, Appita Inc., 2005.

[64] K. L. Larsen and S. Barsberg, "Environmental effects on the lignin model monomer, vanillyl alcohol, studied by Raman spectroscopy," *Journal of Physical Chemistry B*, vol. 115, no. 39, pp. 11470–11480, 2011.

[65] B. I. Na, S. J. Chang, K. H. Lee, G. Lee, and J. W. Lee, "Characterization of cell wall structure in dilute acid-pretreated biomass by confocal Raman microscopy and enzymatic hydrolysis," *Biomass and Bioenergy*, vol. 93, pp. 33–37, 2016.

[66] J. Ralph, C. Lapierre, F. C. Lu et al., "NMR evidence for benzodioxane structures resulting from incorporation of 5-hydroxyconiferyl alcohol into lignins of O-methyltransferase-deficient poplars," *Journal of Agricultural and Food Chemistry*, vol. 49, no. 7, pp. 86–91, 2001.

[67] L. M. Zhang, G. Gellerstedt, J. Ralph, and L. F. C. , "NMR studies on the occurrence of spirodienone structures in lignins," *Journal of Wood Chemistry and Technology*, vol. 26, no. 1, pp. 65–79, 2006.

[68] G. Wang and H. Chen, "Fractionation and characterization of lignin from steam-exploded corn stalk by sequential dissolution in ethanol-water solvent," *Separation and Purification Technology*, vol. 120, pp. 402–409, 2013.

[69] C. Fernández-Costas, S. Gouveia, M. A. Sanromán, and D. Moldes, "Structural characterization of kraft lignins from different spent cooking liquors by 1D and 2D nuclear magnetic resonance spectroscopy," *Biomass and Bioenergy*, vol. 63, pp. 156–166, 2014.

[70] L. L. An, G. H. Wang, H. Y. Jia, C. Y. Liu, W. J. Sui, and C. L. Si, "Fractionation of enzymatic hydrolysis lignin by sequential extraction for enhancing antioxidant performance," *International Journal of Biological Macromolecules*, vol. 99, pp. 674–681, 2017.

[71] C. A. Esteves Costa, W. Coleman, M. Dube, A. E. Rodrigues, and P. C. Rodrigues Pinto, "Assessment of key features of lignin from lignocellulosic crops: stalks and roots of corn, cotton, sugarcane, and tobacco," *Industrial Crops and Products*, vol. 92, pp. 136–148, 2016.

[72] H. Ben and A. J. Ragauskas, "Torrefaction of loblolly pine," *Green Chemistry*, vol. 14, no. 1, pp. 72–76, 2012.

[73] T. Wang, P. Phyo, and M. Hong, "Multidimensional solid-state NMR spectroscopy of plant cell walls," *Solid State Nuclear Magnetic Resonance*, vol. 78, pp. 56–63, 2016.

[74] D. Lee, S. Hediger, and G. De Paepe, "Is solid-state NMR enhanced by dynamic nuclear polarization?," *Solid State Nuclear Magnetic Resonance*, vol. 66-67, pp. 6–20, 2015.

[75] G. Mollica, M. Dekhil, F. Ziarelli, P. Thureau, and S. Viel, "Quantitative structural constraints for organic powders at natural isotopic abundance using dynamic nuclear polarization solid-state NMR spectroscopy," *Angewandte Chemie International Edition*, vol. 54, no. 20, pp. 6028–6031, 2015.

[76] F. A. Perras, H. Luo, X. M. Zhang, N. S. Mosier, M. Pruski, and M. M. Abu-Omar, "Atomic-level structure characterization of biomass pre- and post-lignin treatment by dynamic nuclear polarization-enhanced solid-state NMR," *Journal of Physical Chemistry A*, vol. 121, no. 3, pp. 623–630, 2017.

[77] X. Gao, D. D. Laskar, J. J. Zeng, G. L. Helms, and S. L. Chen, "A ^{13}C CP/MAS-based nondegradative method for lignin content analysis," *ACS Sustainable Chemistry & Engineering*, vol. 3, no. 1, pp. 153–162, 2015.

[78] S. Constant, C. S. Lancefield, B. M. Weckhuysen, and P. C. Bruijnincx, "Quantification and classification of carbonyls in industrial humins and lignins by ^{19}F NMR," *ACS Sustainable Chemistry & Engineering*, vol. 5, no. 1, pp. 965–972, 2017.

[79] Y. Pu, S. Cao, and A. J. Ragauskas, "Application of quantitative ^{31}P NMR in biomass lignin and biofuel precursors

characterization," *Energy & Environmental Science*, vol. 4, no. 9, pp. 3154–3166, 2011.

[80] S. D. Springer, J. He, M. Chui, R. D. Little, M. Foston, and A. Butler, "Peroxidative oxidation of lignin and a lignin model compound by a manganese SALEN derivative," *ACS Sustainable Chemistry & Engineering*, vol. 4, no. 6, pp. 3212–3219, 2016.

[81] L. Mbotchak, C. L. Morvan, K. L. Duong, B. Roussear, M. Tessier, and A. Fradet, "Purification, structural characterization, and modification of organosolv wheat straw lignin," *Journal of Agricultural and Food Chemistry*, vol. 63, no. 21, pp. 5178–5188, 2015.

[82] S. X. Xie, Q. N. Sun, Y. Q. Pu et al., "Advanced chemical design for efficient lignin bioconversion," *ACS Sustainable Chemistry & Engineering*, vol. 5, no. 3, pp. 2215–2223, 2017.

[83] F. C. Lu and J. Ralph, "Non-degradative dissolution and acetylation of ball-milled plant cell walls: high-resolution solution-state NMR," *The Plant Journal*, vol. 35, no. 4, pp. 535–544, 2003.

[84] J. J. Bozell, C. J. O'Lenick, and S. Warwick, "Biomass fractionation for the biorefinery: heteronuclear multiple quantum coherence-nuclear magnetic resonance investigation of lignin isolated from solvent fractionation of switchgrass," *Journal of Agricultural and Food Chemistry*, vol. 59, no. 17, pp. 9232–9242, 2011.

[85] Y. Le Brech, L. Delmotte, J. Raya, N. Brosse, R. Gadiou, and A. Dufour, "High resolution solid state 2D NMR analysis of biomass and biochar," *Analytical Chemistry*, vol. 87, no. 2, pp. 843–847, 2015.

[86] Y. Le Brech, J. Raya, L. Delmotte, N. Brosse, R. Gadiou, and A. Dufour, "Characterization of biomass char formation investigated by advanced solid state NMR," *Carbon*, vol. 108, pp. 165–177, 2016.

[87] D. Ando, F. Nakatsubo, T. Takano, and H. Yano, "Elucidation of LCC bonding sites via γ-TTSA lignin degradation: crude milled wood lignin (MWL) from *Eucalyptus globulus* for enrichment of lignin xylan linkages and their HSQC-NMR characterization," *Holzforschung*, vol. 70, no. 6, pp. 489–494, 2016.

[88] D. Ando, F. Nakatsubo, and H. Yano, "Acetylation of ground pulp: monitoring acetylation via HSQC-NMR spectroscopy," *ACS Sustainable Chemistry & Engineering*, vol. 5, no. 2, pp. 1755–1762, 2017.

[89] K. Saito, A. Kaiho, R. Sakai, H. Nishimura, H. Okada, and T. Watanabe, "Characterization of the interunit bonds of lignin oligomers released by acid-catalyzed selective solvolysis of *Cryptomeria japonica* and *Eucalyptus globulus* woods via thioacidolysis and 2D-NMR," *Journal of Agricultural and Food Chemistry*, vol. 64, no. 48, pp. 9152–9160, 2016.

[90] J. Rencoret, P. Prinsen, A. Gutiérrez, Á. T. Martínez, and J. C. del Río, "Isolation and structural characterization of the milled wood lignin, dioxane lignin, and cellulolytic lignin preparations from brewer's spent grain," *Journal of Agricultural and Food Chemistry*, vol. 63, no. 2, pp. 603–613, 2015.

[91] C. Mattsson, S. I. Andersson, T. Belkheiri et al., "Using 2D NMR to characterize the structure of the low and high molecular weight fractions of bio-oil obtained from lignoBoost™ kraft lignin depolymerized in subcritical water," *Biomass and Bioenergy*, vol. 95, pp. 364–377, 2016.

[92] L. Zhang and G. Gellerstedt, "Quantitative 2D HSQC NMR determination of polymer structures by selecting suitable internal standard references," *Magnetic Resonance in Chemistry*, vol. 45, no. 1, pp. 37–45, 2007.

[93] J. J. Zeng, G. L. Helms, X. Gao, and S. L. Chen, "Quantification of wheat straw lignin structure by comprehensive NMR analysis," *Journal of Agricultural and Food Chemistry*, vol. 61, no. 46, pp. 10848–10857, 2013.

[94] K. Crouvisier-Urion, P. R. Bodart, P. Winckler et al., "Biobased composite films from chitosan and lignin: antioxidant activity related to structure and moisture," *ACS Sustainable Chemistry & Engineering*, vol. 4, no. 12, pp. 6371–6381, 2016.

Research Article

Microstructure of Coal Gangue and Precipitation of Heavy Metal Elements

Yanli Huang, Junmeng Li, Tianqi Song, Qiang Sun, Guoqiang Kong, and Fengwan Wang

School of Mines, State Key Laboratory of Coal Resources and Safe Mining, China University of Mining & Technology, Xuzhou 221116, China

Correspondence should be addressed to Junmeng Li; lijunmeng1201@163.com

The microstructure and mineral composition of the gangue play a decisive role in the precipitation of heavy metal elements. In this study, the microstructure, mineral composition, and precipitation of heavy metal elements of coal gangue with different weathering degrees were analyzed through electron microscopy, X-ray diffraction, and static immersion leaching experiments. The following results were derived. (1) After the weathering of the coal gangue, its compactness and integrity changed significantly. The coal gangue structure transformed from relatively dense to relatively loose, and the development of large pores and fractures changed from basically no development to significant development. (2) After weathering, the contents of kaolinite and illite significantly increased, while that of feldspar significantly decreased. Coal gangue contains a small amount of Mn, Cu, Zn, Ti, Ba, Cl, and other elements. After weathering, the contents of each element were reduced. (3) Under the same conditions, a higher number of heavy metal elements precipitated from the weathered coal gangue than from the fresh coal gangue. The results of this research have significant importance in revealing the precipitation mechanism of heavy metals from coal gangue and in perfecting the theory of underground water environmental protection during solid backfilling mining.

1. Introduction

In addition to containing a large number of major elements including C, Si, Al, Fe, Ca, and Mg, coal gangue also contains a variety of trace heavy metal elements. Under long-term weathering and rain leaching, these heavy metal elements cause pollution in the groundwater, surface water, and soil. In the fully mechanized solid backfilling coal mining, the bottom-well environment is relatively closed, dark, and humid, while the ground stress and terrestrial heat are high. In addition, the overlying cap rock fracture development and coal mining process will result in mine water emission; thus, the coal gangue fillings in the goaf are consequently always immersed in a water environment [1–3]. After long-term mine-water leaching and soaking, the heavy metal elements and inorganic salts in this part of the coal gangue will be released after dissolving in water. Under certain conditions, these elements will migrate in the goaf and floor areas with the flow of mine water and may penetrate into the underlying aquifers, causing a potentially significant

impact on the groundwater environment. Some of the coal gangue used in solid backfilling coal mining is fresh, that is, just out of the well or obtained directly from sorting at the downhole; however, some is weathered gangue obtained from the ground gangue hill after long-time weathering [4, 5]. The microstructures and mineral compositions of fresh and weathered coal gangue are different and play a decisive role in the precipitation of heavy metal elements. Therefore, it is important to study these two features at different weathering degrees to reveal the precipitation mechanism of heavy metal elements in coal gangue and to improve the theory of groundwater environmental protection for solid backfilling in coal mining.

In recent years, domestic and foreign scholars have conducted a series of useful fundamental research on the microstructure of coal gangue, its mineral components, and precipitation mechanism of heavy metal elements in coal gangue. Wu [6] analyzed the microstructure of different solid backfilling materials through scanning electron microscopy (SEM) and then studied the internal mechanism
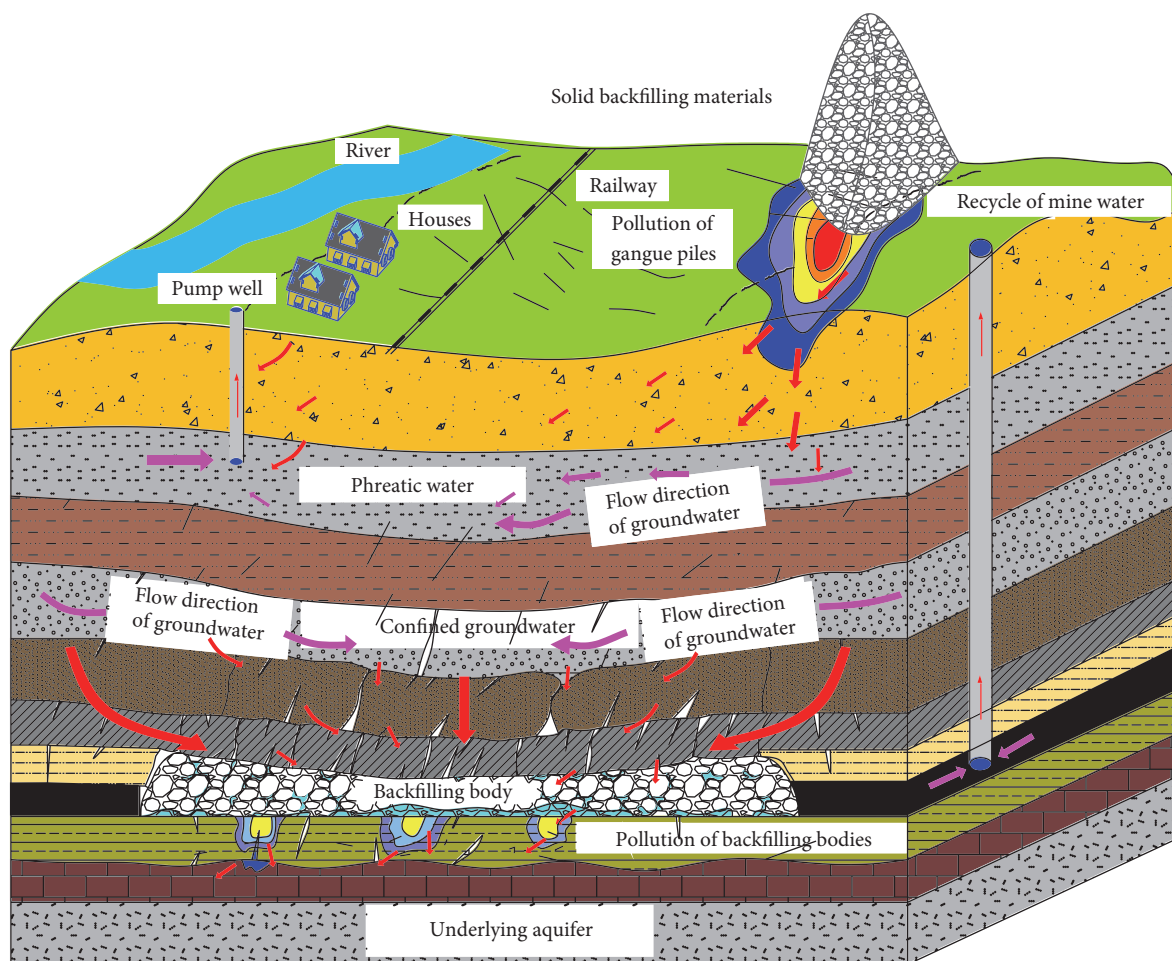
Figure 1: Schematic of groundwater pollution from coal gangue backfilling in goaf.

of compaction deformation. Li and Wu [7] performed X-ray diffraction (XRD) analysis on clay minerals and found that the chemical weathering in this area was obvious, and significant development of clay minerals was observed in the weathered rock. Shang et al. [8] analyzed the mineral composition of weathered granite through XRD. Li [9] performed a 40-day static immersion leaching test on coal gangue with different weathering degrees in the Huangling number 1 mine in northern Shaanxi. He measured the concentration and pH of seven types of trace elements including Cu, Zn, Cr, and Pb in the leaching solution. Li et al. [10] performed dynamic leaching tests on four types of coal gangue with different particle sizes in the Pingdingshan number 12 mine, Henan Province, and monitored the concentration of heavy metal elements Zn, Mn, and Cd in the leaching solution. Their results showed that the content of heavy metal elements in the leaching solution is inversely proportional to the coal gangue particle size. However, no research has been conducted on the precipitation of heavy metal ions of coal gangue by considering different weathering degrees under leaching conditions. In this paper, electron microscopy, XRD, and static immersion leaching experiments were performed to reveal the precipitation mechanism of heavy metal elements of coal gangue with different

weathering degrees under leaching conditions from two aspects: microstructure and mineral composition of the coal gangue.

2. Influence of Coal Gangue Backfilling on the Groundwater Environment

The coal goaf area is a long-term relatively closed, dark, and humid environment. Influenced by the mining depth, geothermal and mine water, and other effects, this area is a relatively closed environment of high stress, where temperature is generally higher than the normal temperature (i.e., the temperature of a part of the goaf area affected by geothermal heat can reach 303.15 K~313.15 K or above). In addition, water can seep out because of the development of fractures in the overlaying cap rock; during the development of coal seam, the coal gangue filled into the goaf will always be immersed in a water environment. After long-term mine water leaching and soaking, the heavy metal elements and inorganic salts in this part of the coal gangue will be released after dissolving in water. Under certain conditions, these elements will migrate in the goaf and floor areas with the flow of mine water and may penetrate into the underlying aquifers,

Dense structure

(a) 80 times—general picture

No development of large pores or fractures

(b) 160 times—enlarged

No development of fine pores and fractures
in fine-grained clay and no visible layer distribution

(c) 600 times—enlarged

"Cement" structure between coarse
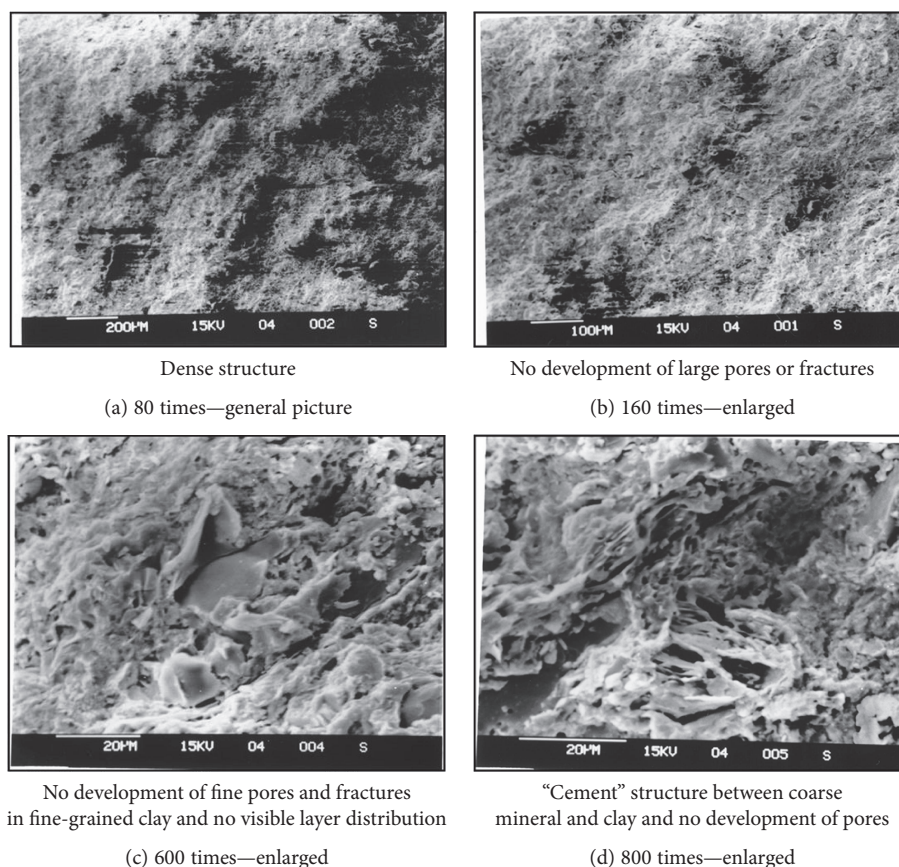mineral and clay and no development of pores

(d) 800 times—enlarged

FIGURE 2: SEM images of the fresh coal gangue at different resolutions.

causing a potentially significant impact on the groundwater environment, as shown in Figure 1.

3. Test Equipment and Material Selection

3.1. Main Test Equipment. The test was completed by scanning electron microscopy (SEM), X-ray diffractometer, and inductively coupled plasma (ICP) atomic emission spectroscopy. The current study analyzed the compactness of coal gangue with different weathering degrees by using an FEI Quanta™ 250 scanning electron microscope. This study qualitatively and quantitatively analyzed the mineral and chemical compositions of coal gangue with different weathering degrees through a D/Max-3B X-ray diffractometer [11, 12] (produced by Japan Rigaku Corporation). The incident light was Cu target Kα radiation ($\lambda = 1.5406$ Å), the X-ray tube operation voltage was 35 kV, the current was 30 mA, and the slit width was 1°. Inductively coupled plasma (ICP) atomic emission spectroscopy was used to determine the major, trace, and ultratrace element contents in various substances (which can be dissolved in hydrochloric acid, nitric acid, hydrofluoric acid, etc.). This instrument can be used for analyzing solid and liquid sample elements, such as rock soil, alloy materials, chemical raw materials, inorganic and organic products, water samples, foodstuffs, plants, animals, and oils.

3.2. Selection of Test Materials. In this study, the gangue to be filled in the Pingdingshan 12 coal mine was selected as the main research object. The gangue mined out from the well was used as the fresh coal gangue and that on the surface of the gangue hill was used as the weathered coal gangue. The "snake sampling method" was used to determine 20 sampling points, after mixing the samples of each sample point, sampling through the "cone quartering" method, and then repeating these steps once again.

4. Analysis of Gangue Compactness Based on SEM

The sample compactness was analyzed through SEM, and the SEM images of fresh and weathered coal gangue were obtained under different resolution conditions, as shown in Figures 2 and 3.

Figures 2 and 3 show that the structure of fresh coal gangue is relatively dense, the surface is uneven, and there are no development of large pores or fractures. In contrast, the structure of the gangue becomes relatively loose after weathering, it was uneven, and there was obvious development of large pores and fractures. After the weathering, the compactness and integrity of the gangue were observed to change significantly; this would have an important influence

Relative loose structure

(a) 80 times—general picture

Obvious development of large pores
and fractures

(b) 160 times—enlarged

Obvious development of
fine pores and fractures in fine-grained clay

(c) 250 times—enlarged

Concentrated partial crystallization,
obvious plate-like cementing structure,
completed crystalline part
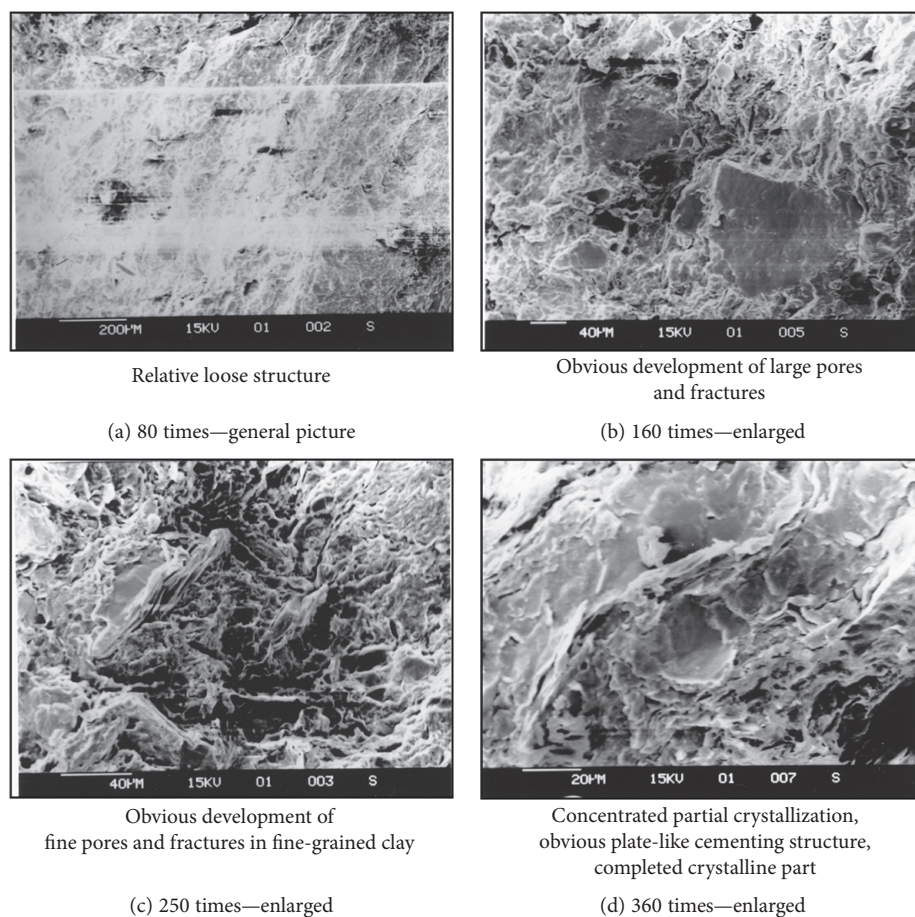
(d) 360 times—enlarged

FIGURE 3: SEM images of the weathered coal gangue at different resolutions.

on the precipitation of heavy metal elements under the leaching condition.

5. XRD Analysis of Heavy Metal Elements in the Gangue

5.1. Mineral Composition Characterization. The equipment used in this test is a D/Max-3B type X-ray diffractometer manufactured by Japan Rigaku Corporation. The test conditions were as follows: Cu target Kα radiation and graphite-bending crystal monochromator. The slit system comprised a 1° divergence slit (DS), a 1° receiving slit (RS), a 0.15 mm antiscattering slit (SS), and a 0.6° monochromator slit (RSM). Here, the X-ray tube voltage was 35 kV and the X-ray tube current was 30 mA. In the qualitative analysis process, the scanning mode was continuous with a scanning speed of 8°/min and a sampling interval of 0.02°. In the quantitative analysis process, the step scanning method was used with a scanning speed of 0.25°/min and sampling interval of 0.01°.

The qualitative analysis was conducted using a standard material powder diffraction file (PDF) provided by the International Center for Diffraction Data (JCPDS-ICDD) and was analyzed according to standard analytical methods. The analytical standards used in the quantitative analysis were in accordance with the *K*-value method in the Chinese standard (GB5225–86). The XRD patterns of the fresh and weathered coal gangue are shown in Figures 4 and 5, respectively, and the mineral composition of each sample is shown in Table 1.

The experimental results showed that the mineral compositions of fresh and weathered coal gangue were not significantly different, and the major components are quartz and kaolinite, between which the proportion of kaolinite was the largest, that is, 33% and 42%, respectively. The components also include illite, illite-montmorillonite mixed layer, and a small amount of chlorite, siderite, pyrite, and other minerals. The amorphous components may be coal or other substances based on the analysis. After weathering, the kaolinite and illite content in gangue increased significantly from 33% and 5% to 42% and 15%, respectively. In other words, the contents increased by 27.3% and 200%, respectively. The content of feldspar significantly decreased from the original 20% to 5%; the decline rate is 75%. The minerals generated through coal gangue weathering were observed to be mainly kaolinite and illite, which are obtained from feldspar decomposition.

5.2. Chemical Compositions. Table 2 shows the analysis results of the chemical composition of fresh and weathered coal gangue, respectively.

Table 2 shows that in the material composition of coal gangue, SiO_2 is the main component with high content, accounting for 59.9% and 53.7% of the fresh and weathered coal gangue, respectively. The secondary element is Al_2O_3,
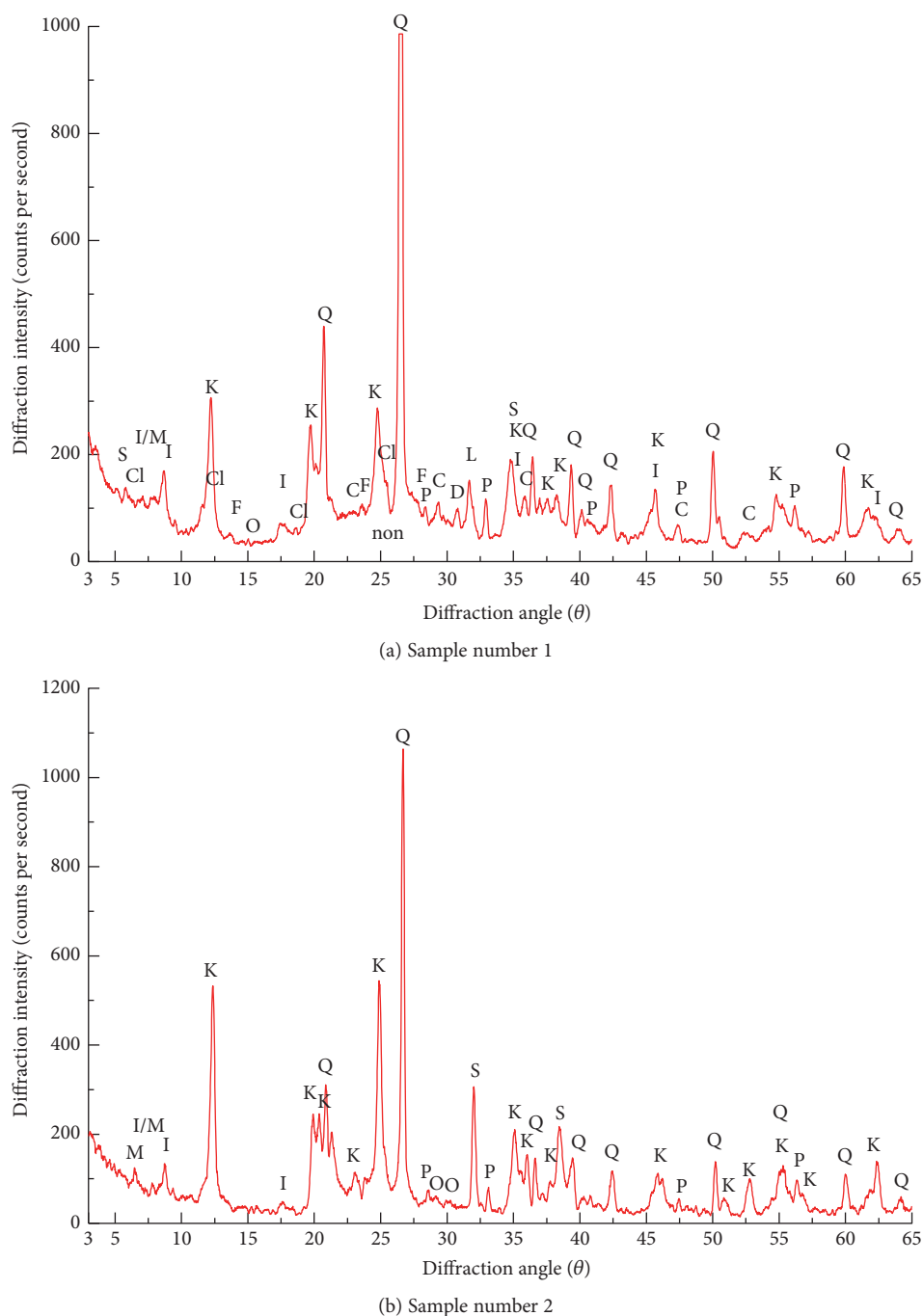
(a) Sample number 1

(b) Sample number 2

FIGURE 4: XRD patterns of the fresh coal gangue. (a) Q: quartz (high); K: kaolinite (high); I: illite; I/M: illite-montmorillonite mixed layer; Cl: Chlorite; S: Smectite; D: dolomite (low); P: pyrite; L: siderite; C: calcite (low); F: feldspar; non: amorphous materials; O: others (low). (b) K: kaolinite (high); Q: quartz (high); I: illite (high); I/M: illite-montmorillonite mixed layer; S: siderite; P: pyrite (low); O: others (low).

accounting for 20.7% and 17.6% of fresh and weathered coal gangue, respectively. The contents of SiO_2, Al_2O_3, and S in the weathered coal gangue are lower than those in the fresh coal gangue, and the content of P is slightly increased. The chemical elements also contain a small amount of Mn, Cu, Zn, Ti, Ba, and Cl. Among these elements, the content of Mn is the highest, that is, 0.054% and 0.043% in fresh and weathered gangue, respectively. The contents of each element in the coal gangue are reduced after weathering.

5.3. Screening of the Potential Water Pollution Component in Coal Gangue. The quality assessment criteria for water quality involve pollutant limits, which are a key indicator of whether coal gangue has an impact on the water quality. According to the status quo of groundwater quality in China, the standard of human health, and environmental protection target of groundwater quality and based on the highest water quality requirement of drinking, indus-trial, and agricultural water, the groundwater quality is
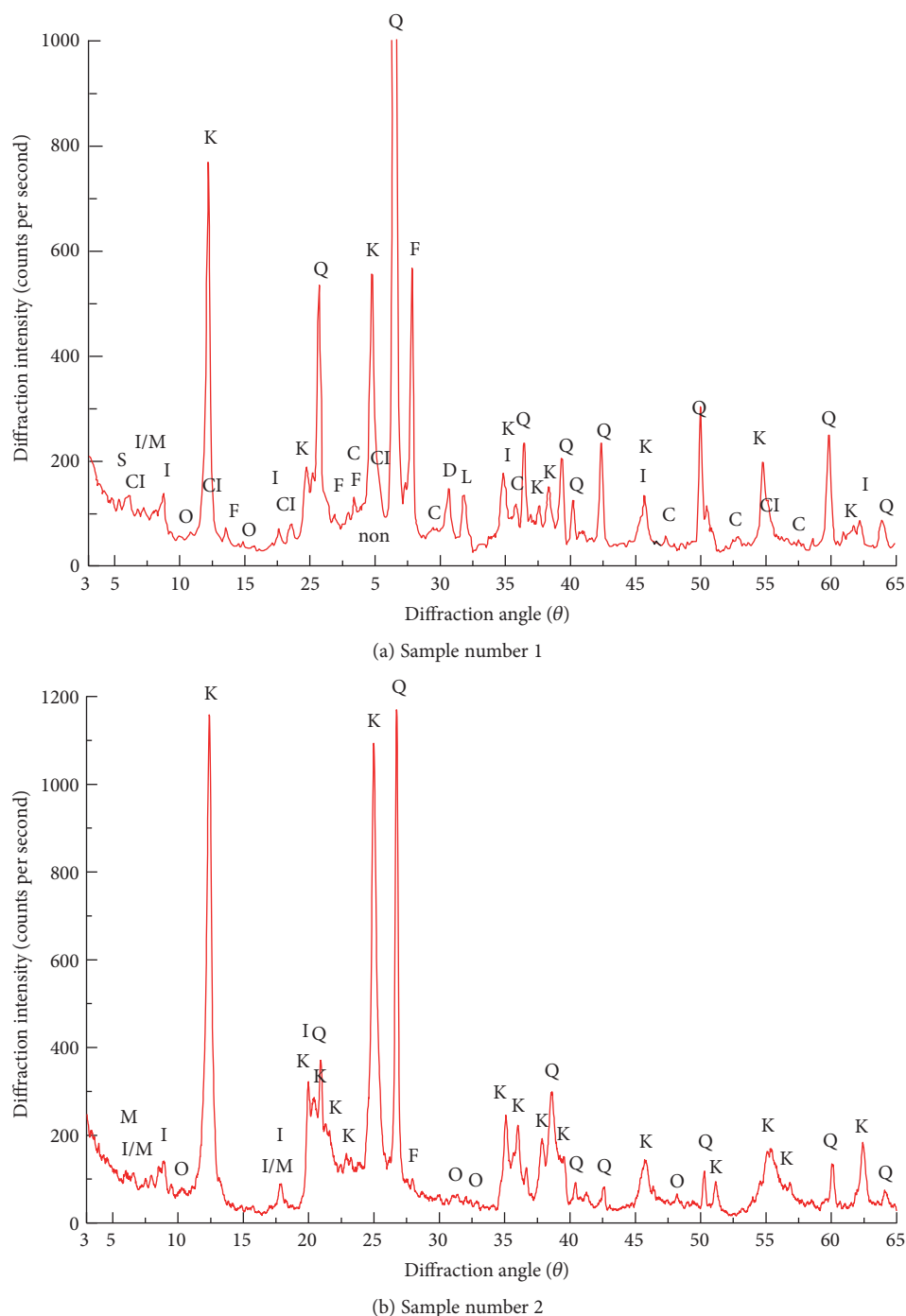
(a) Sample number 1

(b) Sample number 2

FIGURE 5: XRD analysis of the weathered coal gangue. (a) Q: quartz (high); K: kaolinite (high); F: feldspar; Cl: Chlorite; I: illite (high); I/M: illite-montmorillonite mixed layer; S: smectite (low); D: dolomite (low); L: siderite (low); C: calcite (low); non: amorphous materials; O: others (low). (b) K: kaolinite (high); Q: quartz (high); I: illite (high); I/M: illite-montmorillonite mixed layer; M: montmorillonite; F: feldspar (low); O: others (low).

divided into five categories. Class I mainly reflects the natural low background content of the chemical composition of groundwater. Class II mainly reflects the natural background content of the chemical composition of groundwater. Class III is based on the human health reference value, which is mainly applicable to the centralized drinking water source as well as to the agricultural and industrial water. Class IV class is based on agricultural and industrial water requirements but can further be used in drinking water after appropriate treatment. Class V is not suitable for drinking; other types of water applications can be selected according to the usage purpose. The supplementary material available online at https://doi.org/10.1155/2017/3128549 shows the classification index of the groundwater quality in China.

TABLE 1: Mineral composition of fresh and weathered coal gangue (%).

Sample	Quartz	Kaolinite	Illite	Illite-montmorillonite mixed layer	Smectite	Chlorite
Fresh coal gangue	20	33	5	8	2	2
Weathered coal gangue	21	42	15	6	2	3
	Feldspar	Dolomite	Calcite	Siderite	Pyrite	Coal
Fresh coal gangue	20	0.5	0.5	1.3	1.6	6
Weathered coal gangue	5	1	0.2	1	0	3.7

TABLE 2: Chemical composition of coal gangue (%).

Sample	Na_2O	MgO	Al_2O_3	SiO_2	K_2O	CaO	Fe_2O_3	P	S
Fresh coal gangue	0.65	1.8	20.7	59.9	2.4	2.0	6.7	0.05	1.53
Weathered coal gangue	0.41	1.4	17.6	53.7	2.0	1.3	5.4	0.06	0.44
	F	Ba	Mn	Cu	Pb	Zn	Ti	Cl	F
Fresh coal gangue	≤0.045	0.10	0.054	0.0006	<0.0002	0.009	0.50	0.011	≤0.045
Weathered coal gangue	<0.045	≤0.002	0.043	0.0005	<0.0002	0.005	0.42	0.009	<0.045

TABLE 3: Experimental design.

Sample	Weathering degrees	pH
Number 1		5
Number 2	Fresh coal gangue	7
Number 3		9
Number 4		5
Number 5	Weathered coal gangue	7
Number 6		9

FIGURE 6: Gangue with particle size 20–30 mm.

According to the current evaluation criteria of water environment quality and the test results of coal gangue composition, the main potential pollution components were determined as Fe, Mn, Cu, Zn, Pb, Cd, As, Be, Hg, Se, Ca, and Na.

6. Precipitation Mechanism of Heavy Metal Elements in Coal Gangue Backfilling

The coal gangue filled in the goaf is subject to mine water leaching and soaking or actions of other media. As a result, the heavy metals and inorganic salt components are dissolved in water and can be released from the coal gangue. In this study, the release mechanisms of the heavy metal elements in coal gangue with different weathering degrees were analyzed at different alkaline conditions by using a coal gangue soaking test method under indoor temperature. The concentration of heavy metal ions that precipitated from the coal gangue was used as the detection index, and the distilled water with the initial pH value of 7 was used as the basic solution.

6.1. Experimental Design of Static Immersion Leaching of Coal Gangue

6.1.1. Experimental Design. To study the precipitation and release characteristics of heavy metal elements Mn, Cu, Zn, Pb, and Cr in the coal gangue with different weathering degrees under different pH conditions, an orthogonal experiment was designed (Table 3). To ensure accuracy of the test data, each test was repeated three times.

6.1.2. Experimental Procedures. The particle size of gangue fillings used in solid backfilling coal mining is generally not more than 50 mm. To make the precipitation of the potential pollution components more intuitive, samples of single-particle-size-grade coal gangue were obtained from the Pingdingshan 12 mine for this experiment. The gangue freshly mined out of the Pingdingshan 12 mine was used as the fresh coal gangue, and the gangue from the waste gangue hill was used as the weathered coal gangue. First, the gangue was broken, and the gangue with a diameter of 20–30 mm was selected through a grading screen (see Figure 6), and then, the gangue was inserted into the incubator, dried for 24 h at 105°C, and finally placed in a jar and sealed to be used as the test sample.
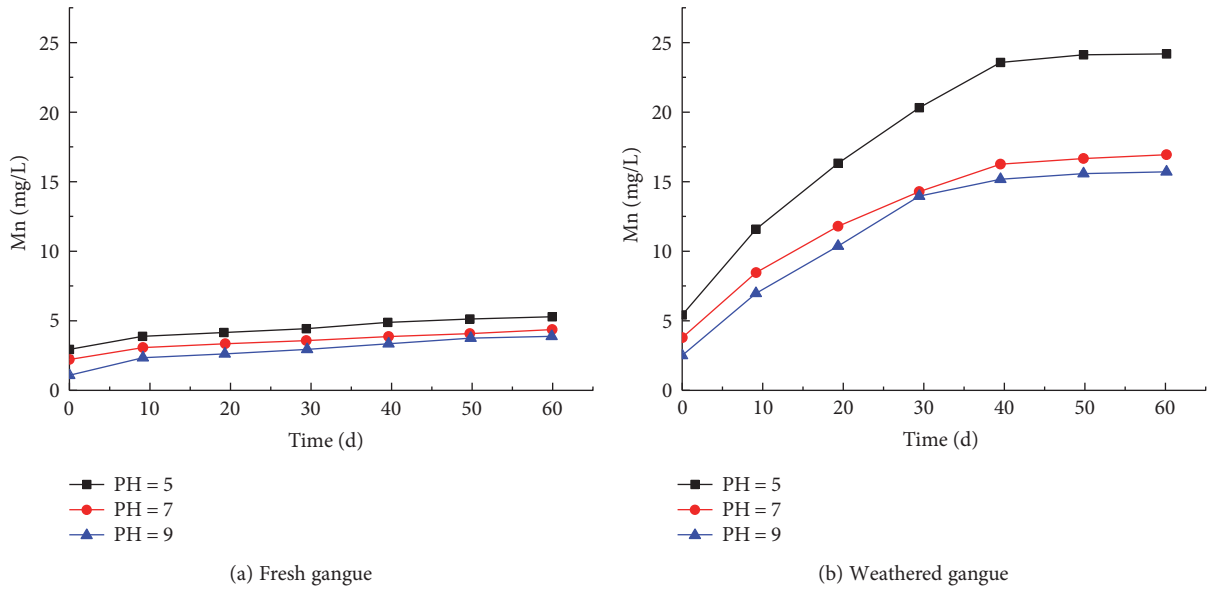
(a) Fresh gangue

(b) Weathered gangue

Figure 7: Mn element.

A certain amount of coal gangue samples was weighed and placed in a large-capacity plastic bucket. Leaching solutions with pH = 5, 7, and 9 were added. The solid–liquid volume ratios were maintained at 1 : 10 and remained unchanged. Aliquots were removed every 10 d for sampling. Next, the solution was stirred for 1 h before sampling, and then, the stirring was stopped. After settlement, a clear supernatant, which was the test solution, was obtained. The test solution was put into a bottle, sealed, and labeled. After the solutions were collected, the collected solution was detected using an ICP atomic emission spectrometer. After the detection, the residual waste liquid was collected for centralized processing treatment. Eighteen test solutions were collected for this test.

6.2. Analysis of Experimental Results of the Static Immersion Leaching of Coal Gangue. The precipitation of heavy metal elements in the coal gangue under different pH conditions shows similar trends. Owing to the limitation of space, this paper only analyzed the Mn element as an example; the results of which are shown in Figure 7.

The following observations are derived from Figure 7.

(1) The precipitation of heavy metal elements under different pH conditions shows similar trends. The precipitation process is divided into three stages: the presoaking, soaking, and end-of-the-soaking stages. The dissolution release rate in the early stage of immersion is very fast, mainly because of the development of pores, the ability of pores to pass through each other, the large specific surface area of pores; after the solution is immersed in the pores, it can be fully contacted with the gangue and easily flow, resulting in heavy metal elements of coal gangue with a faster dissolution and release rate; then, the dissolution release rate relatively slows in the middle of the

soaking process, mainly because coal gangue particles are dissolved or even broken by the interaction between coal gangue and immersion solution, so decreased pores hinder the flow of the solution with the immersion time and the decreased specific surface area between the solution and the pores result in a decreased dissolved release rate of heavy metal elements. And the dissolution release rate tends to be stable toward the end of the soaking. The concentration of heavy metal elements in the soaking solution gradually increases with the immersion time, while the precipitation rate gradually decreases.

(2) Under the same conditions, the heavy metal elements that precipitated from the weathered coal gangue were obviously higher than those that precipitated from the fresh coal gangue. When the pH value is 5, the concentration of Mn ion in the soaking solution was 5.686 mg/L for the fresh gangue after 60 d of leaching. In contrast, the concentration of Mn ion in the soaking solution is 25.138 mg/L for the weathered gangue after the same leaching period; this is 4.4 times that of the fresh coal gangue. This is mainly because of the relatively loose structure and significant development of coarse holes and fractures of coal gangue after weathering; this significantly increased the contact area of the gangue and the solution in the immersion process and promotes the precipitation of heavy metal ions in coal gangue.

(3) The degree of pollution risk to the groundwater environment when using the weathered coal gangue as a filling for the goaf area is obviously higher than that when using the fresh gangue. Thus, the gangue, which is as fresh as possible, should be selected during backfilling to reduce the impact on groundwater environment.

7. Conclusions

(1) The compactness and integrity of coal gangue change remarkably after weathering. The structure of the fresh coal gangue is relatively dense, and large pores and fractures are not developed. The structure of the weathered gangue is relatively loose, with obvious development of large pores and fractures.

(2) The mineral compositions of fresh and weathered coal gangue are not significantly different. In addition, the main components are quartz and kaolinite, along with some illite, illite-montmorillonite mixed layer, and a small amount of chlorite, siderite, pyrite, and so forth. The content of kaolinite and illite after coal gangue weathering was significantly increased, while the content of feldspar significantly decreased.

(3) In the composition of coal gangue, SiO_2 is the main component, followed by Al_2O_3. The content of SiO_2, Al_2O_3, and S in the weathered coal gangue was lower than that in the fresh coal gangue, while the content of P was slightly higher. Chemical elements contain a small amount of Mn, Cu, Zn, Ti, Ba, Cl, and other elements, among which the content of Mn is the highest. Moreover, the contents of each element in coal gangue reduced after weathering.

(4) Under the same conditions, the heavy metal elements precipitated from the weathered coal gangue are obviously higher than those precipitated from the fresh coal gangue. This is mainly because of the relatively loose structure and significant development of coarse holes and fractures of coal gangue after weathering, which significantly increases the contact area of gangue and the solution in the immersion process and promotes the precipitation of heavy metal ions in the coal gangue.

Conflicts of Interest

The authors declare that they have no conflicts of interest.

Acknowledgments

References

[1] J. Zhang, *Study on Strata Movement Controlling by Raw Waste Backfilling with Fully-Mechanized Coal Winning Technology and Its Engineering Applications*, China University of Mining and Technology, Xuzhou, 2008.

[2] J. Zhang, X. Miao, and G. Guo, "Development status of backfilling technology using raw waste in coal mining," *Journal of Mining & Safety Engineering*, vol. 26, no. 4, pp. 395–401, 2009.

[3] Y. Huang, *Ground Control Theory and Application of Solid Dense Backfill in Coal Mines*, China University of Mining and Technology, Xuzhou, 2012.

[4] H. Jiang, "Harmfulness of coal gangue to environment and its comprehensive treatment and utilization," *Coal Processing and Comprehensive Utilization*, vol. 03, pp. 43–46, 2003.

[5] J. Ye, G. Shen, and L. Lu, "Hazards and comprehensive utilization of coal gangue," *China Resources Comprehensive Utilization*, vol. 05, pp. 32–34, 2010.

[6] X.-G. Wu, *Mechanical Properties of Solid Filling Materials Research and Application*, China University of Mining and Technology, Xuzhou, 2014.

[7] R. Li and L. Wu, "Research on characteristic indexes of weathering intensity of rocks," *Chinese Journal of Rock Mechanics and Engineering*, vol. 22, pp. 3830–3833, 2004.

[8] Y. J. Shang, S. J. Wang, Z. Q. Yue, R. L. Hu, and X. B. Tu, "Variation features of pore radius and particle diameter distributions and mineral content of completely decomposed granite and correlation of parameters," *Rock and Soil Mechanics*, vol. 25, no. 10, pp. 1545–1550, 2004.

[9] X. Li, *Study on the Influence of Coal Gangue on Environment and Reuse*, Chang'an University, Xi'an, China, 2006.

[10] F. Li, J. Zheng, and Y. Deng, "Leaching experiments with gangue of different diameters simulating the environmental influence after filling-in coal mine," *Journal of Henan Polytechnic University*, vol. 25, no. 2, pp. 101–103, 2006.

[11] X. Fan, L. Chen, S. Wang et al., "Analysis of geting bituminous coal by electrospray ionization and direct analysis in real time mass spectrometry," *Analytical Letters*, vol. 47, no. 12, pp. 2012–2022, 2014.

[12] X. Fan, C. Wang, C. You et al., "Characterization of a Chinese lignite and the corresponding derivatives using direct analysis in real time quadrupole time-of-flight mass spectrometry," *RSC Advances*, vol. 6, no. 107, pp. 105780–105785, 2016.

Research Article

The Deterioration Mechanism of Diester Aero Lubricating Oil at High Temperature

Ting Yao,[1,2] Hongwei Yang,[3] Li Guo,[3] Yiwei Fei,[3] Huize Jiang,[3] Sen Bian,[3] and Tonghai Wu[2]

[1]*Analysis and Testing Center, Huangshan University, Huangshan, Anhui 245041, China*
[2]*Key Laboratory of Education Ministry for Modern Design and Rotor-Bearing System, School of Mechanical Engineering,*
 Xi'an Jiaotong University, Xi'an 710049, China
[3]*Department of Aero Oil and Material, Air Force Logistics College, Xuzhou, Jiangsu 221000, China*

Correspondence should be addressed to Ting Yao; ttyaoting@163.com

The deterioration of aero lubricating oil at high temperatures was accelerated by using a specific device simulating the operating conditions of engines, where the deterioration mechanism was obtained. Structures of the deteriorated lubricating oils were analyzed by gas chromatograph/mass spectrometer. From the results, it can be concluded that deterioration of aero lubricating oil at high temperatures was composed of thermal pyrolysis, oxidation, and polymerization, with the generation of a variety of products, such as alcohols, aldehydes, acids, and esters, which caused the deterioration of physicochemical properties of the aero lubricating oil.

1. Introduction

The change of molecular structure of aero lubricating oil is the fundamental cause that affects the functions of oil at high temperature [1–5]. The deterioration process, which includes thermal pyrolysis, oxidation, and polymerization, is complicated. The identification of products and investigation of reaction process can effectively explain the cause of deterioration mechanism of aero lubricating oil at high temperature, which can provide the theoretical basis for developing new and high-end lubricating oils.

The tested aero lubricating oil is a kind of synthetic lubricating oil with diisooctyl sebacate (DIOS) as its based oil, which has been extensively used in a certain type of aircraft engine lubrication system. The lubricating properties of aero lubricating oil will change due to deterioration caused by high temperature, high pressure, and high shearing, along with metallic catalysis (i.e., copper and iron) under the conditions of being exposed to the air. The deteriorated oil will do harm to the functions of the engine afterwards [6, 7]. In recent years, the deterioration of diester lubricating oil was focused on the performance deteriorated at high temperatures

[8–11]. Chen et al. explored the change about antioxidants during the decay of some aero lubricating oil. It was found that thermal oxidation of antioxidant was a pseudo-first-order reaction and the equation of reaction kinetics was obtained [8]. Fei et al. analyzed the pyroreaction products of diisooctyl adipate of aero lubricating oil using gas chromatograph/mass spectrometer (GC/MS) and indicated that the formation of substances (i.e., ketones, ethers, alcohols, and acids) was the primary cause of color deepening and increase of acid number [9]. Wu et al. simulated the oxidation of DIOS to investigate the lubricating properties of oil products under different degrees of oxidation by a four ball tester. The results showed that the formation of peroxide during the oxidation process of lubricating oil led to the deterioration of lubricating properties of oil products and occurrence of some polar products decreased abrasion loss [10]. Santos et al. analyzed the product of thermal deterioration by using FTIR and GC/MS, who found that the structure change was related with property change [11]. In these studies, the effect of factors and property changes of diester-like lubricating oil were focused on thermal oxidation. However, few studies concern the process and mechanism of thermal deterioration.

In the present investigation, some aero lubricating oil was subjected to simulating its oxidation under different high temperatures using the simulative device and subsequently analyzed by GC/MS. The deterioration mechanism was focused on investigation. This is of a great significance in improving the high-temperature performance of an aero lubricating oil, determining the appropriate oil change intervals and realizing the long-term quality monitoring on aero lubricating oil.

2. Experimental Section

2.1. Materials. Some aero lubricating oil was collected from some Fuel Research Institute. The reagents used in the experiment are analytical ones which are commercially available. All reagents (petroleum ether, n-hexane, acetone, and so on) used in the experiments were analytical reagents, and all the organic solvents had been distilled before use.

2.2. Simulation Testing on High-Temperature Oxidation. 128 g aero lubricating oil was added into a device (500 mL volume, 32 MPa, 450°C, 1100 r/min, and 2 kW, SongLing Co. Ltd, Yantai, China) simulating the operating conditions of the engine. The experimental lubricating oils were heated to the required temperatures (180, 200, 230, 250, 270, and 300°C) for 2 h, respectively, and the stirring rate was 800 r/min. For the convenience of description, the six experimental oils were marked with EO_{180}, EO_{200}, EO_{230}, EO_{250}, EO_{270}, and EO_{300}, respectively. After the reaction, the device was immediately placed in ice water until room temperature. The experimental oils were filtered and kept in dark conditions.

2.3. Acid Value Testing. The determination of acid values in testing samples is made in accordance with GB/T 264-1983(1991) Standard Testing Methods.

2.4. GC/MS Analyses. Oil samples were analyzed with a Hewlett-Packard 6890/5973 GC/MS, which was equipped with a capillary column coated with HP-5MS (cross-link 0.5% PH ME siloxane, 60 m length, 0.25 mm inner diameter, 0.25 μm film thickness) and a quadrupole analyzer with an m/z range from 33 to 500 and operated in electron impact (70 eV) mode. The capillary column was heated from 120 to 274°C at a rate of 13°C min^{-1} and held for 2 min, then raised to 281°C at a rate of 0.5°C and held for 2 min, finally raised to 300°C at a rate of 12°C and held at 300°C for 3 min. Data were acquired and processed using software of Agilent MSD Productivity Chemstation. Compounds were identified by comparing mass spectra with NIST05a library data.

3. Results and Discussion

3.1. Color and Molecular Compositions of Oils. As a direct appearance index, color change of oils can be determined by various factors, including both internal ones (base oil, additive, oil pigment, and so forth) and external conditions (temperature, high pressure, high shearing, metal catalysis, oxidation, run time, and so forth) [12]. In this study, color

of oils in different high-temperature reactions became more noticeable. EO_{180} is almost pale yellow and transparent at 180°C. As the reaction temperature rose, the color gradually deepens. It is worth noting that color becomes most remarkable at 230°C, even looking reddish brown. EO_{300} became not transparent but showed deep chocolate brown at 300°C. Most of aero lubricating oils were undergone significant color change under the high temperature, which provided a clue to explore the performance analysis for aero lubricating oils.

Figure 1 listed the total ion chromatogram of EO_{180}–EO_{300} before 20.4 min. As shown in Figure 1, in total, 50 compounds were detected with GC/MS, which included alkanes, alkenes, alcohols, acids, amines, ketones, monoesters, and diesters, and were displayed in Table 1. As demonstrated in Table 1, ester compounds dominated in detected compositions, which were 25 compounds. In addition, some chromogenic compounds are detected in EO_{180}–EO_{300}, including amines (peak 23, 25), phosphates (peak 30, 33, 42, 44–47), ketones (peak 12, 31, 36), and acids (peak 11, 43). Though few in content, they played a crucial role in significantly deepening color of aero lubricating oils. Meanwhile, these compounds, stronger in polarity, contributed to the enhancement of the acid number, increasing from 0.173 mg KOH/g in EO_{180} to 10.450 mg KOH/g in EO_{300}.

3.2. The Deterioration Mechanism of Oils. Temperature is one of the most important factors for the deterioration of aero lubricating oil. As displayed in Figure 1 and Table 1, the product amounts were markedly increased with raising temperature and reached maxima at 300°C and properties of aero lubricating oil change with the oil's compositions. The deterioration of oils is generally considered tending to form free radicals and follow the chain reactions under high temperature and oxygen conditions. But little work has been published to date about the deterioration mechanism of aero lubricating oil. We focus our attention on possible reaction mechanism at the molecular level in order to slower or prevent oil deterioration. As shown in Scheme 1, possible chemical reactions are thermal pyrolysis, thermal oxidation, and thermal polymerization according to detected compounds in Table 1.

3.2.1. Thermal Pyrolysis. DIOS, as based oil of experimental oil, is a long-chain diester with favorable symmetric structure with presented hydrogen of β-carbon at alcohol side. Hydrogen of β-carbon at alcohol side and oxygen of ester carbonyl groups formed intramolecular hydrogen bond by molecular movement, forming six-membered ring with C, O, and H atoms [13]. At high temperature, hexatomic ring was cracked into free radical I and II (Scheme 1(a)), and then free radical I and II recurred disproportionation reaction and generated 10-[(2-ethylhexyl)oxy]-10-oxodecanoate and 2-ethylhexene (peak 4, Scheme 1(b)). Along with the increase of reaction temperature, the relative abundances of 2-ethylhexene (peak 4) in EO_{180} to EO_{300} were 0.018, 0.012, 0.068, 0.293, 0.500, and 5.213%, respectively, indicating the pyrolysis extent of oil were significantly enhanced with raising temperature. 2-ethylhexene further produced ethylene and hexylene at the higher temperature (Scheme 1(c)). As
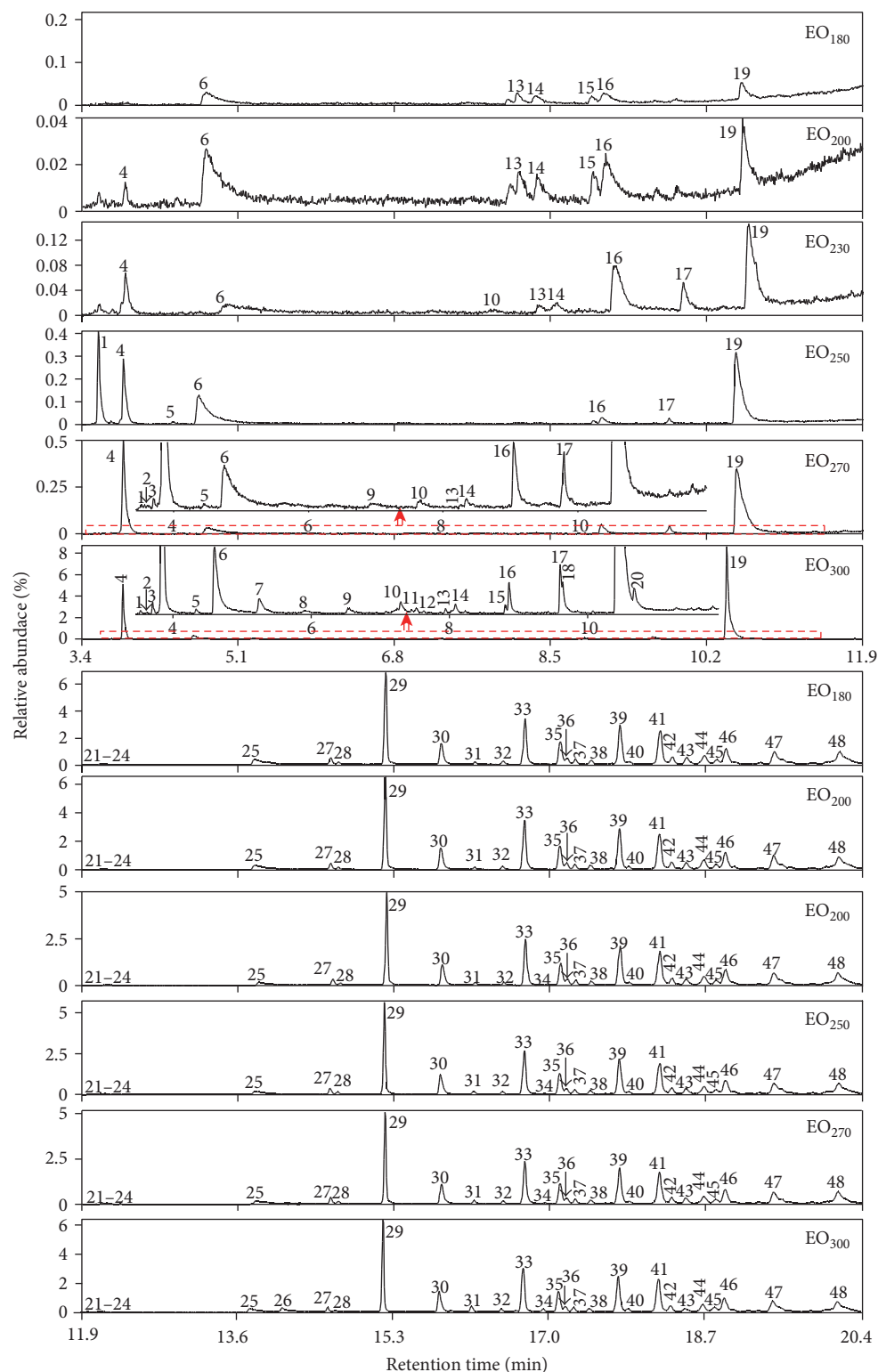
FIGURE 1: Total ion chromatograms of EO_{180}–EO_{300} before 20.4 min.

depicted in Scheme 1(d and e), parts of free radical II reacted with ethyl free radical and ethylene to generate 3-ethyloctane and 4-ethyloctene, respectively.

According to the structural formula, DIOS presented straight chain with eight carbons between ester groups. The straight chain could be cracked at high temperature, which is similar to straight-chain alkanes. The bonding energy of C-H bond of alkanes was higher than that of the C-C bond; therefore, homolysis of thermal pyrolysis started with C-C bond [14, 15], so did DIOS. All C-C bonds between ester groups can cause homolytic reaction at high-temperature conditions. The generated free radicals

TABLE 1: Distribution of compounds in EO_{180}–EO_{300}.

Peak	Compound	EO_{180}	EO_{200}	EO_{230}	EO_{250}	EO_{270}	EO_{300}
1	2-Pentene				×	×	×
2	4-Methyl-1-hexene					×	×
3	5-Methyl-3-heptene					×	×
4	3-Methylene		×	×	×	×	×
5	2-Ethylhexanal				×	×	×
6	2-Ethylhexane-1-alcohol	×	×	×	×	×	×
7	2-Ethylhexyl acetate						×
8	2-Ethylhexyl propionate						×
9	2-Ethylhexyl butyrate				×	×	×
10	2-Ethylhexyl valerate			×	×	×	×
11	12-Hydroxydodecanoic acid						×
12	4-Isopropylcyclohexane-1,3-diketone						×
13	2-Ethylhexyl-2-methoxyethyl acetate	×	×	×	×	×	×
14	2-Ethylhexylhexanoate	×	×	×	×	×	×
15	3-Ethylhexylhexanoate	×	×	×			×
16	Unknown	×	×	×		×	×
17	Unsaturated esters			×	×	×	×
18	2-Ethylhexyloctanoate						×
19	Unknown	×	×	×	×	×	×
20	2-Ethylhexyldecanoate						×
21	2-Ethylhexylacryloyloate	×	×	×	×	×	×
22	Unsaturated esters	×	×	×	×	×	×
23	(E)-N-(4-Butoxybenzylidene)-4-ethylaniline	×	×	×	×	×	×
24	Unknown	×	×	×	×	×	×
25	N-Phenylnaphthalene-2-amine	×	×	×	×	×	×
26	Unknown						×
27	(E)-1-(Pentyloxy)-3-cinnamenylbenzene	×	×	×	×	×	×
28	4-Methoxy-7-(2-methylbut-3-yn-2-oxy) furano[2,3-b]quinoline	×	×	×	×	×	×
29	Diisooctyl hexanedioate	×	×	×	×	×	×
30	Triphenyl phosphate	×	×	×	×	×	×
31	6-Heptyl-6-methyl-3-(pyridin-3-yl)-6,7-dihydro-1H-indazole-4(5H)-one	×	×	×	×	×	×
32	6-(Benzyloxymethyl)-3-butyl-2,4-dihydroxybenzene(methane)al	×	×	×	×	×	×
33	Diphenyl p-benzylphosphate	×	×	×	×	×	×
34	Isomer of 36			×	×	×	×
35	Bis(2-ethylhexyl)decanedioate	×	×	×	×	×	×
36	1-(3′-Benzoyl-2,6-dimethoxybiphenyl-3-yl)ethanone	×	×	×	×	×	×
37	Isomer of 36	×	×	×	×	×	×
38	Isomer of 36	×	×	×	×	×	×
39	Isomer of 36	×	×	×	×	×	×
40	Isomer of 36	×	×	×	×	×	×
41	Isomer of 36	×	×	×	×	×	×
42	Trio-benzylphosphate	×	×	×	×	×	×
43	3-(5-(3-Hydroxy-4-methylphenyl)-1-(3-hydroxyphenyl)-1H-pyrrol-2-yl)propanoic acid	×	×	×	×	×	×
44	Phenyldip-benzylphosphate	×	×	×	×	×	×
45	4-Ethylphenylphenyl p-benzylphosphate	×	×	×	×	×	×
46	Isomer of 42	×	×	×	×	×	×

TABLE 1: Continued.

Peak	Compound	EO$_{180}$	EO$_{200}$	EO$_{230}$	EO$_{250}$	EO$_{270}$	EO$_{300}$
47	Isomer of 42	×	×	×	×	×	×
48	Bis(2-ethylhexyl)decanedioate	×	×	×	×	×	×
49	Isomer of 48	×	×	×	×	×	×
50	1-(2-Ethyl-5-oxohexyl) 10-(2-ethylhexyl) decanedioate	×	×	×	×	×	×
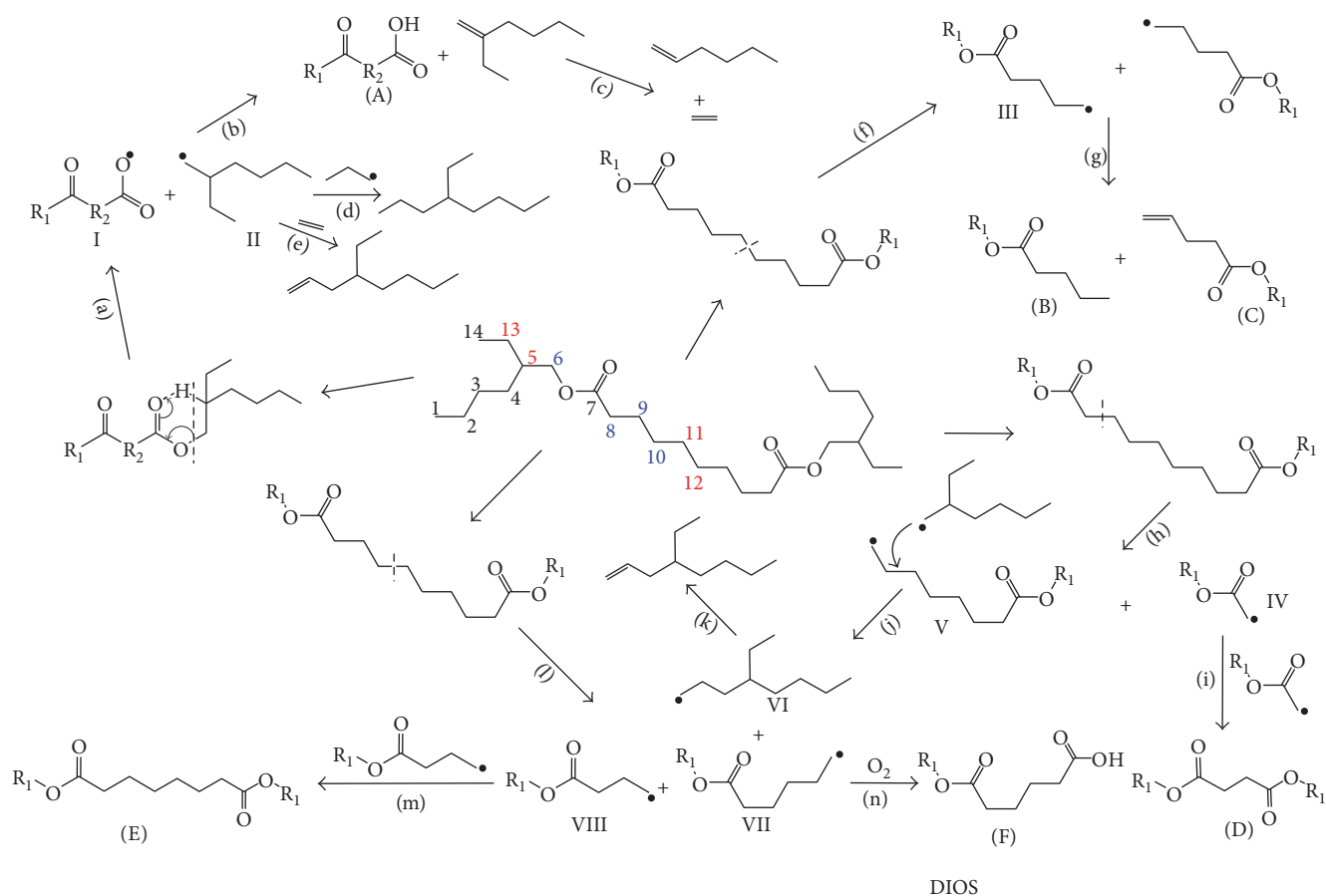
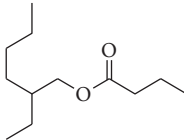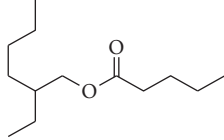SCHEME 1: Possible reaction process of thermal pyrolysis of DIOS.
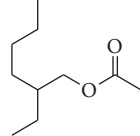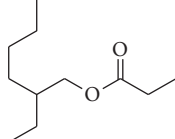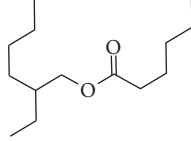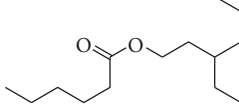
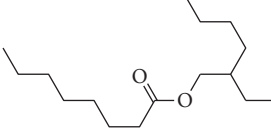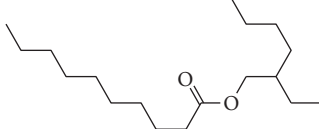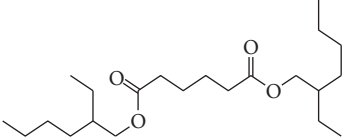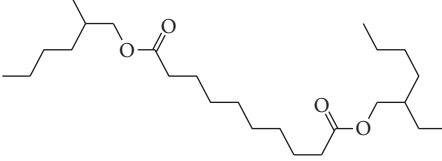caused disproportionation reaction to produce saturation and unsaturation monoester. The reaction processes and products of the cracked C-C bond at different positions will be consequently discussed with the basis of GC/MS analysis.

As exhibited in Scheme 1, when the breakpoint is at the C_{11}-C_{12} bond, DIOS could homolytically cracked two III free radicals (f). When two free radicals happened to have a collision, it will lead to the loss of H and generated unsaturated 2-ethylhexyle-4-olefine acid monoester (C), whereas the other free radical generated saturated 2-ethylhexyl-olefine acid monoester (B). When the breakpoint is at the C_8-C_9 bond, DIOS generated IV and V free radicals and then two IV free radicals can generate low molecular weight di-2-ethylhexyl diester by coupling reaction (D). In this system, II free radical attacked the β-carbon of V free radical to generate VII free radical and alkyl radical with

molecular weight of 141, whereas alkyl radical lost H atom and formed the alkene with molecular weight of 140 (Scheme 1(j and k)). When point of fracture is at the C_{10}-C_{11} bond, DIOS generated two VII and VIII free radicals, and two VIII free radicals bumped together and formed caprylyl glycol adipate (E) by coupling reaction (Scheme 1(m)). VIII free radical was oxidized by oxygen at some temperature and formed the 6-(2-ethylhexyloxy)-6-diakyl hexylic acid (Scheme 1(n)). When the breakpoint is at the C_9-C_{10} bond, DIOS could generate two free radicals and then formed diisooctyl adipate (F) by coupling reaction. Table 2 displayed the part ester compounds of EO$_{300}$.

Spatial position and the near groups varied with the type of the C-C bond, resulting in different interactions involved. Therefore, the hemolytic cleavage of the different C-C bonds

TABLE 2: Several ester compounds of EO_{300}.

Peak	Compound	Structural formula
7	2-Ethylhexylacetate	
8	2-Ethylhexylpropanoate	
9	2-Ethylhexylbutanoate	
10	2-Ethylhexylvalerate	
14	2-Ethylhexylhexanoate	
15	3-Ethylhexylhexanoate	
18	2-Ethylhexyloctanoate	
20	2-Ethylhexyldecanoate	
29	Diisooctyl hexanedioate	
35	Diisooctyl decanedioate	

at high temperatures leads to the different abilities of free radicals. Generally, bond length of chemical bond is inversely proportional to the bond energy: the more low bond energies, the more crack of chemical bond. Zhou et al. [16] calculated the bonding energies of C-C bond of *n*-decane and xylene by computational chemistry method. The results indicated that the low bonding energy of *n*-decane can more easily cause thermal pyrolysis.

The structure of DIOS was optimized by using semiempirical method (PM3 method) with an aid of Hyperchem 7.0 software (Figure 2). Table 3 exhibited the bond length of various C-C bonds between ester groups. The fitted results of HyperChem indicated that the bonding length of the C_7-C_8 bond was significantly lower than that of other C-C bonds, revealing that C_7-C_8 bond was not easy to break. The difference in bond length of other four C-C bonds suggested that the C-C bond could be broken at high temperature, which was consistent with the deterioration mechanism of DIOS as based oil. Thermal pyrolysis included the cracking of six-membered ring and long carbon chain between ester groups. The cracking of long carbon chain between ester groups at different positions formed the different free radicals [17]. The collision of free radicals caused coupling and disproportionation reaction, resulting in formation of unsaturation and saturation monoesters, diesters with molecular weight less than DIOS, and part diesters with molecular weight more than DIOS.

3.2.2. Thermal Oxidization.

Besides thermal pyrolysis, DIOS can cause thermal oxidization by the effect of oxygen under metal catalysis and high-temperature conditions. Alkene and reactive free radicals derived from thermal pyrolysis could be oxidized to form acid oxygen-containing compounds (peaks 11, 12, 31, 36, and 43), which lead to increasing acid number. Table 4 listed the acid number of experimental oils under different temperatures. As shown in Table 4, the acid number of EO_{180} is 0.173 mg KOH/g, which was lower than critical value (0.5 mg KOH/g) with less corrosion for engine. However, the acid number was 1.011 mg KOH/g at 250°C, which could mildly lead to the corrosion of the engine. Furthermore, when the heated temperature increases to 300°C, the acid number dramatically reached to 10.450 mg KOH/g, which meant that the engine was corroded severely and the aero lubricating oil must be replaced.

3.2.3. Thermal Polymerization.

The deterioration process not only is the cleavage of bonds but also includes polymerization, especially polycondensation at high temperature. It was reported that the oxidation products of lubricating oil could be condensed to polyoxides and then further formed the macromolecules [18, 19]. As expected from the GC/MS results, compounds of high molecular weight were detected in total ion chromatograms after 20.4 min. Due to the disadvantage of GC/MS, which only detects compounds with a molecular weight of less than 500, compounds of high molecular weight could not be detected and identified. Therefore, further research will
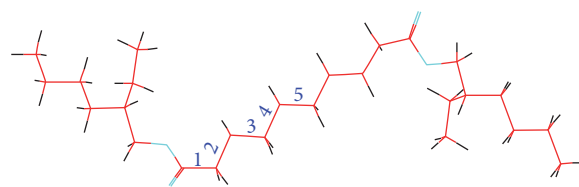

FIGURE 2: Optimized structure of DIOS.

TABLE 3: Simulated results of bond length by HyperChem.

Number	1	2	3	4	5
Bond length	1.5134	1.5209	1.5213	1.5202	1.5207

TABLE 4: Acid number (mg KOH/g) of EO_{180}–EO_{300}.

Sample	Acid number	Sample	Acid number
EO_{180}	0.173	EO_{250}	1.011
EO_{200}	0.221	EO_{270}	2.092
EO_{230}	0.728	EO_{300}	10.450

focus on identifying the macromolecules from oils. These macromolecules, which combined with degraded products of additives and wear metallic particles, formed oil sludge. Oil sludge could be dissolved into oils and/or deposited to the surface of engine or blocked the strainer and gallery, which decreased lubrication effect due to lack of oil supply.

4. Conclusions

In summary, it is demonstrated that some aero lubricating oil significantly cause deterioration with air under high temperature. According to analysis with GC/MS, three reactions were presented, which mainly included thermal pyrolysis, thermal oxidation, and thermal polymerization, and thermal pyrolysis dominated at high temperature. Thermal pyrolysis included the pyrolysis of six-ring esters and pyrolysis of long carbon chain of ester groups, resulting in formation of acid, alkene, and various reactive intermediates. And thermal reactions between alkene/reactive intermediates and oxygen generated chromogenic compounds, such as alcohol, aldehyde, and acid. In addition, coupling and disproportionation reactions were observed by collision of free radicals, which generated unsaturated monoester, saturated monoester, diesters, and high-molecular-height polymers. The thermal pyrolysis of DIOS generated acid substances, and derivative of part additives resulted in the increase of acid number of oil products. Moreover, these products influenced the aero lubricating oil properties. The products of thermal oxidation were ester- and hydrocarbon-like compounds. The former and the latter were the chromophoric and auxochromous substance, respectively, which lead to the dark

color of oil products after the oxidation process. The thermal polymerization generated the large molecular weight ester compounds. Then these ester compounds and degradation products generated oil sludge. The overabundance of oil sludge will block oil line and decreased the lubrication effect afterwards.

Conflicts of Interest

The authors declare that they have no conflicts of interest.

Acknowledgments

References

[1] D. C. Kramer, J. N. Ziemer, and M. T. Cheng, "Influence of group II & III base oil composition on VI and oxidation stability," *Nlgi Spokesman*, vol. 63, no. 10, pp. 20–39, 2000.

[2] H. Nakanishi, K. Onodera, K. Inoue, Y. Yamada, and M. Hirata, "Oxidation stability of synthetic lubricants," *Lubrication Engineers*, vol. 53, no. 5, pp. 29–37, 1997.

[3] L. N. Edmund, "Neopentyl polyol ester lubricants-bulk property optimization," *Industrial & Engineering Chemistry Product Research and Development*, vol. 15, no. 1, pp. 54–58, 1976.

[4] W. Liu, J. Xu, and D. Feng, "Research status and development tendency of synthetic lubricating oil," *Tribology*, vol. 33, no. 1, pp. 91–104, 2013, (In Chinese).

[5] X. Fan, J. Jiang, L. Chen et al., "Identification of organic fluorides and distribution of organic species in an anthracite with high content of fluorine," *Fuel Processing Technology*, vol. 142, pp. 54–58, 2016.

[6] K. C. Jayaprakash, S. P. Srivastava, K. S. Anand, and P. K. Goel, "Oxidation stability of steam turbine oils and laboratory methods of evaluation," *Lubrication Engineers*, vol. 40, no. 2, pp. 89–95, 1984.

[7] A. C. M. Wilson, "Problems encountered with turbine lubricants and associated systems," *Lubrication Engineers*, vol. 32, no. 2, pp. 59–65, 1976.

[8] L. B. Chen, S. H. Guo, S. Y. Li, L. Q. Song, and Z. G. Zhang, "Thermal oxidization kinetics of antioxidant in aero lubricating oil," *Journal of Fuel Chemistry and Technology*, vol. 30, no. 6, pp. 523–528, 2002, (In Chinese).

[9] Y. W. Fei, X. L. Peng, T. Yao, F. Guo, and Y. H. Wang, "Component analysis of ester-like aero lubricating oil at high temperature," *Petrochemical Technology*, vol. 43, no. 12, pp. 1444–1449, 2014, (In Chinese).

[10] Y. Wu, W. Li, and X. Wang, "The influence of oxidation on the tribological performance of diester lubricant," *Lubrication Science*, vol. 26, no. 1, pp. 55–65, 2013.

[11] J. C. O. Santos, I. M. G. Santos, and A. Souza, "Thermal degradation process of synthetic lubricating oils: part I, spectroscopic study," *Petroleum Science and Technology*, vol. 33, no. 11, pp. 1238–1245, 2015.

[12] Y. W. Fei, Z. S. Cheng, H. W. Yang, and T. Yao, "Characteristic analysis of ester-like synthetic aero lubricating carrier oil," *Contemporary Chemical Industry*, vol. 42, no. 9, pp. 1297–1300, 2014, (In Chinese).

[13] N. Ponnekanti and K. Savita, "Study of synthetic complex esters as automotive gear lubricants," *Journal of Synthetic Lubrication*, vol. 25, no. 25, pp. 131–136, 2008.

[14] F. C. Li, J. S. Zhang, and Q. M. Yuan, "Reaction mechanism of thermal and catalytic pyrolysis of octane and formation of methane," *Journal of Fuel Chemistry and Technology*, vol. 42, no. 6, pp. 697–703, 2014, (In Chinese).

[15] B. Y. Wang, N. X. Tan, Q. Yao, and Z. R. Li, "Accurate calculation of the reaction barriers and rate constants of the pyrolysis of alkyl radicals in the β-position using the isodesmic reaction method," *Acta Physico-Chimica Sinica*, vol. 28, no. 12, pp. 2824–2830, 2012, (In Chinese).

[16] H. Zhou, J. Mao, B. Y. Wang, Q. Zhu, J. L. Wang, and X. Y. Li, "Thermal pyrolysis of decane and xylene under supercritical pressure conditions," *Acta Physico-Chimica Sinica*, vol. 29, no. 4, pp. 689–694, 2013, (In Chinese).

[17] M. Wang, X. Fan, X. Y. Wei et al., "Characterization of the oxidation products of Shengli lignite using mass spectrometers with 'hard', 'soft' and ambient ion sources," *Fuel*, vol. 183, pp. 115–122, 2016.

[18] J. F. Lahijani, F. E. Lockwood, and E. E. Klaus, "The influence of metals on sludge formation," *A S L E Transactions*, vol. 25, no. 1, pp. 25–32, 1982.

[19] J. A. Supp and R. E. Kornbrekke, "Deposit formation in gasoline engines: part 1. Base oil in sequence VE deposits," *Lubrication Engineers*, vol. 50, no. 12, pp. 964–969, 1994.

Research Article

Thermometric Titration for Rapid Determination of Trace Water in Jet Fuel

Jian-Qiang Hu,[1] Jian-Jian Zhang,[1] Shi-Zhao Yang,[1] Yong-Liang Xin,[1] Li Guo,[1] and Ting Yao[1,2]

[1]*Department of Aviation Oil and Material, Air Force Logistics College, Xuzhou 221000, China*
[2]*Analysis and Testing Center, Huangshan University, Huangshan 245041, China*

Correspondence should be addressed to Jian-Qiang Hu; hjq555918@sohu.com and Ting Yao; ttyaoting@163.com

Water content in jet fuels is detected by thermometric titration (TMT), and the optimal detected system is 2,2-dimethoxypropane as titrant, cyclohexane and isopropanol as titration solvents, and methanesulfonic acid as catalyst in this method. The amounts of oil, concentration and delivery rate of titrant, volumes, and the reliability and accuracy of thermometric titration were emphasized. The results show that the accuracy, validity, and reliability of TMT are excellent by different indicated spiked water contents. The obtained results between TMT and Karl Fischer titration have been proven to be in accord. But, the duration of titration merely spends 3–5 min in the whole process, greatly shortening the detected time. Therefore, rapid and accurate determination of trace water in a jet fuel can be realized by TMT.

1. Introduction

Water in jet fuels can result in fuel system icing, microbial contamination, and corrosion, which was considered as an important quality of fuel performance. Under a low-temperature environment, dissolved water content of jet fuels is reduced and free water in fuels generates small ice crystals that block the oil line and decrease the normal fuel supply, so as to threaten flight safety [1]. Thus, water content in jet fuels must be strictly controlled.

At present, several field and laboratory methods are used to determine water in oil products. Field method is mainly visual observation method (VOM), which is conducted for the qualitative determination of water. However, as is characteristic of poor accuracy and repeatability, VOM cannot perform accurate quantitative determination of water in oil products [2]. Laboratory methods mainly include sensor method, solvent reflux, and Karl Fischer titration. Sensor method can achieve online measurement, but which requires established standard curves for each oil product.

Meanwhile, the results are bound to be affected by the environment [3]. Solvent reflux method can directly give free water contents in oil products; however, the method in obtaining data is subjective, complicated, time-consuming, and low accuracy [4]. Although the Karl Fischer method can obtain accurate water contents, because of highly toxic reagents, complicated preparation, and short service life, it has seriously hindered the practical uses [5]. Therefore, thermometric titration (TMT) is presented and attracted more and more attention due to rapidity, convenience, automation, and particularly excellent accuracy and applicability. TMT has been successfully applied in product quality, process control, and analysis of acidic substances and ions in aqueous and nonaqueous phase systems of different areas, such as petroleum, chemical engineering, electric power, pharmacy, and hygiene [6–11].

In the present investigation, the water of jet fuel was subjected to determination by TMT. As the same time, results by TMT are compared with by Karl Fischer, and accuracy and repeatability of results by TMT are further testified.

2. Experiments

2.1. Experimental Principle. TMT is an analytical method used to determine the content of substances, which is measured on the basis of different values of enthalpy of reaction [12]. Water content through TMT is based on the endothermic reaction between 2,2-dimethoxypropane (DMP) and water. Water content in jet fuels can be calculated when the inflection point in temperature-titration volume curves is used as titer of the titrant.

Water content in jet fuel is detected with DMP as titrant. DMP has undergone an endothermic reaction with water under the catalytic action of acids, and its enthalpy is +27.6 kJ/mol. The reaction equation of DMP and H2O is exhibited as (1).

$$CH_3C(CH_3OH_2)_2CH_3 + H_2O \xrightarrow{H+} 2CH_3OH + (CH_3)_2CO. \tag{1}$$
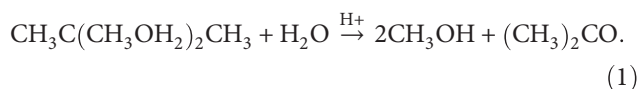
2.2. Reagent and Instrument. DMP (98%), isopropyl alcohol (A.R.), cyclohexane (A.R.), and methanesulfonic acid (MSA; 99%) were purchased from the Shanghai China National Medicines Corporation Ltd. Number 3 jet fuel was purchased from the Tianjin branch of Sinopec. The obtained reactants were dehydrated through a molecular sieve and placed in a dryer.

A self-developed automatic TMT device was equipped with titration software, high-precision temperature-sensing probe, volumetric dispenser, and magnetic stirrer. The titration software has the unique capability of processing large number of data points at the rate of 8 measurements every second which is critical for reliable detection of the endpoint; the probe can measure the temperature to 0.01°C and have a response time of less than 0.3 s; volumetric dispenser can consistently deliver desired volume of titration solvent. Electronic scales from German Sartorius Corporation are capable of weighing to ±0.1 mg. 10 μL and 1000 μL microinjectors were purchased from Shanghai Anting Microsyringe Plant. The SC-3 Karl Fischer titrator was produced by Shandong Zhonghui Instrument Co. Ltd.

2.3. Reagent Preparation

(1) Preparation of the titrant: 12.5 mL DMP was accurately weighed, added into 100 mL volumetric flask, and dissolved into a constant volume with cyclohexane; the DMP titrant with a concentration of approximately 1.0 mol/L was obtained. Then, 0.1 mol/L, 0.5 mol/L, 1.5 mol/L, and 2.0 mol/L DMP titrants were prepared according to the above method.

(2) Preparation of the titration solvent: the titration solvent was obtained by mixing isopropyl alcohol and cyclohexane with a volume ratio of 2 : 3.

(3) Preparation of the standard aqueous solution: 1 μL, 2 μL, 4 μL, 8 μL, 16 μL, and 20 μL distilled water were dissolved into 10 g anhydrous isopropyl alcohol, and standard solutions with mass fractions of 0.01% (w/w), 0.02% (w/w), 0.04% (w/w), 0.08% (w/w),

TABLE 1: Results of different mass.

Mass (g)	2.0	5.0	10.0	15.0	20.0	30.0
Recovery rate (%)	97.2	99.3	100.8	102.1	104.8	105.5

0.16% (w/w), and 0.2% (w/w) were obtained, which was used to calibrate the concentration of DMP titrant.

2.4. Experimental Method

(1) TMT: the appropriate amount of jet fuel was accurately weighed and added to the thermal insulation reaction flask; then, 20 mL titration solvent and 200 μL MSA were added to the flask and fully dissolved with the stirring speed of 200 r/min; the thermistor and titrant delivery line were placed into the sample. DMP titrant with appropriate concentration was delivered to the sample at a constant speed. The TMT software was used to record the temperature and titrant volume of the titration system; there was a change in the slope of the plot of temperature versus volume, which indicated the endpoint of the titration. Endpoints were determined by calculating the second derivative and facilitating the determination of the endpoint. During titration, there is a blank to be determined. The blank titration is a summation of all delays inherent in the titration solution under defined experimental conditions. These delays were caused from kinetics of the chemical reaction between titrant and titrand, sensor response, mixing inefficiencies, electronic transfer, and computation of data. The volumes of the titrant obtained in the blank titration were subtracted from those in the initial titration data of fuel samples. Each titration experiment was performed three times.

(2) Karl Fischer titration: the water content in jet fuel was measured by Karl Fischer method of ASTM D6304.

3. Results and Discussion

3.1. Effect of the Mass of Fuel, Concentration, and Delivery Rate of Titrant on Thermometric Titration. The water contents in jet fuel are relatively small, so the mass of fuel, concentration, and delivery rate of titrants will affect the accuracy of the determination results in thermometric titrations. As Table 1 shows, the mass was 2.0 g and there is a slight deviation. The mass was between 5.0 g and 15.0 g and the test value was basically consistent with the real value. The mass reached or exceeded 20.0 g and there was a large deviation. These observations show that the effects of sample mass on the determination results are relatively small in a reasonable range.

The results of titrant consumption under different concentrations of titrants are listed in Table 2, from which we can see clearly the concentrations of the titrant have great influence on determination result of TMT. The smaller the concentration of the titrant is, the larger the consumption

TABLE 2: Results of different concentrations of titrant.

Concentration (mol·L^{-1})	0.1	0.5	1.0	1.5	2.0
Recovery rate (%)	108.2	101.1	99.5	98.3	92.2

TABLE 3: Results of different delivery rates of titrant.

Delivery rate (mL·min^{-1})	0.5	0.8	1.0	1.5	2.0	3.0
Recovery rate (%)	105.8	101.5	99.3	96.5	92.8	89.5

TABLE 4: Corresponding relationship between spiked water content and DMP titer.

Spiked water content (%)	0.01	0.02	0.03	0.04	0.05
DMP titer (mL)	0.947	1.013	1.073	1.127	1.173

FIGURE 1: Calibration curve of the DMP.

of the titrant volume is, which results in larger deviation. The higher the concentration of the titrant is, the smaller the consumption of the titrant volume is, which results in larger error on determination results. In summary, the most optimal titrant concentration is between 0.5 mol/L and 1.5 mol/L. In addition, in order to compare Karl Fisher conveniently, the concentration of titrant was used as 1.0 mol/L in all experiments.

As showed in Table 3, when the delivery rate of the titrant was 0.5 mL·min^{-1}, the recovery rate was 105.8%. When the delivery rate was between 0.8 mL·min^{-1} and 1.0 mL·min^{-1}, the test value and real value of titrant consumption were quite close. When the delivery rate reached or exceeded 1.5 mL·min^{-1}, deviation is large. Therefore, the delivery rate of titrant played an important role on the determination results for TMT, and the most optimal titration rate is between 0.8 mL·min^{-1} and 1.0 mL·min^{-1}.

3.2. Determination of the Standard Water Content. The prepared DMP titrant was calibrated by five groups of standard solutions. Linear fitting of the data points was conducted, and titrant concentration was calculated according to the slope. The determination results were displayed in Table 4.

Linear fitting of the standard water content and DMP titer was conducted. As demonstrated in Figure 1, the calibration curve of DMP was $y = 5.6650x + 0.8967$. According to the calculation based on the linear fitting equation, the slope of the fitted straight line was $k = 5.6650$. The straight slope k was the value in millimeters of consumed titrant per 1% water content in 10 g jet fuel. According to the chemical equation of DMP and H_2O, the ratio between DMP and H_2O with regard to the stoichiometric number of the chemical reaction was 1 : 1. 0.9807 mol/L DMP was be obtained according to the experimental results.

Jet fuel with mass of 10.015 g was accurately weighed. Then, spiked water with different mass fractions was added to the jet fuel and mixed with 20 mL titrant and 200 μL MSA. Stirring velocity was set at 200 r/min, and 1.0 mol/L titrant was used at a titration velocity of 0.8 mL/min. As
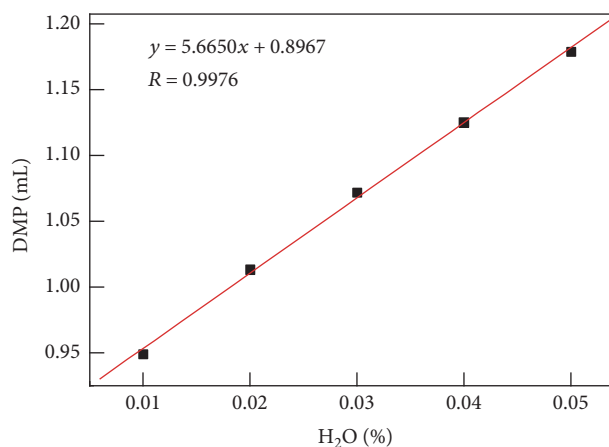
TABLE 5: Results of jet fuels with different standard water contents.

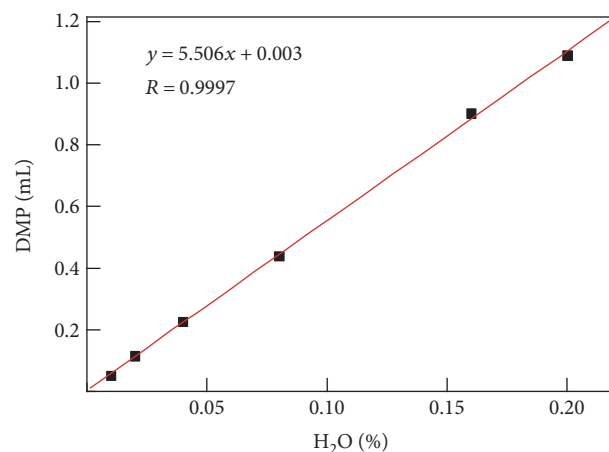| Spiked water content (%)	0.01	0.02	0.04	0.08	0.16	0.20
Spiked recovery rate (%)	102.4	101.5	98.6	99.0	101.5	98.2
Relative standard deviation (%)	2.8	3.1	3.5	1.8	1.6	1.5

FIGURE 2: Linear regression equation of determining the spiked water contents.

shown in Table 5, the spiked recovery rates under high- and low-water contents were high, that is, they are within 98% to 103%.

Linear fitting of the standard water content and DMP titer was established. Figure 2 demonstrated the linear regression equation between the spiked water contents and DMP titers. The linear regression coefficient R was 0.9997. When the spiked water contents within 0.01% (*m/m*) and 0.2% (*m/m*) were tested in the jet fuels, the determination results were highly accurate with favorable repeatability.

3.3. Determination of the Water Content in Jet Fuels. Under room temperature (20°C) and humidity (80%) conditions,
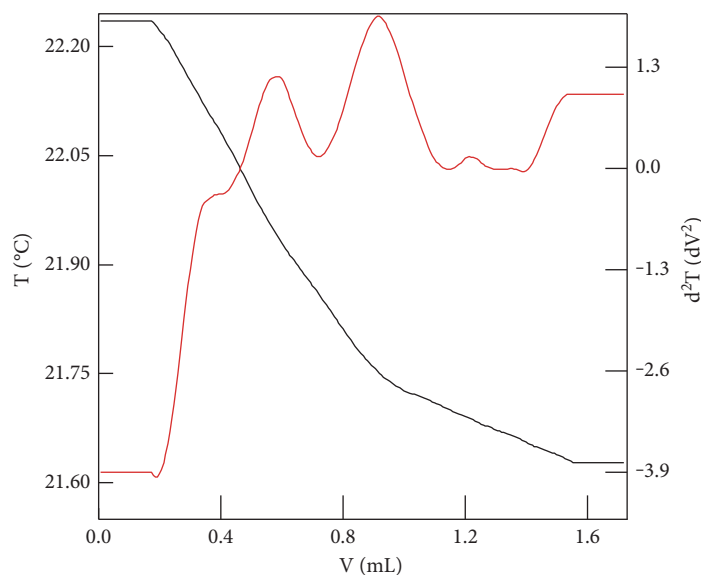
FIGURE 3: The curves of temperature titration.

jet fuels with mass of 10 g were accurately weighed. Calibrated DMP was used to determine the water contents in jet fuels. The curve of temperature titration was shown in Figure 3.

The selection of the endpoint of titration was automatically carried out with no interference with the manual. A second derivative was rapidly formulated to confirm the automatic selection of endpoint by titration software. TMT and Karl Fischer method were used to determine the water content in jet fuels under different conditions. As displayed in Table 6, at different temperatures, the water determination results obtained through TMT were accurate. Thus, this method was appropriate for determining water content in jet fuels.

TABLE 6: Results of the water content (μg·g^{-1}) in jet fuels under different conditions.

Factors		TMT				Karl
Temperature (°C)	Humidity (%)	A	B	C	Mean value	Fischer
0	60	30	36	39	35	31
6	65	35	46	45	42	38
9	71	52	45	53	50	51
16	77	47	62	62	57	55
20	80	57	54	63	58	60
24	83	59	68	68	65	63
31	85	70	75	83	76	69

3.4. *Mechanism Analysis of TMT Determining Water.* On the basis of the influence of the laws of the titration conditions, the reaction principle between DMP and H$_2$O was analyzed during the determination process. The DMP titrant contained H$_3$C–OH groups, which would react with water by absorbing heat and realizing water determination. The reaction mechanism between DMP and H$_2$O was shown in Figure 4.

The structure of DMP titrant contains two methoxy groups connected to one carbon atom forming large sterically hindered and strong chemical activity. This structure easily undergoes nucleophilic substitution with water. Under catalyst-free conditions, S$_N$2 nucleophilic substitution occurs in the reaction. Particularly, H$_2$O induces backside attack of the leaving groups as nucleophilic reagents. Fracturing of old bonds and formation of new bonds simultaneously proceed. However, the stronger the nucleophilicity of the reagent in the S$_N$2 reaction is, the higher the reaction velocity is. The nucleophilicity of H$_2$O is smaller than that of methoxyl. Therefore, the reaction slowly occurs between DMP and H$_2$O without catalyst, so slowly so that the reaction
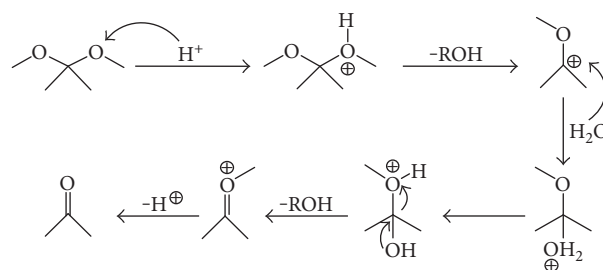
FIGURE 4: Proposed mechanism between DMP and H$_2$O.

cannot be noticed. Herein, we focus on acid as catalyst to accelerate the reaction and convert the reaction process from S$_N$2 substitution into S$_N$1 substitution. Protonation effect occurs in DMP because of the bond between the proton and methoxyl. As a result, methyl alcohol molecules were separated from DMP and formed carbocations. After a methoxyl was lost, steric hindrance was reduced, so it would be easily attacked by the nucleophilic reagent. As the nucleophilic reagent, H$_2$O was bonded with carbocations, then the

second methyl alcohol molecule was separated from a center carbon atom, and formation of protonated acetone occurred. As heat was absorbed in this process, the protons were finally removed to form acetone, and the removed protons continued the catalytic reaction.

4. Conclusion

The determination results on 0.01%–0.2% (m/m) spiked water were highly accurate and good repeatable. The obtained results on trace water in jet fuel at different temperature and humidity conditions were in accordance with those obtained using the Karl Fischer method. The duration of the entire determination process was 3–5 min. The trace water in jet fuels could be accurately and rapidly determined by TMT. As a result, TMT was appropriate for the determination of trace water in jet fuels.

Conflicts of Interest

The authors declare that they have no conflicts of interest.

Acknowledgments

References

[1] K. Chen, H. Xiang, T. Sun, and D. M. Dian, "Research on the icing behavior of water in the jet fuel," *Petrochemical Industry Applicant*, vol. 33, no. 12, pp. 1–5, 2014.

[2] N. Wu, J. Q. Hu, and S. Z. Yang, "Study on change rule of dissolved water content in jet fuels," *Petroleum Processing and Petrochemicals*, vol. 41, no. 9, pp. 22–24, 2015.

[3] X. G. Chen, X. X. Tian, and Y. Yang, "Research of on-line monitoring of trace moisture content in transformer oil," *Journal of Southwest University (Natural Science Edition)*, vol. 31, no. 1, pp. 1–4, 2009.

[4] C. Zhang, X. Chen, D. J. Webb, and G.-D. Peng, "Water detection in jet fuel using a polymer optical fibre Bragg grating," *20th International Conference on Optical Fibre Sensors*, vol. 75, no. 03, pp. 81–84, 2009.

[5] G. H. Nicolta, I. H. Daniel, and I. Heinz-dieter, "Water content of natural cyclodextrins and their essential oil complexes: a comparative study between Karl Fischer titration and thermal methods," *Food Chemistry*, vol. 132, no. 4, pp. 1741–1748, 2012.

[6] F. M. Najib, S. Zewar, and A. M. Abdulla, "A new sensor for thermometric titrations," *Talanta*, vol. 71, no. 1, pp. 141–148, 2007.

[7] P. E. G. Jean and M. R. José, "Isothermal titration calorimetry: a thermodynamic interpretation of measurements," *Chemical Thermodynamics*, vol. 55, pp. 193–202, 2012.

[8] G. Burgot, F. Auffret, and J. L. Burgot, "Determination of acetaminophen by thermometric titrimetry," *Analytica Chimica Acta*, vol. 343, no. 1-2, pp. 125–728, 1997.

[9] S. U. Huan, W. A. Hart, and G. O. Yan, "Determination of sulfate ion FGD equipment from fossil fuel power plants by thermometric titration," *Thermal Power Generation*, vol. 44, no. 4, pp. 116–119, 2015.

[10] T. K. Smith, "Analysis of FFA in edible oils by catalyzed end-point thermometric titrimetry (CETT)," *Journal of the American Oil Chemists' Society*, vol. 80, no. 1, pp. 21–24, 2003.

[11] S. Z. Yang, J. Q. Hu, and L. Guo, "Rapid determination for acidity of aviation oils by thermometric titration," *Acta Petrolerei Sinica (Petroleum Processing Section)*, vol. 30, no. 1, pp. 71–75, 2014.

[12] E. J. Greenhow, "Catalytic thermometric Titrimetry," *Chemical Reviews*, vol. 77, no. 6, pp. 835–854, 1977.

Research Article

Electronic Controlling on Nanotribological Properties of a Textured Surface by Laser Processing

Haifeng Yang,[1,2] Kun Liu,[1] Yanqing Wang,[3] Hao Liu,[1] Jiaxiang Man,[1] and Bo Sun[1]

[1]*College of Mechanical & Electrical Engineering, China University of Mining and Technology, Xuzhou, Jiangsu 221116, China*
[2]*Jiangsu Key Laboratory of Mine Mechanical and Electrical Equipment, China University of Mining and Technology, Xuzhou 221116, China*
[3]*School of Materials Science and Engineering, China University of Mining and Technology, Xuzhou 221116, China*

Correspondence should be addressed to Kun Liu; liuk1995@163.com

The friction-reducing performance of surfaces with regular nanotextures is a key topic in surface engineering research. This paper presented a simple, easily controlled method for fabricating regular nanotextures on an electrodeposited Ni-Co alloy. The electronic controlling on the friction performance of a nanotexured surface was investigated by AFM. The results showed that the frictional force of a nanotexured surface can be controlled by an external electric field. Before laser processing, the friction initially increased with the bias voltage and then decreased after the bias voltage exceeded 1.0 V. Its friction forces can be changed more than 2 times under the different external electric field. After laser processing, the trend of the frictional force was reversed and its friction forces changed more than 12 times for the laser-processed sample with 0.18 J/cm^2 laser power. The results also showed that the friction force decreased when using different nanotextures in an external electric field.

1. Introduction

In computing and MEMS areas, Ni-Co coating was widely applied in such devices as microforceps, micromirrors, and microswitches. Usually, these devices worked under an external electric field. However, the effect of this external electric field on the friction performance of Ni-Co coatings was rarely studied. Meanwhile, it can also be used in the controlling of the friction coefficient or maintaining its stability.

Through controlling the surface characteristics, an engineered surface can be made to deliver the desired functional performance [1]. Except for a wide range of other applications of laser technique [2–4], as an effective technique, it also was used to improving the coating performances [5–8]. Many researchers have investigated the laser processing technique about how to improve surface performance of alloy coatings [9–11]. Nowadays, methods such as moulding [12], electrochemical deposition [13, 14], and chemical vapor deposition [15] are used to produce artificial surfaces with particular textures. However, all of these methods fail to produce controllable textured surfaces. In recent years, many researchers have adopted new processes to fabricate textures on solid surfaces. Mo et al. fabricated the nanotexture on an H-passivated Si surface by current-induced local anodic oxidation and investigated its nanotribological properties by colloidal probe [16, 17]. The results indicated that the nanotextures exhibited low adhesion and greatly reduced the friction at a nanometric scale. Fang Liang investigated the friction and wear of a 45# steel surface textured by YAG laser and found that the coefficient of friction of a cross-grooved surface increased with decreasing texture span (i.e., width of pattern). The tribological properties of nanotextures on Ni-Co coatings have not been extensively studied to date.

In recent years, many researchers have investigated the relationship between the nanotribological properties and external electric field at nanoscale in different domains. Park et al. found that the nanoscale friction properties of a Si (100) sample can be manipulated significantly by the simple application of a bias voltage [18]. They then observed a significant increase in friction under accumulation (forward bias)
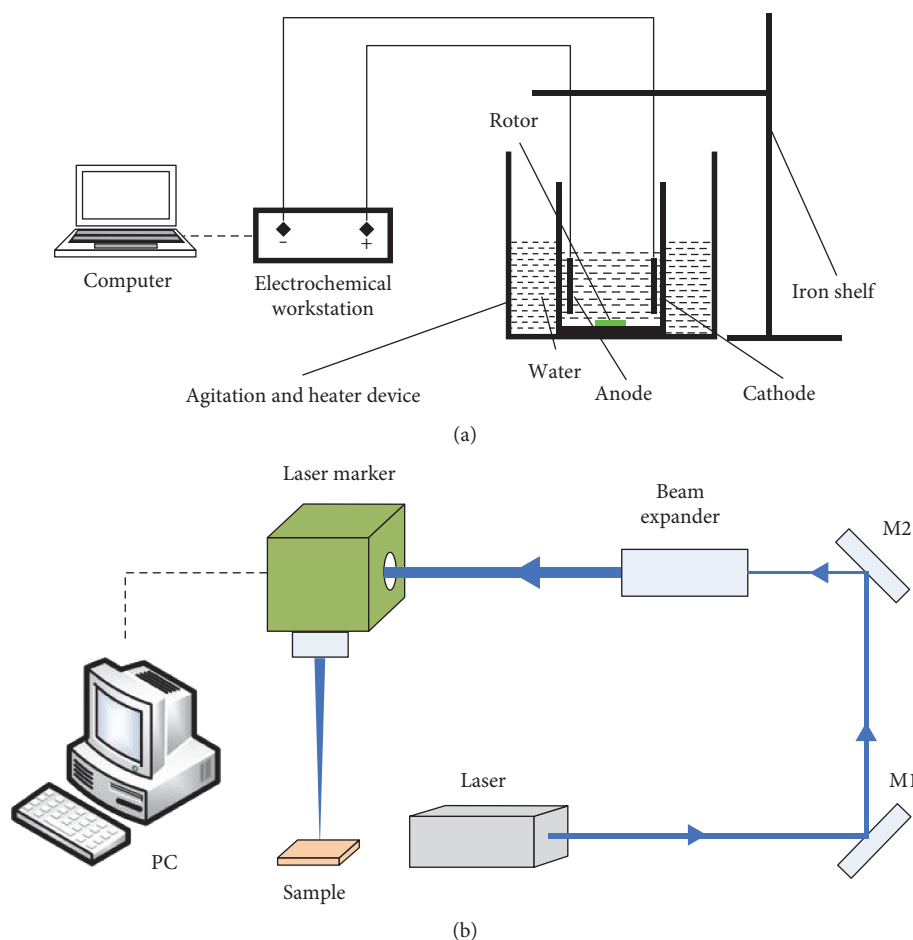
(a)

(b)

Figure 1: (a) Schematic of the electroplating setup. (b) Laser processing experimental system.

conditions with respect to depletion (reverse bias) conditions and established a model based on the force exerted by the trapped charges that quantified the experimental observations of excess friction, using a Pt-coated tip with a 50 nm radius in an AFM sliding against an n-type GaAs (100) substrate [19]. Liu et al. investigated the microtribological properties of Langmuir-Blodgett monolayer films in AC and DC electric fields [20]. They found that the friction and wear characteristics of Langmuir-Blodgett films could be controlled and improved by an external electric field. However, the influence of an external electric field on the friction properties of nanotextures on a Ni-Co coating has not previously been studied.

Here, the nanotextures on the Ni-Co alloy coating surface were fabricated by the laser processing technique. The surface morphology and microstructure of the laser-processed region were characterized by SEM. Then, the nanotribological behavior of different nanotexured surfaces under external electrical field was investigated by FFM and AFM.

2. Experiments

2.1. Experimental Setup. The experimental setup for the electroplating is shown in Figure 1(a). A type of CHI660D electrochemical workstation was used to provide power supply.

Table 1: The composition of the electroplating bath solution and relevant processing parameters.

Composition	Content/gL^{-1}
Cobalt sulphate	30
Nickel sulphate	250
Nickel chloride	40
Boric acid	35
Code position condition	
Temperature (°C)	50
pH	3.5 to 4.5

Figure 1(b) showed the laser processing experimental system for fabricating nanotextures on the electroplated Ni-Co alloy coating surface. An ultraviolet laser (DSH-355-10, Photonics Industries, USA) with a working wavelength of 355 nm was used to process the specimen. The laser beam was completely reflected by two mirrors. The reflected beam was filled, collimated, and expanded by a beam expander. The beam expander could allow the high-frequency noise to be removed from the laser beam to provide a clean Gaussian profile and make the laser beam smaller after focusing. A computer-controlled laser marker was used to control the direction of the laser beam.
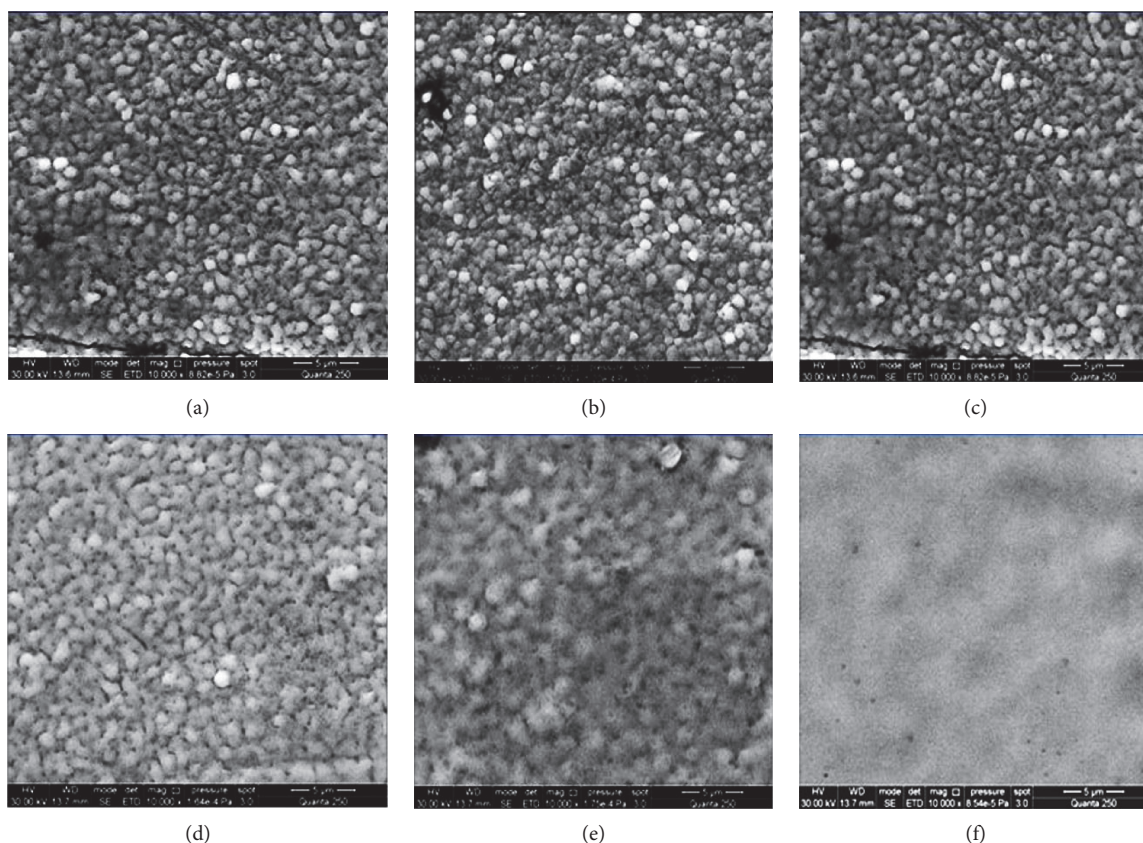
(a)   (b)   (c)

(d)   (e)   (f)

FIGURE 2: SEM images of Ni-Co alloy coating surface. (a) Unprocessed; laser processed at (b) 0.03 J/cm^2; (c) 0.05 J/cm^2; (d) 0.08 J/cm^2; (e) 0.18 J/cm^2; (f) 0.22 J/cm^2.

2.2. Experimental Method. Before the electroplating of Ni-Co alloy coating, the bath composition was prepared according to Table 1. To ensure that the composition of the bath was uniform, the electrolyte was subject to magnetic stirring for 20 min before the deposition process started. A nickel sample, of commercial-purity grade, measuring 80 mm × 60 mm × 2 mm was used as the anode, and a type 316L stainless steel specimen, measuring 20 mm × 10 mm × 2 mm, was used as the cathode. The cathode was placed 30 mm from, and parallel to, the nickel when immersed in the bath. Before electroplating, the specimen was polished using 2000 grit and then degreased in acetone under ultrasonic vibration for 5 min and then pretreated in 1 mol/L HCL solution for 2 min at room temperature to remove the surface oxide scale.

Then, the electroplating was performed under direct current conditions with the current density of 25 mA/cm^2 and electroplating time of 20 min. After electroplating, distilled water was used to wash the specimen. The specimen was tested after being dried at room temperature in air for several hours. The deposition thickness was about 8 μm. The surface morphology and microstructure of the coating were characterized by SEM.

After that, the laser processing experimental system was used to fabricate nanotextures on the electroplated Ni-Co alloy coating. The laser power ranged from 0 J/cm^2 to 2 J/cm^2 at a scan speed of 25.4 mm/s and line interval of 0.01 mm. The SEM was used to analyze the effect of laser irradiation on the surface morphology and microstructure of the coating.

Lastly, the nanotribological behavior of the Ni-Co alloy coating in this electric field was measured by AFM/FFM (CSPM5500 electronics, Benyuan Nano-Instruments, China). The probe was coated with a conducting layer of Au film. The varying load (0.1 to 1.0 V) and bias voltage (0.0 V, 0.5 V, 1.0 V, 1.5 V, and 2.0 V) were applied between the probe and the sample.

3. Results and Discussions

3.1. Laser-Induced Nanotextures on the Ni-Co Alloy Coating. The laser power was varied to investigate the influence on the Ni-Co alloy coating. The laser power was increased from 0 J/cm^2 to 0.22 J/cm^2. Figure 2 shows the micrographs of the Ni-Co alloy surfaces after laser processing at 0 J/cm^2, 0.03 J/cm^2, 0.05 J/cm^2, 0.08 J/cm^2, 0.18 J/cm^2, and 0.22 J/cm^2.

The morphology of the Ni-Co alloy coating before laser process was shown in Figure 2(a). Many irregular-sized microparticles and nanoprotrusions were observed. The average diameter of the grains was approximately 0.7 μm. The Co content in the coating accounted for 40% of its total mass. The roughness R_a of the Ni-Co coating surface was approximately 25 nm. After laser processing at 0.03 J/cm^2, most of the irregular protrusions become half-
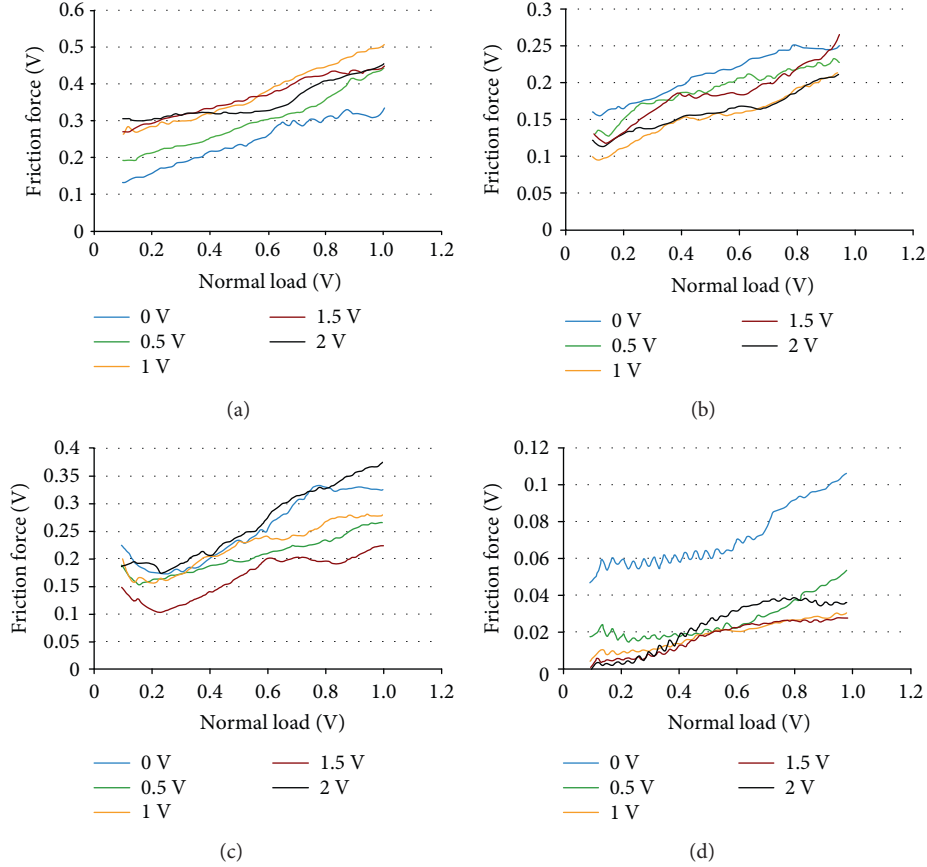
(a)

(b)

(c)

(d)

FIGURE 3: Frictional force versus normal load, from 0.1 V to 1.0 V, with five bias voltages (0 V, 0.5 V, 1 V, 1.5 V, and 2 V) for the four Ni-Co alloy coating surfaces. (a) unprocessed; laser processed at (b) 0.03 J/cm^2; (c) 0.05 J/cm^2; (d) 0.18 J/cm^2.

hemispherical and more regular and the surface morphology of the laser-processed area was also uneven (Figure 2(b)). With increase of laser power, the half-hemispherical nanoprotrusions grew uniformly and gradually became half-ellipsoid structures. Besides, when the laser powers were 0.05 and 0.08 J/cm^2, the surface morphology of the laser-processed area becomes flatter, as shown in Figures 2(c) and 2(d). At 0.18 J/cm^2, the half-hemispherical nanoprotrusions continued to grow and began to reduce in number (Figure 2(e)). Figure 2(f) showed that the surface morphology of the laser-processed area had become relatively smooth at 0.22 J/cm^2 and the nanoprotrusions had completely disappeared.

Through these experiments, we concluded that the formation of regular nanoprotrusions was dependent on the power of the ultraviolet laser. Therefore, we can adjust the power of the ultraviolet laser for fabricating stable nanoprotrusions on the surface of the Ni-Co alloy coating. Koch et al. and Mannion et al. once proposed a theory in which nanoprotrusions were formed because of the interference between the incident laser and the excited surface electromagnetic waves caused by the presence of structural defects [21, 22]. This theory can be also used to explain the formation of nanoprotrusions on the surface of the Ni-Co alloy coating. Moreover, after laser irradiation, vaporization and redeposition of the nanoparticles should also affect the

surface nanostructures. However, the detailed mechanism underpinning this behavior requires further investigation [23]. When the applied laser power was greater than 0.22 J/cm^2, the Ni-Co alloy coating underwent rapid fusion due to extreme heat. Therefore, the surface morphology of the laser-processed area became smooth, and the nanoprotrusions on the surface almost all vanished.

3.2. Nanotribological Properties under Different Bias Voltages. Figure 3 showed the different relationships between the frictional force and normal load at bias voltages of 0 V, 0.5 V, 1.0 V, 1.5 V, and 2.0 V. It can be seen that the friction increased quasilinearly with increasing normal load for the different Ni-Co alloy coating surfaces.

In Figure 3(a), for unprocessed specimen, the friction force with a forward bias voltage was larger than that without a bias voltage. Its friction forces can be changed more than 2 times under the different external electric field. However, the situation was reversed in Figures 3(b), 3(c), and 3(d). This difference in the frictional forces was mainly due to changes in the surface crystal lattice and texture that can influence the friction between metal friction pairs [24]. It may be concluded that the bias voltage can be increased to reduce friction on the surface after laser processing. In particular, the friction force under a bias voltage was significantly reduced (Figure 3(d)). Its friction forces changed more
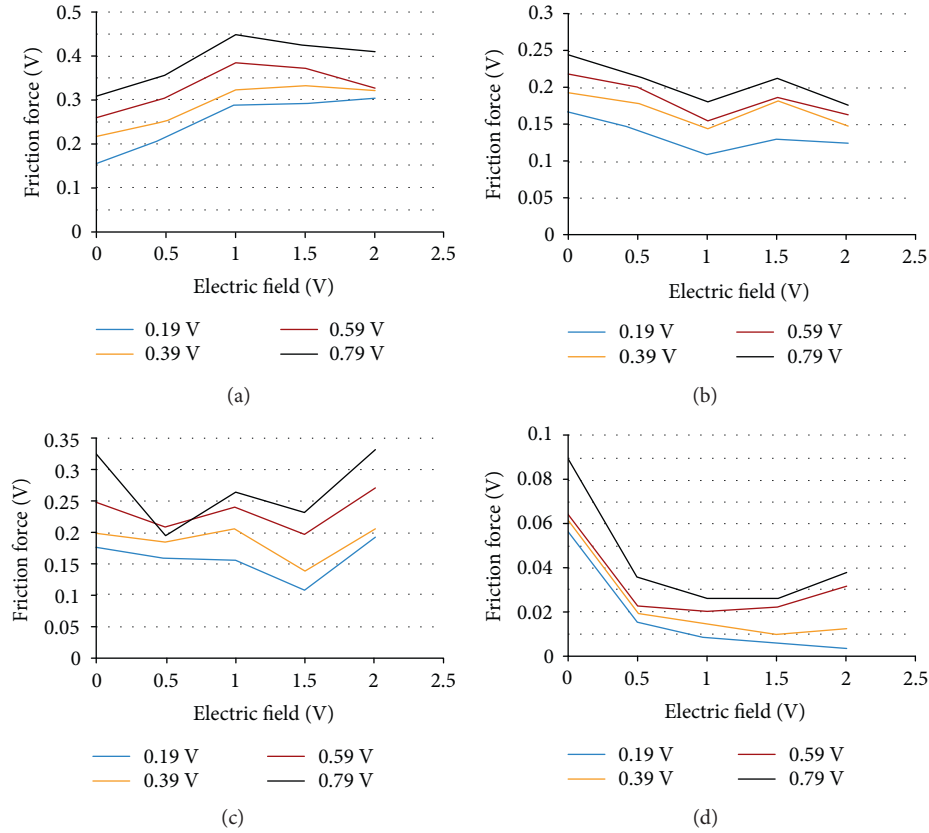
(a)

(b)

(c)

(d)

FIGURE 4: Frictional force versus bias voltage, from 0 V to 2 V, at four normal loads (0.19 V, 0.39 V, 0.59 V, and 0.79 V) for the four Ni-Co alloy coating surfaces. (a) Unprocessed; laser processed at (b) 0.03 J/cm^2; (c) 0.05 J/cm^2; (d) 0.18 J/cm^2.

than 12 times for this specimen. Therefore, the nanotribological properties were affected by laser irradiation under a forward bias voltage.

Figure 4 showed the relationship between frictional force and the bias voltages of 0.0 V, 0.5 V, 1.0 V, 1.5 V, and 2.0 V with four normal loads (0.19 V, 0.39 V, 0.59 V, and 0.79 V). The frictional force could be controlled by external electric field. In Figure 4(a), the frictional force initially increased with increasing bias voltage but then decreased while the bias voltage exceeded 1.0 V at normal loads of 0.19 V, 0.39 V, 0.59 V, and 0.79 V. However, the frictional force initially decreased with increasing bias voltage and then increased as shown in Figures 4(b), 4(c), and 4(d). The trend varied, mainly due to the changes in the surface crystal lattice and texture [25].

There are two main theories which may be used to interpret these behaviors: electrostatic interaction theory and self-generated voltage theory. Electrostatic interaction theory dictated that the external electric field can influence the electrostatic force between friction pairs and thus affects the real normal load (P_{real}). The sphere-plane electrostatic adhesion force (F_e) is related to the voltage of the external electronic field (U). When the bias voltage exceeds 0 V, the real normal load initially decreases with increasing bias voltage and then it increased, which matched the measured results. Self-generated voltage theory said that during the repeated relative movement of the tip and sample surface, the friction between metal friction pairs would self-generate a voltage V_g [24–26], the direction of which might be

contrary to the external electric voltage V_e. Thereinto, the self-generated voltage V_g increases as the number of repeating relative movements between the tip and sample surface increases [25]. Thus, the actual bias voltage V_a between tip and sample surface is $V_a = V_e - V_g$. After laser treatment, the changes in the surface crystal lattice and texture affected the rate of increase of V_g. This trend is reversed after laser irradiation, because of the differing rates of increase of V_g and V_e.

3.3. Nanotribological Properties of Different Nanotextures. Figure 5 showed the variation in friction force and normal load for different sample surfaces (unprocessed and processed at 0.03 J/cm^2, 0.05 J/cm^2, and 0.18 J/cm^2). Figure 5(a) showed a plot of the frictional force versus normal load at the same bias voltage V_e of 0 V. According to the comparison of the sample before and after laser processing, the differences between the trends were not clear. A plot of the frictional force versus normal load at the same bias voltages V_e of 0.5 V, 1.0 V, and 2.0 V were shown separately in Figures 5(b), 5(c), and 5(d). When the bias voltage exceeded 0 V, the differences between the changing trends of the surface friction force become distinct: after laser processing, the surface friction was significantly lower than before. Thus, the frictional force can be controlled through the use of laser processing under a forward bias voltage. In Figure 5, as the surface became smooth after laser processing
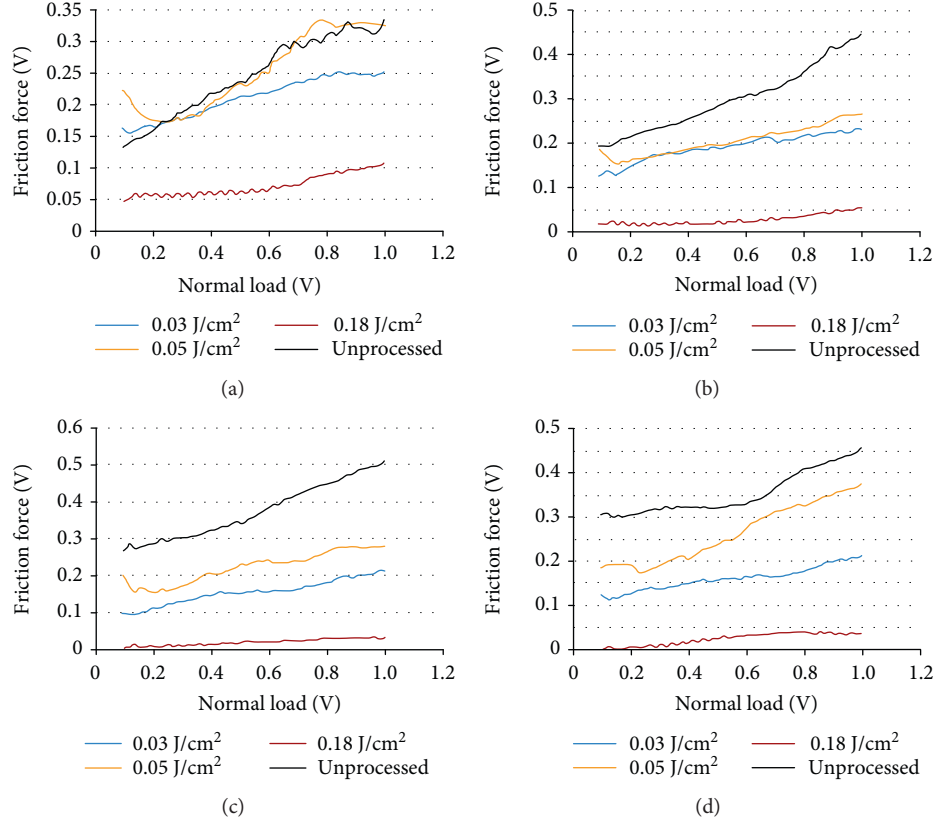
FIGURE 5: Frictional force versus normal load for the different sample surfaces under four constant bias voltages. (a) 0 V; (b) 0.5 V; (c) 1.0 V; (d) 2.0 V.

at 0.18 J/cm^2, the frictional force changed between approximately between 0.05 V and 0.1 V under a bias voltage of 0 V and varied between 0 V and 0.05 V when the bias voltage exceeded 0 V. To some extent, the frictional force remained stable. Therefore, under an external electrical field and specific laser processing, the Ni-Co alloy surface frictional force can be controlled so as to be reduced by the nanotexture deposited on the Ni-Co alloy coating.

4. Conclusions

This paper presented a simple, easily controlled laser processing method for fabricating regular nanotextures on the electrodeposited Ni-Co alloy surface. The electronic controlling on the friction performance of the nanotexured surface was achieved using atomic force microscope. Regular nanoprotrusions can be produced by choosing certain laser processing parameters, and the frictional force on such nanotexured surfaces can be controlled by an external electric field. Before laser processing, the friction initially increased with the bias voltage and then decreased after the bias voltage exceeded 1.0 V. Its friction forces can be changed more than 2 times under the different external electric field. After laser processing, the trend of the frictional force was reversed and its friction forces changed more than 12 times for the laser-processed sample with 0.18 J/cm^2 laser power. Furthermore, with certain nanotextures and bias voltages, the frictional force could be maintained at a stable value.

Nomenclature

P_{real}: Real normal load [N]
F_e: Electrostatic adhesion force [N]
U: External electronic field [V]
V_g: Self-generate a voltage [V]
V_a: Actual bias voltage [V]
V_e: External electric voltage [V].

Subscripts

MEMS: Micro-Electro-Mechanical System
AFM: Atomic force microscope
SEM: Scanning Electronic Microscopy
FFM: Friction force microscopy
M: Mirror.

Conflicts of Interest

The authors declare that they have no conflicts of interest.

Acknowledgments

References

[1] A. A. G. Bruzzone, H. L. Costa, P. M. Lonardo, and D. A. Lucca, "Advances in engineered surfaces for functional performance," *Cirp Annals-Manufacturing Technology*, vol. 57, no. 2, pp. 750–769, 2008.

[2] X. Fan, M. W. Little, and K. K. Murray, "Infrared laser wavelength dependence of particles ablated from glycerol," *Applied Surface Science*, vol. 255, no. 5, pp. 1699–1704, 2008.

[3] J. X. Man, H. F. Yang, Y. Q. Wang, C. Yan, and S. Zhang, "Nanotribological properties of nanotextured Ni-Co coating surface measured with AFM colloidal probe technique," *Journal of Laser Micro/Nanoengineering*, vol. 12, no. 1, pp. 16–21, 2017.

[4] X. Fan, S. Z. Wang, A. L. Zheng et al., "Investigation on infrared laser desorption of solid matrix using scanning electron microscope and fast photography," *Microscopy Research and Technique*, vol. 76, no. 7, pp. 744–750, 2013.

[5] I. Etsion, O. Levinson, and G. Halperin, "Experimental investigation of the elastic-plastic contact area and static friction of a sphere on flat," *Journal of Tribology*, vol. 127, no. 1, pp. 47–50, 2005.

[6] K. D. Zhang, J. X. Deng, R. Meng, P. Gao, and H. Yue, "Effect of nano-scale textures on cutting performance of WC/Co-based Ti55Al45N coated tools in dry cutting," *International Journal of Refractory Metals and Hard Materials*, vol. 51, pp. 35–49, 2015.

[7] H. S. Amoli, H. Amani, and M. Mozaffari, "Deposition of ITO nanopowder layers on flexible substrate by spin coating using pulsed Nd-YAG laser for crystallization and bonding," *Journal of Russian Laser Research*, vol. 34, no. 6, pp. 581–585, 2013.

[8] R. Ghasemi, R. Shoja-Razavi, R. Mozafarinia, and H. Jamali, "The influence of laser treatment on thermal shock resistance of plasma-sprayed nanostructured yttria stabilized zirconia thermal barrier coatings," *Ceramics International*, vol. 40, no. 1, pp. 347–355, 2014.

[9] H. F. Yang, H. D. He, E. L. Zhao et al., "Electronic-controlling nanotribological behavior of textured silicon surfaces fabricated by laser interference lithography," *Laser Physics Letters*, vol. 11, no. 10, article 105901, 2014.

[10] H. F. Yang, H. D. He, E. L. Zhao et al., "Simulation and fabrication of nanostructures with laser interference lithography," *Laser Physics*, vol. 24, no. 6, pp. 225–292, 2014.

[11] H. F. Yang, T. C. Chen, J. G. Qian et al., "Friction-reducing micro/nanoprotrusions on electrodeposited Ni–Co alloy coating surface fabricated by laser direct writing," *Bulletin of Materials Science*, vol. 38, no. 1, pp. 173–181, 2015.

[12] J. Bico, C. Marzolin, and D. Quéré, "Pearl drops," *Europhysics Letters*, vol. 47, no. 2, pp. 220–226, 1999.

[13] X. Zhang, F. Shi, X. Yu et al., "Polyelectrolyte multilayer as matrix for electrochemical deposition of gold clusters: toward super-hydrophobic surface," *Journal of the American Chemical Society*, vol. 126, no. 10, pp. 3064-3065, 2004.

[14] N. J. Shirtcliffe, G. McHale, M. I. Newton, G. Chabrol, and C. C. Perry, "Dual-scale roughness produces unusually water-repellent surfaces," *Advanced Materials*, vol. 16, no. 21, pp. 1929–1932, 2004.

[15] Y. Y. Wu, H. Sugimura, Y. Inoue, and O. Takai, "Thin films with nanotextures for transparent and ultra water-repellent coatings produced from trimethylmethoxysilane by microwave plasma CVD," *Chemical Vapor Deposition*, vol. 8, no. 2, pp. 47–50, 2002.

[16] Y. F. Mo, W. J. Zhao, D. M. Huang, F. Zhao, and M. Bai, "Nanotribological properties of precision-controlled regular nanotexture on H-passivated Si surface by current-induced local anodic oxidation," *Ultramicroscopy*, vol. 109, no. 3, pp. 247–252, 2009.

[17] Y. F. Mo, Y. Wing, J. B. Pu, and M. Bai, "Precise positioning of lubricant on a surface using the local anodic oxide method," *Langmuir*, vol. 25, no. 1, pp. 40–42, 2009.

[18] J. Y. Park, Y. Qi, D. Ogletree, P. A. Thiel, and M. Salmeron, "Influence of carrier density on the friction properties of silicon pn junctions," *Physical Review B*, vol. 76, no. 6, article 064108, 2007.

[19] Y. Qi, J. Park, B. Hendriksen, D. F. Ogletree, and M. Salmeron, "Electronic contribution to friction on GaAs: an atomic force microscope study," *Physical Review B*, vol. 77, no. 18, article 184105, 2008.

[20] H. Liu, S. Fujisawa, A. Tanaka, and Y. Enomoto, "Controlling and improving the microtribological properties of Langmuir–Blodgett monolayer films using an external electric field," *Thin Solid Films*, vol. 368, no. 1, pp. 152–156, 2000.

[21] J. Koch, F. Korte, T. Bauer, C. Fallnich, A. Ostendorf, and B. N. Chichkov, "Nanotexturing of gold films by femtosecond laser-induced melt dynamics," *Applied Physics A*, vol. 81, no. 2, pp. 325–328, 2005.

[22] P. T. Mannion, J. Magee, E. Coyne, G. M. O'connor, and T. J. Glynn, "The effect of damage accumulation behaviour on ablation thresholds and damage morphology in ultrafast laser micro-machining of common metals in air," *Applied Surface Science*, vol. 233, no. 1–4, pp. 275–287, 2004.

[23] W. Jia, Z. N. Peng, Z. J. Wang, X. Ni, and C. Y. Wang, "The effect of femtosecond laser micromachining on the surface characteristics and subsurface microstructure of amorphous FeCuNbSiB alloy," *Applied Surface Science*, vol. 253, no. 3, pp. 1299–1303, 2006.

[24] R. Chen, W. Zhai, and Y. Qi, "The mechanism and technology of friction control by applying electric voltage II. The effects of applied voltage on friction," *TRIBOLOGY-BEIJING*, vol. 16, no. 3, pp. 235–238, 1996.

[25] W. Zhai, R. Chen, and Y. Qi, "The mechanism and technique of friction control by applied voltage I. The correlation of self-generated voltage to friction force," *TRIBOLOGY-BEIJING*, vol. 16, no. 1, pp. 1–5, 1996.

[26] H. R. Ao, Y. F. Gao, W. J. Zhai, and Y. L. Qi, "An experimental research on self-generated potential of ball-disc friction pair under normal pressure and low and middle vacuum," *TRIBOLOGY-BEIJING*, vol. 19, no. 250, pp. 250–254, 1999.